

UNIVERSITY OF OKLAHOMA  
GRADUATE COLLEGE

CHARACTERIZATION OF THE CONVECTIVE BOUNDARY LAYER  
THROUGH A COMBINATION OF LARGE-EDDY SIMULATIONS AND A  
RADAR SIMULATOR

A DISSERTATION  
SUBMITTED TO THE GRADUATE FACULTY  
in partial fulfillment of the requirements for the  
Degree of  
DOCTOR OF PHILOSOPHY

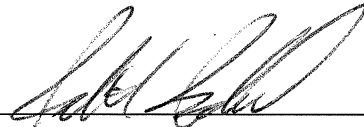
By

DANNY SCIPIÓN  
Norman, Oklahoma  
2011


CHARACTERIZATION OF THE CONVECTIVE BOUNDARY LAYER  
THROUGH A COMBINATION OF LARGE-EDDY SIMULATIONS AND A  
RADAR SIMULATOR

A DISSERTATION APPROVED FOR THE  
SCHOOL OF ELECTRICAL AND COMPUTER ENGINEERING

BY



Dr. Robert Palmer



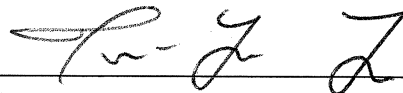
Dr. Phillip Chilson



Dr. Evgeni Fedorovich



Dr. Richard Doviak



Dr. Tian-You Yu

©Copyright by DANNY SCIPIÓN 2011  
All Rights Reserved.

## Acknowledgments

This work was primarily supported by the National Science Foundation (NSF) for their support via grant ATM-0553345. The observational data for this study were obtained from the Atmospheric Radiation Measurement (ARM) Program sponsored by the U.S. Department of Energy, Office of Science, Office of Biological and Environmental Research, Environmental Science Division. Special thanks to committee co-chairs Dr. Robert Palmer and Dr. Phillip Chilson for their guidance, comments, and suggestions during the course of this project. Additional thanks to Dr. Evgeni Fedorovich for his time and advice, especially in giving a meteorological perspective to the project. I would also like to acknowledge my committee members, Dr. Tian-You Yu and Dr. Richard Doviak for their efforts put forth in reviewing my work and for offering their comments, suggestions, and corrections.

In addition, I would like to thank my parents, Eddy Scipi3n and Juany Castillo de Scipi3n for being my motivation, and showing me the value of pursuing higher education in order to succeed in a competitive world. Finally, to Dustin Baum for his support, encouragement, understanding, patience, and especially his time throughout this project.

# Contents

<b>Acknowledgments</b>	<b>iv</b>
<b>List Of Tables</b>	<b>viii</b>
<b>List Of Figures</b>	<b>ix</b>
<b>Abstract</b>	<b>xv</b>
<b>1 Introduction</b>	<b>1</b>
1.1 The Atmospheric Boundary Layer: A Brief Review . . . . .	1
1.2 Radars for Sensing the Atmosphere . . . . .	6
1.2.1 Weather Radars: Particle Scattering From Precipitation . . .	7
1.2.2 Profiling Radars: Clear-Air Scattering from Refractive Index Variations . . . . .	13
1.3 Large-Eddy Simulations to Characterize the Atmospheric Boundary Layer . . . . .	17
1.4 Motivation for Dissertation . . . . .	18
1.5 Outline of Dissertation . . . . .	19
<b>2 Large-Eddy Simulations and Doppler Radars: Theoretical Back- ground</b>	<b>20</b>
2.1 Large-Eddy Simulations . . . . .	20
2.2 Pulsed Doppler Radar . . . . .	27
2.2.1 Basic Concepts . . . . .	27
2.2.2 The Radar Equation . . . . .	33
2.2.3 Scattering Mechanisms . . . . .	33
2.2.3.1 Weather Radar - Rayleigh Scatter . . . . .	33
2.2.3.2 Clear-Air Radar - Bragg Scatter . . . . .	35
2.3 Signal Processing for Radars that Observe the Atmosphere . . . . .	37
2.3.1 Spectral Moments . . . . .	39
2.3.1.1 Moment Estimation in the Time Domain . . . . .	40
2.3.1.2 Moment Estimation in the Frequency Domain . . . . .	42
2.4 Techniques for the Estimation of the Three-Dimensional Wind Field .	43
2.4.1 Doppler Beam Swinging . . . . .	43
2.4.2 Spaced Antenna . . . . .	45

<b>3</b>	<b>Radar Simulator Design Based on Large-Eddy Simulations</b>	<b>49</b>
3.1	Time Series Radar Simulator . . . . .	49
3.2	Possible Configurations of the Virtual Radar . . . . .	56
3.2.1	Monostatic Configuration . . . . .	58
3.2.1.1	Doppler Beam Swinging . . . . .	59
3.2.1.2	Multiple Radar Configuration . . . . .	61
3.2.2	Spaced Antenna . . . . .	62
<b>4</b>	<b>Characterization of the Boundary Layer: Validation with Realistic Data</b>	<b>64</b>
4.1	Experimental Configuration . . . . .	64
4.2	Structure Function Parameter of Refractive Index . . . . .	65
4.3	Wind Field Comparisons . . . . .	68
4.4	Vertical Velocity Variance . . . . .	73
4.5	Vertical Velocity Skewness . . . . .	75
<b>5</b>	<b>Comparison between LES and Virtual Boundary Layer Radar</b>	<b>78</b>
5.1	Effect of Horizontal Shear of Vertical Velocity on Horizontal Wind Estimates . . . . .	78
5.1.1	Theoretical Formulation . . . . .	78
5.1.1.1	Doppler Beam Swinging . . . . .	78
5.1.1.2	Spaced Antenna . . . . .	79
5.1.2	Test Configurations . . . . .	80
5.1.2.1	DBS Configuration . . . . .	81
5.1.2.2	Spaced Antenna Configuration . . . . .	83
5.1.3	Results . . . . .	85
5.2	Turbulence Kinetic Energy Based on Radar Wind Estimates . . . . .	97
5.2.1	Theoretical Formulation . . . . .	97
5.2.2	Results . . . . .	98
5.3	Turbulence-Eddy Dissipation Rate Based on Radar Spectrum Width . . . . .	99
5.3.1	Theoretical Formulation . . . . .	99
5.3.2	Results . . . . .	103
<b>6</b>	<b>Conclusions and Future Work</b>	<b>110</b>
6.1	Conclusions . . . . .	110
6.2	Future Work . . . . .	114
	<b>Reference List</b>	<b>116</b>
	<b>Appendix A - List Of Symbols</b>	<b>127</b>
	<b>Appendix B - List Of Acronyms and Abbreviations</b>	<b>135</b>
	<b>Appendix C</b>	
	Calculations of Structure Function Parameter of Refractive Index . . . . .	138



## List Of Tables

1.1	Fractional concentration by volume of the major constituents of the Earth's atmosphere up to 105 km, with respect to dry air (from Wallace and Hobbs (2006)). . . . .	2
1.2	Example of typical VCPs utilized by the WSR-88D based on the type of weather occurring (from <a href="http://www.wdtb.noaa.gov/tools/RPS/">http://www.wdtb.noaa.gov/tools/RPS/</a> ). . . . .	10
1.3	Classification of radars according to their altitude coverage . . . . .	15
2.1	Description of the LES settings . . . . .	24
2.2	Examples of the values of $Z$ . . . . .	35
2.3	Examples of the magnitude and intensity of $C_n^2$ . . . . .	36
3.1	Description of the LES settings . . . . .	51
5.1	Description of the field domain used by the radar simulators . . . . .	81
5.2	Specifications of DBS configuration . . . . .	82
5.3	Specifications of SA configuration . . . . .	84

# List Of Figures

1.1	The structure of the Earth’s atmosphere (modified from Ahrens (1991)). The structure reflects how temperature, density, and composition of the atmosphere change with height, and how it is determined in large part by how it interacts with the sun’s light. . . . .	3
1.2	Depiction of the diurnal development of the atmospheric boundary layer (adapted from Stull (1988)). . . . .	6
1.3	Location of radars present at the OPERA radar database updated in June 2010 (from <a href="http://www.knmi.nl/opera/">http://www.knmi.nl/opera/</a> ). The color dots represent the frequency bands: C-band = green, S-band = blue, X-band = cyan. The center color represent the type of radar: dual polarization radar = red center, Doppler radar= yellow center. . . . .	8
1.4	Location of the operational WSR-88D radars (National Oceanic and Atmospheric Administration (NOAA) 2007 (from <a href="http://radar.weather.gov/">http://radar.weather.gov/</a> ). The color coding represent the US agency in charge of the correct operation of the radar. . . . .	9
1.5	(a) NEXRAD Radar at the WSR-88D Radar Operations Center in Norman, OK (from <a href="http://en.wikipedia.org/wiki/NEXRAD">http://en.wikipedia.org/wiki/NEXRAD</a> ). (b) Phased-Array Radar (PAR) in Norman, OK (from <a href="http://www.thunderchaser.com/june2005/spc_tour.html">http://www.thunderchaser.com/june2005/spc_tour.html</a> ). . . . .	11
1.6	(a) Jicamarca Incoherent Scatter Radar at Lima, Peru (from <a href="http://jro.igp.gob.pe">http://jro.igp.gob.pe</a> ). (b) The SOUSY (SOUnding SYstem) Radar at Lindau, Germany (from <a href="http://radars.uit.no/sousy/index.html">http://radars.uit.no/sousy/index.html</a> ). (c) NARL MST Radar at Gadanki, India (from <a href="http://www.narl.gov.in/">http://www.narl.gov.in/</a> ). (d) MU (Middle and Upper atmosphere) Radar at Shigaraki, Japan (from <a href="http://www-lab26.kuee.kyoto-u.ac.jp/study/mu/mu_e.html">http://www-lab26.kuee.kyoto-u.ac.jp/study/mu/mu_e.html</a> ). . . . .	14
1.7	Schematic of the evolution of the inertial subrange with height. The horizontal axis represent the Bragg scale. In the troposphere, the Bragg scale extends safety from $10^{-1}$ to 10 m, which corresponds to frequencies of 1.5 GHz (UHF) - 15 MHz (VHF), respectively (from Hocking (1985)). . . . .	15
2.1	Schematic representation of idealized (a) and realistic (b) initial data (from Botnick and Fedorovich (2008)). . . . .	23
2.2	Examples of LES fields in the virtual radar sub-domain. Top-left: zonal wind. Top-right: meridional wind. Middle-left: potential temperature. Middle-right: specific humidity. Bottom-left: vertical wind. Bottom-right: sub-grid kinetic energy. All data presented refer to the same single realization in time. . . . .	25

2.3	Three-dimensional wind fields obtained at the center of the LES sub-domain for the $\sim 11.5$ hours of simulation. Top: zonal wind. Middle: meridional wind. Bottom: vertical wind. . . . .	26
2.4	Simple schematic of the basic principles of a radar. (a) A pulse is transmitted into space. (b) The pulse reaches the target. (c) The target scatters in all directions. (d) Some of the energy is reradiated towards the antenna and delivered to the receiver. . . . .	27
2.5	Block Diagram of a homodyne Doppler Radar. The RF signal generated by the STALO is modulated, amplified, and transmitted into space by the antenna. The received signal is “mixed” with the same RF from STALO, filtered, processed, and finally, displayed for the user. . . . .	28
2.6	Block Diagram of a heterodyne Doppler Radar. A difference from the homodyne system presented in Figure 2.5 is the generation of the RF frequency by combining the STALO and COHO signals. The received signal is mixed with the STALO to obtain an IF signal. This IF signal is sampled by a digital receiver, where matched filtering, baseband conversion and phase referencing for coherent-on-receive operation are realized by digital signal processing hardware and software. . . . .	29
2.7	Idealized traces for the radar signal (adapted from (Doviak and Zrnić 1993)). Each trace represents a composite of echoes for each transmitted pulse. Instantaneous samples are taken at $T_{r1}$ , $T_{r2}$ , etc. The red stars represent a probable time dependence of the sample at $T_r$ . Samples at fixed $T_r$ taken at $T_s$ intervals are used to construct the Doppler spectrum from targets located at approximately the range $cT_r/2$ . . . . .	31
2.8	Simple diagram of the Kolmogorov turbulence spectrum (adapted from Pope (2000)). The energy spectrum of turbulence $E(\kappa)$ and wavenumber $\kappa$ axes are in logarithmic scale. In the inertial subrange, the large eddies from the energy-containing range cascade into the small eddies in the dissipation range following a slope of $-5/3$ . . . . .	36
2.9	Schematic of the Doppler spectrum. $S$ represents the signal power, $N$ is the noise power (usually assumed “white”), $v_r$ is the mean radial velocity, and $\sigma_v$ represents the Doppler spectral width. . . . .	40
2.10	Schematic of the autocorrelation function. Top: magnitude of the ACF. Signal power is represented by $S$ , $N$ is the noise power. Bottom: phase of the ACF. The radial velocity $v_r$ is calculated based on the phase of the ACF at lag 1 ( $\tau = 1$ ). . . . .	41
2.11	Schematic of the calculations of radial velocity $v_r$ as a function of the three wind field components. Left: the radial velocity is expressed as a function of the horizontal velocity and the vertical wind field. Right: the horizontal velocity is expressed as a function of the zonal and meridional wind fields. . . . .	44
2.12	Schematic of the Doppler Beam Swinging Technique. DBS uses at least three non-coplanar beams to estimate the three components of the wind field under the assumptions of homogeneity and stationarity during the time of the scan. . . . .	45

2.13	Normalized autocorrelation ( $c_{11}(\tau)$ ) and cross-correlation ( $c_{12}(\tau)$ ) functions. $\hat{\eta}$ represents the decorrelation parameter, $\hat{\tau}_p$ is the peak time of CCF, $\hat{\tau}_c$ is the square root of the second central moment of CCF, and $\tau_x$ is the lag such that $ c_{11}(\tau_x)  =  c_{12}(0) $ . . . . .	47
3.1	Left: scheme that represents an off-vertical pointing beam. The dotted lines represent the radial from the location of the radar to the grid points of the LES within the resolution volume. Along these dotted lines, $C_n^2$ is calculated, and later weighted in range ( $W_r$ ) and beam width ( $W_b$ ). Right: the dotted line represents the axis along which $C_n^2$ needs to be estimated. First, the value of $n$ at level $z$ is obtained from the LES matrix; however, at levels $z + \Delta z$ and $z - \Delta z$ , the dotted line does not match any of the LES grid points. In order to obtain an estimate at those heights, a linear interpolation is made using the four closest points. Finally, an average of the two estimates of structure function parameter of $n$ (from $z$ and $z + \Delta z$ , and $z$ and $z - \Delta z$ ) with an oblique separation $\Delta$ is computed. . . . .	52
3.2	Left: vertical profile of specific humidity characteristics for the CBL. Center: vertical profile of refractivity calculated from the LES fields. Right: vertical profile of the horizontally averaged structure function parameter of refractive index $C_n^2$ . All data were calculated from a single realization in time. . . .	53
3.3	Time-series data from the simulated BLR data $V(t)$ obtained at a range of 475 m. The blue line represents the real part (in-phase) of $V(t)$ , and the red line is the imaginary part (quadrature) of $V(t)$ . Top: without AWGN. Bottom: with AWGN (minimum SNR = -3 dB). . . . .	57
3.4	Schematic of the monostatic radar configuration. The simulated radar has the capability to point at any desired azimuth and zenith angle provided the resolution volume is located within the LES sub-domain. . . . .	58
3.5	Doppler beam swinging configuration. The configuration is based in a single monostatic radar that points in five different, non-coplanar directions. Usually, the oblique beams point to the four cardinal directions. . . . .	60
3.6	Multiple monostatic radar setup. The configuration uses the assumption that five simultaneous monostatic radars point towards the same resolution volume inside the LES. . . . .	61
3.7	Spaced Antenna Setup. This experiment uses one antenna for transmission and three or more for reception. The distance between the transmitter (Tx) and receivers (RxA and/or RxB) is small, so it allows the beams to intercept. The different transmitter and receiver beamwidths have been incorporated in the radar simulator. Here, the beamwidth is exaggerated for diagram purposes. . . . .	63
4.1	Picture of the Radial Wind Profiler (RWP) located at the SGP ACRF. In addition to the wind profiles, the system can obtain virtual temperatures through the Radio Acoustic Sounding System (RASS) co-located with the radar (Courtesy of Dr. P. Chilson). . . . .	65

4.2	Structure function parameter of the refractive index estimates on June 8, 2007. Top: estimates from the vertical beam of the radar simulator. Middle: LES-profile at center of domain. Bottom: estimates from the vertical beam of the SGP ACRF radar. . . . .	67
4.3	Zonal wind estimates averaged every 12 min on June 8, 2007. Top: LES-DBS. Middle: LES-Profile at center of domain. Bottom: DBS estimates from the SGP ACRF radar. . . . .	69
4.4	Meridional wind estimates averaged every 12 min on June 8, 2007. Top: LES-DBS. Middle: LES-Profile at center of domain. Bottom: DBS estimates from the SGP ACRF radar. . . . .	70
4.5	Vertical wind estimates averaged every 12 min on June 8, 2007. Top: LES-DBS. Middle: LES-Profile at center of domain. Bottom: DBS estimates from the SGP ACRF radar. . . . .	71
4.6	Wind comparison from the RadSim <sub>DBS</sub> , LES, Radar <sub>ARM</sub> , and a sounding (launched at three different times: 12:00, 18:00, and 00:00 UTC) at ~530 m (left) and ~1030 m (right) on June 8, 2007. Top: zonal wind. Middle: meridional wind. Bottom: vertical velocity. . . . .	72
4.7	Vertical velocity variance as a function of height for different periods of time from left to right (14:00-16:00; 16:00-18:00; 18:00-20:00; and 20:00-22:00 UTC). Red line: estimates from the virtual BLR. Blue line: estimates from the LES. Black line: estimates from the BLR located at the SGP ACRF site. The horizontal dashed line represents the CBL top obtained from the LES $C_n^2$ maximum averaged over the period under study. . . . .	74
4.8	Skewness of the vertical velocity as a function of height for different periods of time from left to right (14:00-16:00; 16:00-18:00; 18:00-20:00; and 20:00-22:00 UTC). Red line: estimates from the virtual BLR. Blue line: estimates from the LES. Black line: estimates from the BLR located at the SGP ACRF site. The horizontal dashed line represents the CBL top obtained from the LES $C_n^2$ maximum averaged over the period under study. . . . .	76
5.1	Zonal wind estimates obtained using DBS for different shear conditions. Left: $sfrac = 0.00$ (no shear). Middle: $sfrac = 0.50$ . Right: $sfrac = 1.00$ . . . . .	82
5.2	Zonal wind bias. Line: Ideal bias. Dots: estimated from the DBS simulation for different values of $sfrac$ . . . . .	83
5.3	Diagram showing the location of the SA transmitter (Tx) and receivers (RxA, RxB, RxC, and RxD). The black dots represent the location of the four receivers in the cross-configuration. As noted, they are located symmetrically, with respect to the Tx, along the zonal and meridional axes. . . . .	84
5.4	Zonal wind estimates obtained using SA for different shear conditions. Left: $sfrac = 0.00$ (no shear). Middle: $sfrac = 0.50$ . Right: $sfrac = 1.00$ . . . . .	85
5.5	Zonal wind bias. Line: Ideal bias. Dots: estimated from the SA simulation for different values of $sfrac$ . . . . .	86
5.6	Top: Signal-to-Noise Ratio as a function of time. The asterisks represent estimates of the BL top. Bottom: censored SNR plot. Values less than -3 dB and above the BL top have been removed. . . . .	87

5.7	Zonal wind estimates as a function of time for $sfrac = 1.00$ . Top: LES estimates. Middle: DBS estimates. Bottom: SA estimates obtained from the FCA-Gaussian method. The first height is removed for DBS, and the first three heights for SA. . . . .	89
5.8	Same as Figure 5.7, except for the meridional wind. . . . .	90
5.9	Comparison between the DBS estimates versus LES fields. Top: zonal wind for different $sfrac$ values. Bottom: meridional wind for the same $sfrac$ values. Left: $sfrac = 0.00$ . Middle: $sfrac = 0.50$ . Right : $sfrac = 1.00$ . . . . .	91
5.10	Error analysis as a function of time for $sfrac = 1$ . Top: zonal wind error from DBS estimates. Middle-top: range corrected zonal shear from LES. Middle-bottom: meridional wind error from DBS estimates. Bottom: range corrected meridional shear from LES. . . . .	92
5.11	Error from the DBS estimates vs. range corrected shear from LES for $sfrac = 1.00$ . Left: zonal wind. Right: meridional wind. . . . .	93
5.12	Wind bias for DBS. Left: zonal wind. Right : meridional wind. . . . .	94
5.13	Comparison between the SA estimates vs. LES fields. Top: zonal wind for different $sfrac$ values. Bottom: meridional wind for the same $sfrac$ values. Left: $sfrac = 0.00$ . Middle: $sfrac = 0.50$ . Right : $sfrac = 1.00$ . . . . .	94
5.14	Error analysis as a function of time for $sfrac = 1$ . Top: zonal wind error from SA estimates. Middle-top: range corrected zonal shear from LES. Middle-bottom: meridional wind error from DBS estimates. Bottom: range corrected meridional shear from LES. . . . .	95
5.15	Error from the SA estimates vs. range corrected shear from LES for $sfrac = 1.00$ . Left: zonal wind. Right: meridional wind. . . . .	96
5.16	Wind bias for SA. Left: zonal wind. Right: meridional wind. . . . .	97
5.17	Horizontal velocity variances. Gray lines: time spread of plane statistic estimates from the LES over a one-hour period. Black: statistics obtained from LES data over the entire BLR domain by plane averaging and additional time averaging over one hour. Red: velocity variances calculated by time averaging from LES data over the DBS volume scan. Blue: velocity variance estimated from an ideal DBS setting (all beams available at dwell time of 30 s). Green: velocity variance estimated from a realistic DBS setting (all beams available after the scan time of 150 s). Statistics in the two upper plots are evaluated with original vertical velocities ( $sfrac = 1$ ). Statistics in the two lower plots are obtained with zero vertical velocity ( $sfrac = 0$ ). . .	100
5.18	Horizontal velocity variances. For notation see Figure 5.17. The averaging time for the DBS estimates is 1200 s instead of 150 s. . . . .	101
5.19	Left: vertical velocity variance. Right: turbulence kinetic energy. For notation see Figure 5.17. . . . .	101

5.20	Kolmogorov turbulence spectra obtained from the velocity fields. The subscript represents the longitudinal $l$ or the transverse $t$ component, and the superscript represents the velocity component. All five components are presented as a time average obtained between 18:00-19:00 UTC at approximately 700 m. The black dashed line represents the $-5/3$ law expected from isotropic turbulence (see Section 2.2.3.2). All spectra behave similarly, which confirms the isotropy in the LES fields. Also, the transverse spectrum is larger than the longitudinal spectrum, which is consistent with the structure parameter in the inertial subrange. The beginning of the dissipation range can be identified as $\approx 157$ m, which is caused by dumping in the sub-grid closure of the LES model. . . . .	104
5.21	Turbulence eddy dissipation rate as a function of time and height. Top: estimates from LES. Middle-top: estimates from the Doppler spectrum width of the signal from the vertical beam. Middle-bottom: estimates from the Doppler spectrum width of the signal from the oblique beam pointing to the north. Bottom: estimates from the Doppler spectrum width of the signal from the oblique beam pointing to the east. . . . .	106
5.22	Hourly averages of turbulence eddy dissipation rate profiles from 16:00 - 17:00. Left: estimates from the virtual BLR with different directed beams (red: vertical beam; blue: east beam; green: north beam; cyan: west beam; magenta: south beam). Right: $\epsilon$ profile from the LES (black) compared to the profile from BLR averages among different beam directions (red). . . .	107
5.23	Same as Figure 5.22, except with time averaging over period 17:00 - 18:00 UTC. . . . .	108
5.24	Same as Figure 5.22, except with time averaging over period 18:00 - 19:00 UTC. . . . .	108
5.25	Same as Figure 5.22, except with time averaging over period 19:00 - 20:00 UTC. . . . .	109
C.1	Scheme that describes the calculations of $C_n^2$ at each LES cell. The difference in refractive index $\Delta n_k$ is calculated at edge of the cube considering the refractive index at each vertex. The length of each of the twelve edges of the cube corresponds by the LES grid spacing $\Delta$ . . . . .	138

## Abstract

The boundary layer (BL) is the lowest part of the atmosphere where the flow field is directly influenced by interactions among air, heat, and the Earth's surface. The structure of flow in the BL is dynamic due to the fact that the atmospheric flow is turbulent. Turbulence in the daytime convective boundary layer (CBL) is primarily caused by buoyancy forced from the heated underlying surface. Wind profilers are one of the many instruments used to study and characterize the atmosphere. In addition to in-situ observations, numerical large-eddy simulations (LES) have been probed to adequately reproduce the CBL under different conditions. The focus of this work is to bring the advantages of LES techniques to assist in the interpretation of data from wind profilers.

The present study focuses on an example of flow structure of the CBL as observed in the U.S. Southern Great Plains Atmospheric Radiation Measurement Climate Research Facility in Lamont, Oklahoma on June 8, 2007. The considered CBL flow has been reproduced using LES, sampled with a LES-based virtual boundary layer radar (BLR), and probed with an actual operational wind profiler. The LES-generated CBL flow data are then ingested by the virtual BLR and treated as a proxy for prevailing atmospheric conditions. The virtual BLR has been used to simulate radar signals obtained from wind profilers through the synthesis of Doppler beam swinging (DBS) and spaced antenna (SA) techniques and to retrieve the three-dimensional wind fields. Comparisons of the estimates of the structure parameter of refractive index  $C_n^2$ , wind fields, vertical velocity variance, and vertical velocity skewness have been presented for the LES, virtual BLR, and actual radar.

It has been observed that during the presence of strong horizontal shear of vertical velocity, the estimates of the horizontal wind fields are biased. This study will quantify the effect of this shear for both wind estimation techniques under different conditions. Additionally, it has been noticed that this shear also biases the estimates of turbulence kinetic energy (TKE) calculated from the variances of the wind fields. Finally, the TKE (eddy) dissipation rate  $\epsilon$  can be obtained from radar estimates of

Doppler spectral width. Values of  $\epsilon$  are obtained from the different oblique and vertical beams and contrasted with the LES estimates obtained through a parameterized expression that relates the dissipation rate to sub-grid TKE and turbulence length scale.

# Chapter 1

## Introduction

### 1.1 The Atmospheric Boundary Layer: A Brief Review

The Earth's atmosphere is a layer of gases surrounding the planet that is retained by its gravity (Ahrens 1991; Stull 2000; Wallace and Hobbs 2006). The atmosphere protects life on Earth by absorbing ultraviolet solar radiation which warms the surface through heat retention (greenhouse effect) and reduces temperature extremes between day and night. The atmosphere is a complex fluid system (Stull 2000) which generates chaotic motions known as weather. In 340 B.C., Aristotle defined *Meteorologica* as the study of the weather and climate, as well as astronomy, geography, and chemistry. Today, *Meteorology* is the study of the atmosphere and its phenomena. Some of the most intensely studied topics include all parts of severe weather: thunderstorm, clouds, rain, snow, wind, hail, lightning, and hurricanes (Ahrens 1991). In the absence of precipitation, *Meteorology* studies changes in temperature, winds, air turbulence, etc.

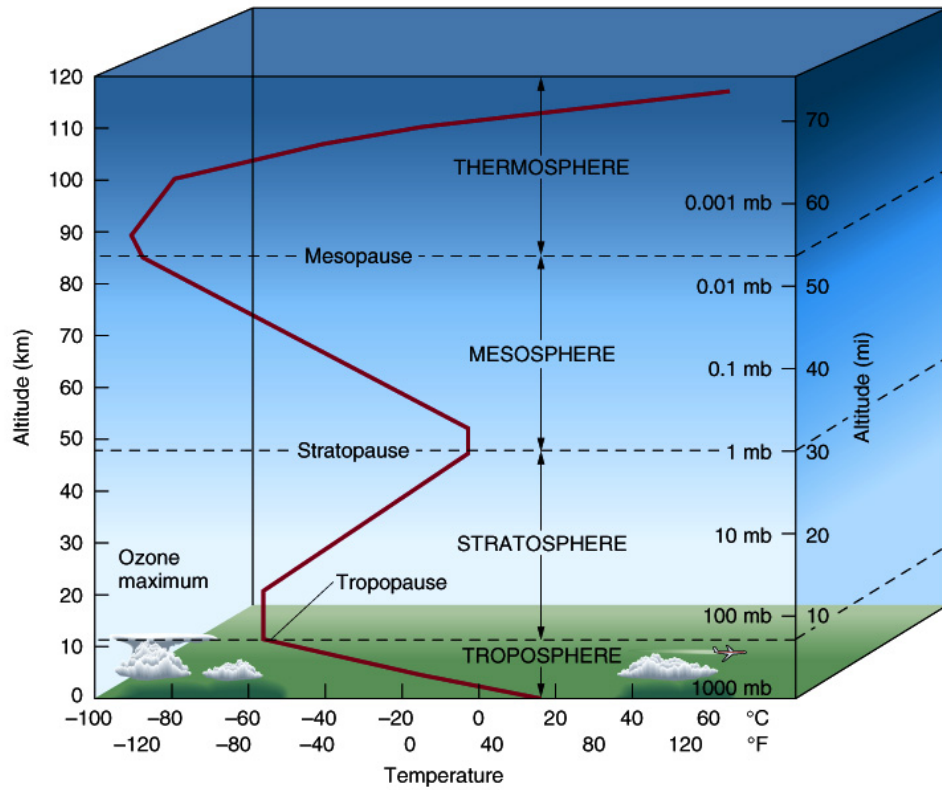
The atmosphere is composed of a mixture of gases in proportions shown in Table 1.1. Nitrogen and Oxygen are the main constituents of the Earth's atmosphere, and their percentage remains constant from the surface up to approximately 80 km (Ahrens 1991; Wallace and Hobbs 2006). Consequently, there is a balance between production and destruction of these gases near the surface. Nitrogen is removed from the atmosphere by biological processes that involve soil bacteria. It is returned to the atmosphere mainly through the decay of plant and animal matter. Oxygen, on the other hand, is removed from the atmosphere when organic matter decays and when oxygen combines with other substances, producing oxides. The oxygen returns to the atmosphere through photosynthesis (Ahrens 1991). Argon is present in higher

concentrations than other noble gases like neon, helium, krypton, and xenon. Water vapor accounts for approximately 0.25% of the mass of the atmosphere, and its concentration varies from 10 ppmv (parts per million per volume) in the coldest regions of the Earth's atmosphere up to 5% by volume ( $5 \times 10^{-4}$  ppmv) in hot and humid air masses (Wallace and Hobbs 2006). Ozone concentrations also have large variabilities, and a concentration of greater than 0.1 ppmv is considered dangerous to human health.

Table 1.1: Fractional concentration by volume of the major constituents of the Earth's atmosphere up to 105 km, with respect to dry air (from Wallace and Hobbs (2006)).

Constituent	Molecular weight	Fractional concentration by volume
Nitrogen (N <sub>2</sub> )	28.013	78.08%
Oxygen (O <sub>2</sub> )	32.000	20.95%
Argon (Ar)	39.95	0.93%
Water vapor (H <sub>2</sub> O)	18.02	0-5%
Carbon dioxide (CO <sub>2</sub> )	44.01	380 ppm
Neon (Ne)	20.18	18 ppm
Helium (He)	4.00	5 ppm
Methane (CH <sub>4</sub> )	16.04	1.75 ppm
Krypton (Kr)	83.80	1 ppm
Hydrogen (H <sub>2</sub> )	2.02	0.5 ppm
Nitrous oxide (N <sub>2</sub> O)	53.02	0.3 ppm
Ozone (O <sub>3</sub> )	48.00	0 - 0.1 ppm

The structure of the atmosphere indicates changes in temperature, density, and composition with height and is depicted in Figure 1.1. The lowest layer of the atmosphere is the troposphere, which extends from the surface up to approximately 7 km at the poles and 17 km at the equator. The troposphere is mostly heated by transfer of energy from the surface, so on average the lowest part of the troposphere is warmest and the temperature decreases with altitude. The rate at which temperature decreases with height is called adiabatic lapse rate, and its value can be found by combining the first law of thermodynamics, the equation of state for ideal gas, and the hydrostatic balance equation ( $\Gamma_d \sim 9.8^\circ\text{C km}^{-1}$ ) (Holton 2004; Wallace and Hobbs 2006). If the atmospheric lapse rate  $\Gamma$  is lower than the adiabatic lapse rate ( $\Gamma < \Gamma_d$ ),



<http://burro.cwru.edu/Academics/Astr201/Atmosphere/atmosphere1.html>

Figure 1.1: The structure of the Earth's atmosphere (modified from Ahrens (1991)). The structure reflects how temperature, density, and composition of the atmosphere change with height, and how it is determined in large part by how it interacts with the sun's light.

an air parcel that undergoes an adiabatic displacement from its equilibrium level will be positively buoyant when displaced downward and negatively buoyant when displaced upward so that it will tend to return to its equilibrium level, and the atmosphere is said to be *statically stable*. *Static stability* considers only buoyancy to estimate the flow stability, and ignores shears in the mean wind. The air parcel is considered *unstable*, if the buoyant force is in the same direction as the displacement. This instability causes the air parcel to continue accelerating in the initial direction of movement. This results in convective circulations and convective clouds (Stull 2000). This promotes the vertical mixing of gases. The troposphere also contains all weather that we are familiar with on Earth. The boundary between the troposphere and stratosphere is called the tropopause.

The stratosphere extends from the tropopause up to approximately 50 km. Temperature increases with height, which restricts turbulence and mixing. Stratospheric air is extremely dry and ozone rich. The absorption of solar radiation in the ultraviolet region of the spectrum by this *stratospheric ozone layer* is critical to the inhabitability of the Earth (Wallace and Hobbs 2006). The stratopause, which is the boundary between the stratosphere and mesosphere, is typically at 50 - 55 km. The mesosphere extends from the stratopause up to 80 - 85 km. This is the layer where most meteors ablate upon entering the atmosphere. Temperature decreases with height in the mesosphere. A phenomenon due, in part, to the fact that there is little ozone in the air to absorb solar radiation. Hence, the molecules are able to lose more energy than they absorb, which results in an energy deficit and cooling (Ahrens 1991). The mesopause, the temperature minimum that marks the top of the mesosphere, is the coldest region of the Earth and has an average temperature around  $-85^{\circ}\text{C}$ . Due to the cold temperature of the mesosphere, water vapor can be frozen, which might allow for the formation of ice clouds (or Noctilucent clouds). Temperature increases with height in the thermosphere from the mesopause up to the thermopause due to the absorption of solar radiation in association with the dissociation of diatomic nitrogen and oxygen molecules and the stripping of electrons from atoms (Wallace and Hobbs 2006). These process is known as photodissociation and photoionization. Temperatures in the Earth's outer thermosphere can change over a wide range due to variations in the emission of ultraviolet and x-ray radiation from the sun's outer atmosphere.

The Atmospheric Boundary Layer (ABL) is the lowest part of the troposphere in which the flow field is directly influenced by interactions with the Earth's surface (Holton 2004). For average midlatitude conditions, the atmospheric Convective Boundary Layer (CBL) extends through the lowest kilometer and thus contains about 10% of the mass of the atmosphere. The structure of the flow in the boundary layer is dynamic due to the fact that the atmospheric flow is turbulent. The CBL depth produced by turbulent transport may range from as little as 30 m in conditions of large static stability to more than 3 km in highly convective conditions. Vertical shears can be extremely intense within a few millimeters of the surface, which continuously leads to the development of turbulent eddies.

In the daytime CBL, turbulence is primarily forced by surface heating, radiational cooling from clouds at the CBL top, or by both mechanisms. A pure buoyancy-driven CBL rarely exists, and there are many situations in which surface heating is relatively weak while the turbulence production by wind shears is relatively strong. In these cases, the shear effects on the CBL turbulence dynamics cannot be ignored (Conzemius and Fedorovich 2006).

The CBL is considered clear when no clouds are present (Holtslag and Duynkerke 1998). A clear CBL is the focus of this study. The bottom of the CBL is called the *surface layer* and extends upwards from 20 to 200 m. In this layer, frictional drag, heat conduction, and evaporation from the surface cause substantial changes in wind speed, temperature, and humidity with height (Stull 2000). This layer is also known as the *constant flux layer* because the turbulent fluxes are relative uniform with height. In this case, the CBL's main forcing mechanism is surface heating. Turbulent convective motions in the CBL transport heat upward in the form of convective plumes or thermals. These rising motions and associated downdrafts effectively mix momentum and potential temperature fields in the middle portion of the CBL (Zilitinkevich 1991). The resulting *mixed layer* is typically the CBL's thickest sublayer. The CBL is topped by the *entrainment zone*, which has relatively large vertical gradients of averaged (in time or over horizontal planes) meteorological fields. Above the *entrainment zone* is the rest of the troposphere, also called the *free atmosphere* (see Figure 1.2).

The *entrainment zone* is often called the interfacial or capping inversion layer because it is co-located with the region of maximum gradients in the potential temperature profile. This stable layer traps turbulence, pollutants, and moisture below it and prevents most of the surface friction from being felt by the free atmosphere. The height of the capping inversion is usually denoted by  $z_i$  and is frequently a measure

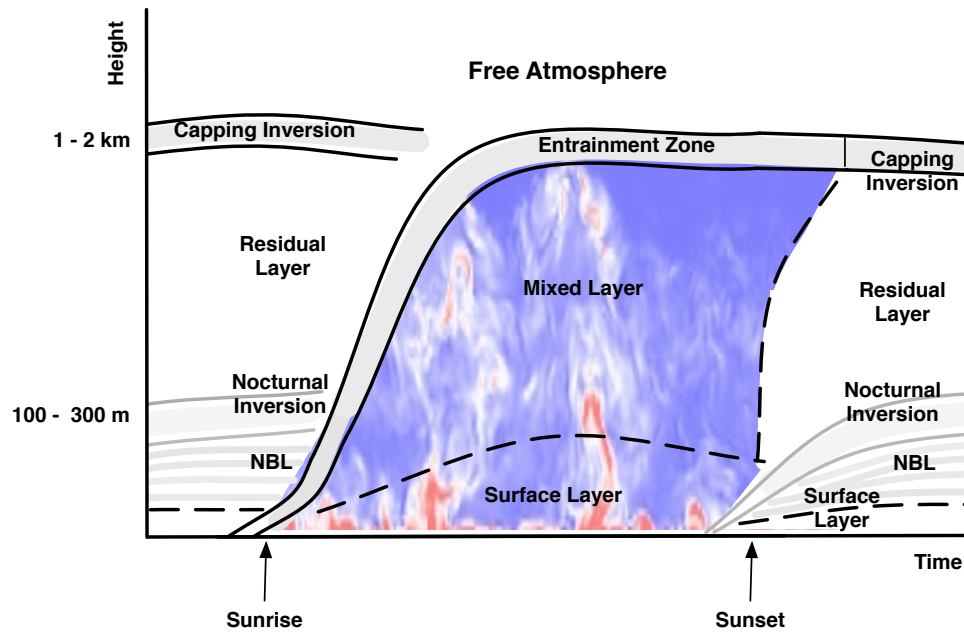


Figure 1.2: Depiction of the diurnal development of the atmospheric boundary layer (adapted from Stull (1988)).

of the CBL depth. Many quantities within the CBL can be scaled with this value (Deardorff 1970). These include mean flow parameters (mean wind speed, potential temperature, and specific humidity), turbulent fluxes of momentum, heat, and moisture, and variances of the velocity components and passive scalars. As a consequence, accurate estimates of  $z_i$  are extremely important in any study of CBL structure. A detailed understanding of the CBL is important for numerical weather prediction and climate modeling applications. The turbulence contained in the CBL is an important transport mechanism of heat, pollutants, and momentum.

## 1.2 Radars for Sensing the Atmosphere

One of the many instruments that is used to study the atmosphere is radar (RAdio Detection And Ranging) (Doviak and Zrnić 1993). There are many other uses for radars such as detection of military targets, radar-assisted ground-controlled approach (GCA) systems in airports, radar guns used by police to monitor vehicle speeds on the roads, etc. Radars use electromagnetic waves to irradiate and measure the observed fields. The returned signal is used to infer the properties of the atmosphere. Doppler

radars can detect tracers of wind and measure their radial velocities, both in the clear-air and/or within regions of precipitation. Depending on the type of scattering mechanism, radars can be separated as weather or clear-air radars. There have been many studies that summarize their characteristics (Doviak and Zrnić 1993; Balsley and Gage 1982; Rinehart 2004). Nevertheless, a short review is provided here.

### 1.2.1 Weather Radars: Particle Scattering From Precipitation

Precipitation refers to all liquid or solid phase aqueous particles that originate in the atmosphere and fall to the Earth's surface (*AMS Glossary*). They are usually identified as rain, sleet, hail, snow, and any other form of water falling from the sky. The scattering mechanism of electromagnetic radiation by spherical particles is called *Mie scattering*. Hydrometeors correspond to this type of scattering. However, when their size is much smaller than the radar wavelength, they correspond to a sub-set of the Mie theory called *Rayleigh scattering*.

Radar was not developed by one person, it was the product of the effort of many. Hertz, Marconi, Tesla, Thompson, Edison, Braun, and many others can all be credited with contributing to the invention of radar (Dunlap Jr. 1946). It is difficult to trace the first radar detection of precipitation, but it is likely to have been in the latter half of the 1940s (Atlas 1990; Doviak and Zrnić 1993), during World War II when Britain invested more than \$41.5 million in radar technology, which corresponds to more 500 million in today's dollars (Dunlap Jr. 1946). This new technology allowed Britain's Royal Air Force to intercept the German Luftwaffe at night through fog and clouds. The use of radar definitely aided the Allies in their victory over Germany and Japan, and it also saved countless lives.

Today, Doppler radars are commonly used for weather observations. Weather radars come in a variety of designs and use different frequencies such as X-band (8-12 GHz), C-band (4-8 GHz), and S-band (2-4 GHz), depending on the application. Mobile radars usually operate at X-band due to its low cost and relatively good resolution. However, they are susceptible to suffer from severe attenuation and range-velocity ambiguity. Range-velocity ambiguity refers to the inability of a pulsed Doppler radar to resolve range and velocity without aliasing (Rinehart 2004). Most stationary radars operate at S-band due to their low attenuation and less severe range-velocity ambiguity. Nonetheless, they are expensive and less sensitive (e.g. WSR-88D (Weather Surveillance Radar - 1998 Doppler) sensitivity is -7.5 dBZ at 50 km). Radars that operate at C-band are mobile and stationary systems alike due

to their low cost and higher sensitivity (e.g. OU PRIME (Polarimetric Radar for Innovations in Meteorology and Engineering) sensitivity is -18 dBZ at 50 km).

There are many weather radar networks around the world. The European weather radar network (Operational Program for the Exchange of weather RADar information – OPERA) standard is a C-band Doppler radar, although the Spanish network is composed of C- and S-band Doppler radars. Italy operates several polarimetric C-band Doppler radars for local applications (Meischner 2004). A map of the location of the current radars operated by OPERA is presented in Figure 1.3.

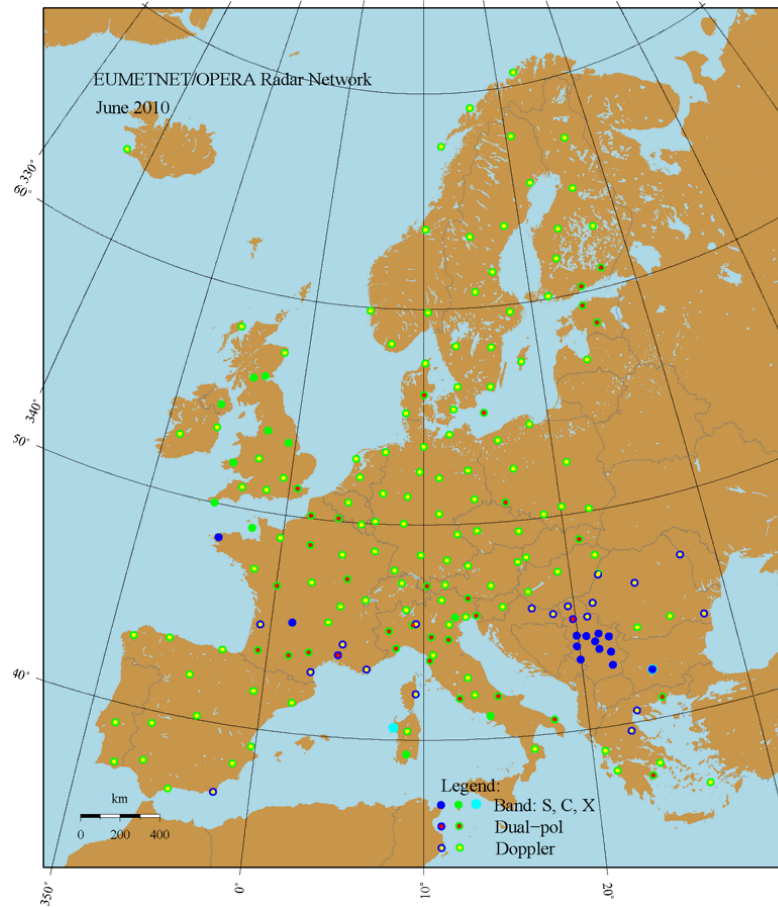


Figure 1.3: Location of radars present at the OPERA radar database updated in June 2010 (from <http://www.knmi.nl/opera/>). The color dots represent the frequency bands: C-band = green, S-band = blue, X-band = cyan. The center color represent the type of radar: dual polarization radar = red center, Doppler radar = yellow center.

The United States weather radar network is composed of 154 WSR-88D (Next-Generation Radar - NEXRAD) S-band radars (see Figure 1.4) and is operated by the National Weather Service, the Federal Aviation Administration (FAA), and the

Department of Defense (DOD) (Rinehart 2004). The WSR-88D (see left panel of

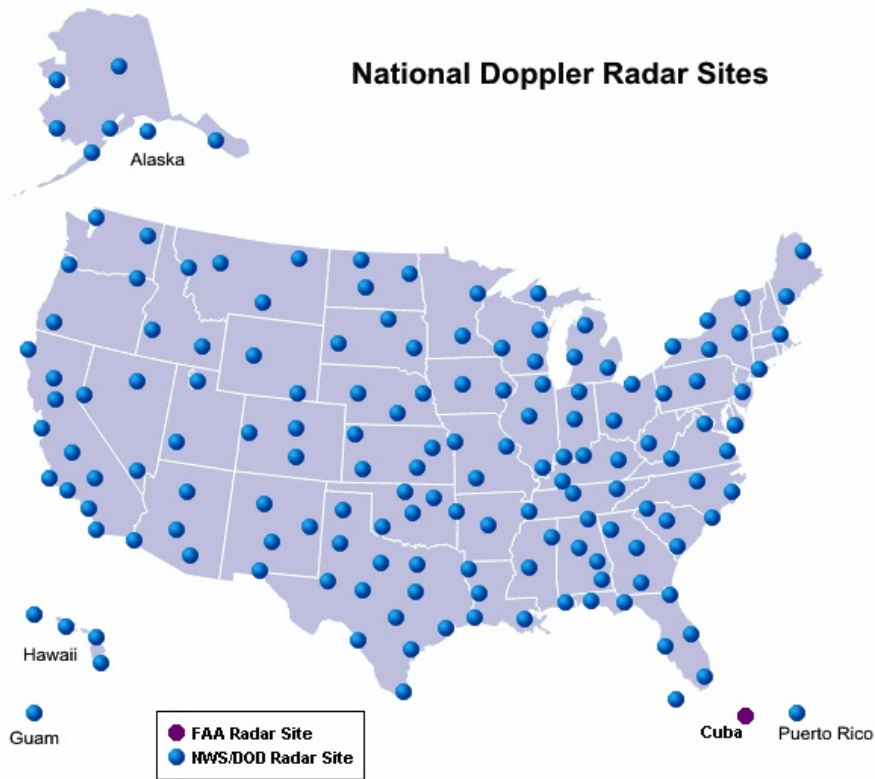


Figure 1.4: Location of the operational WSR-88D radars (National Oceanic and Atmospheric Administration (NOAA) 2007 (from <http://radar.weather.gov/>)). The color coding represent the US agency in charge of the correct operation of the radar.

Figure 1.5) began as the Joint Doppler Operational Project (JDOP) in 1976 at the National Severe Storms Laboratory (NSSL) in Norman, Oklahoma (OK) (Crum and Alberty 1993). The goal was to create a national network of Doppler radars to improve the detection of hazardous storms, tornados, and squall lines. The program was an effort put forth by the three U.S. agencies sharing common interests in the capabilities of the radar: Department of Commerce (DOC), DOD, and the Department of Transportation (DOT). Installation of the network began with the first WSR-88D constructed near Oklahoma City, OK in 1990.

The WSR-88D systems collect, process, and display high-resolution and high accuracy reflectivity, radial velocity, and spectrum width continuously. The antenna scans its environment in predefined sequences of  $360^\circ$  azimuthal sweeps at various angles or *volume coverage patterns* (VCP). A complete multiple elevation sequence is

a volume scan (Crum and Alberty 1993). Typical VCPs used by the WSR-88D are presented in Table 1.2.

Table 1.2: Example of typical VCPs utilized by the WSR-88D based on the type of weather occurring (from <http://www.wdtb.noaa.gov/tools/RPS/>).

VCP	Tscan (min)	Elev. scans	Elevation angles (°)	Usage
11	5	14	0.5, 1.5, 2.4, 3.4, 4.3, 5.3, 6.2, 7.5, 8.7, 10, 12, 14, 16.7, 19.5	Convection, especially when close to the radar
12	4.5	14	0.5, 0.9, 1.3, 1.8, 2.4, 3.1, 4, 5.1, 6.4, 8, 10, 12.5, 15.6, 19.5	Convection, especially activity at longer ranges
21	6	9	0.5, 1.5, 2.4, 3.4, 4.3, 6, 9.9, 14.6, 19.5	Shallow precipitation
32	10	5	0.5, 1.5, 2.5, 3.5, 4.5	Default clear-air mode, reduces wear on antenna

The WSR-88D network will be start to be modified for dual polarization operations in 2011 (Istok et al. 2009). This new technology will allow the WSR-88D radars to simultaneously transmit and receive in horizontal and vertical polarization. Dual polarization provides a unique tool for classification of radar echoes. Having dual polarization capability is essential for weather discrimination and classification of different hydrometeor types like rain, hail, graupel, and snow of different types. The dual polarization technology has been the subject of research since the 1970's. However, it was not until the Joint Polarization Experiment (JPOLE) that the technology was demonstrated to provide significant benefits to the forecaster. During JPOLE, using a prototype dual polarimetric WSR-88D, hydrometeor classification was tested using fuzzy logic algorithms (Ryzhkov et al. 2005b). The version of hydrometeor classification algorithm (HCA) which will be implemented on the WSR-88D radars is described in Park et al. (2009). This algorithm includes the estimation of a data quality index that is an indicator of many possible sources of error in the radar measurements, the assignment of a matrix of weights that sets values to the radar retrieval according to its importance to the variable to retrieve, and implementation of class designation based on the distance from the radar and the parameters of the melting layer which are determined as a function of azimuth with polarimetric radar

measurements (Istok et al. 2009). The Melting Layer Detection Algorithm (MLDA) is part of the HCA, and was tested using S-band radar in OK (Giangrande et al. 2008) and C-band in Ontario, Canada (Boodoo et al. 2008). The performance and robustness of the MLDA was proven in both conditions (Istok et al. 2009). Finally, the quantitative precipitation estimation (QPE) algorithm (Ryzhkov et al. 2005a) was optimized by combining QPE and HCA in the second version of the polarimetric QPE algorithm (QPE v2) which was validated using the Oklahoma Mesonet for 43 events (Giangrande and Ryzhkov 2008).

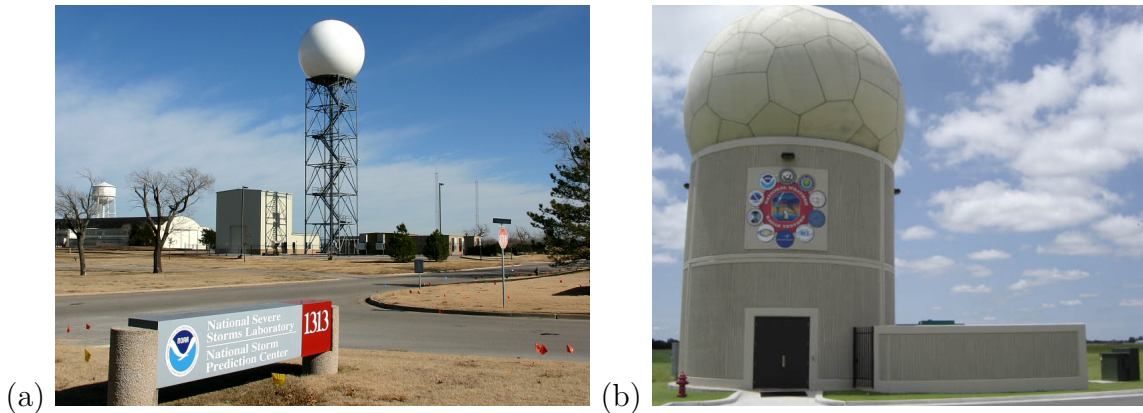


Figure 1.5: (a) NEXRAD Radar at the WSR-88D Radar Operations Center in Norman, OK (from <http://en.wikipedia.org/wiki/NEXRAD>). (b) Phased-Array Radar (PAR) in Norman, OK (from [http://www.thunderchaser.com/june2005/spc\\_tour.html](http://www.thunderchaser.com/june2005/spc_tour.html)).

As mentioned previously, the WSR-88D scans the volume in sequences of  $360^\circ$ , and depending on the VCP and the current weather conditions, the total time for a volume scan is approximately 4.5 minutes. However, it is convenient to revisit regions of interest more frequently and other regions less frequently maintaining adequate data quality. These constitute a limitation for conventional weather radars due to the mechanic inertial of the rotating antennas. The Phased-Array Radar (PAR) or the National Weather Radar Testbed (NWRT) is presented in the right panel of Figure 1.5 and has a unique antenna that collects the same information as a conventional radar in about one-fourth the time. The S-band radar has a 10-cm wavelength and is being used in studying and developing faster and more accurate severe and hazardous weather warnings (Forsyth et al. 2005; Heinselman et al. 2008; Zrnić et al. 2007). The PAR is able to electronically steer in both elevation and azimuth within a  $45^\circ$  cone-shaped volume. An advantage of the system is its capability to change the beam pointing direction from pulse to pulse, which allows the system to be used in weather forecast

and primary aircraft surveillance. This could be an alternative to current surveillance radars (e.g. WSR-88D) (Weadon et al. 2009). The system was developed by an interactive group from government and industry organizations (Forsyth et al. 2002) consisting of NSSL and Radar Operations Center (ROC), the United States Navy's Office of Naval Research, Lockheed Martin Corporation, the University of Oklahoma, the Oklahoma State Regents for Higher Education, and the FAA's Technical Center. The PAR was installed successfully in September 2003, and started full operational data collection in May 2005.

It has demonstrated in Heinselman et al. (2008) that the NWRT PAR can achieve high temporal volumetric resolution. Its time improvement over a conventional WSR-88D scan is at least four times. This high temporal resolution is necessary for rapid identification and confirmation of weather phenomena. Also, the beam multiplexing (BMX) technique has been tested and implemented on the NWRT (Yu et al. 2007; Zrnić et al. 2007). This approach improves the scan time by changing the pointing direction, which reduces the time to achieve independent samples. In both approaches, the time to obtain a volume scan was significantly reduced in comparison with a WSR-88D, which opens more possible uses for the PAR.

The Multifunction Phased-Array Radar (MPAR) system is a specialized application of general phased array radar technology that is designed to simultaneously fulfill the multiple functions of national air and weather surveillance (Weadon et al. 2009). The MPAR system will be able to improve meteorological forecasts and warnings and reduce the number of existing radars by combining meteorological and air surveillance functions into a single system. This also will reduce the cost of maintaining the current systems, and in time MPAR will become more affordable. Due to the capability of instantaneously and dynamically controlling beam position on a pulse-by-pulse basis, the MPAR system can perform both tasks with different update times to achieve the goal of better characterizing and forecasting the storms of interest. In order to achieve both tasks at the same time, an algorithm based on the concept of time balance (TB) was developed for adaptive weather sensing (Reinoso-Rondinel et al. 2010). A simulated experiment was conducted to test the feasibility of the technique and to test the performance of the TB scheduling algorithm. As a result, the storm of interest was scanned more frequently within a relatively short period time compared to conventional scanning while air surveillance was done "simultaneously".

## 1.2.2 Profiling Radars: Clear-Air Scattering from Refractive Index Variations

Wind profilers are pulsed Doppler radars that transmit radio waves vertically or nearly vertically. They receive backscattered signals from refractive index fluctuations in clear-air (Bragg scattering). These fluctuations are caused by variations in temperature, humidity, and electron density of the atmosphere. The contribution of the latter is only observed in the upper atmosphere.

The history of clear-air radars started during the same period of weather radars in which “angel echoes” were recorded when no precipitation was present (Baldwin 1948; Friend 1949). There were discrepancies regarding the origin of the echoes; insects and birds were one possibility, and sharp gradients in refractive index were another (Atlas 1990). Since 1950 there has been significant exploration of the clear-air echoes with different radar wavelengths and for long periods of time. From 1963 to 1972 there were notable achievements in detection of clear-air turbulence in ranges up to 10-20 km with 10 cm or longer wavelength radars (UHF). Atlas and Hardy (1966) conducted an experiment at Wallops Islands with 3.2-, 10.7-, and 71.5-cm radars to study the atmosphere. Through the use of range-height-intensity (RHI) displays, they discovered that some of the “angel echoes” that appeared between 1 and 3 km were seen most prominently with the 3.2-cm radar and not with the 71.5-cm radar, which indicates that these targets were small compared to the radar wavelength, and led to the conclusion that the return signals were from insects and/or birds. Atlas and Hardy (1966) also discovered a layer around 1 km that was clearly observed with the 10.7- and 71.5-cm radars, but it was more intensely observed with the 10.7-cm radar. This layer was clearly caused by variations in the refractive index (Hardy et al. 1966). Also, using low elevation plan-position-indicator (PPI) plots Hardy and Ottersten (1969); Konrad (1970); Harrold and Browning (1971), with the 10.7-cm radar, were able to study convective processes in the boundary layer. The first Frequency-Modulated Continuous-Wave (FM-CW) radar (Richter 1969; Gossard and Richter 1970) was built in the late 1960s, pointed vertically, and had a resolution of 1 m. The main contribution from the use of FM-CW radar is the understanding of Kelvin-Helmholtz instabilities and the interaction of instabilities on a variety of scales (Atlas 1990).

Woodman and Guillen (1974) obtained Doppler wind velocities both in the lower atmosphere and mesosphere with the 50 MHz (VHF) radar located at the Jicamarca

Radio Observatory near Lima, Peru. The Jicamarca radar was previously used primarily for ionospheric research. After this discovery at Jicamarca, many researchers recognized the potential of VHF radars for exploring the clear atmosphere, from the lower troposphere up to the mesosphere ( $\sim 100$  km) (Atlas 1990). Consequently, the radar wavelengths to study the clear-air atmosphere were switched from the UHF to VHF. These new VHF radars were typically phase-array antennas which often operated unattended at low power. Many radars were built as a direct result of the Jicamarca research such as the 53 MHz SOUSY (SOUnding SYstem) radar in the Harz, Germany, the 50 MHz Poker Flat radar in Alaska (no longer in operation), the 46 MHz MU (Middle and Upper atmosphere) radar in Shigaraki, Japan; and the 53 MHz Gadanki radar in Tirupati, India. Some of these VHF radars are presented in Figure 1.6. Today, this type of radar usually operates in frequencies between 50 MHz

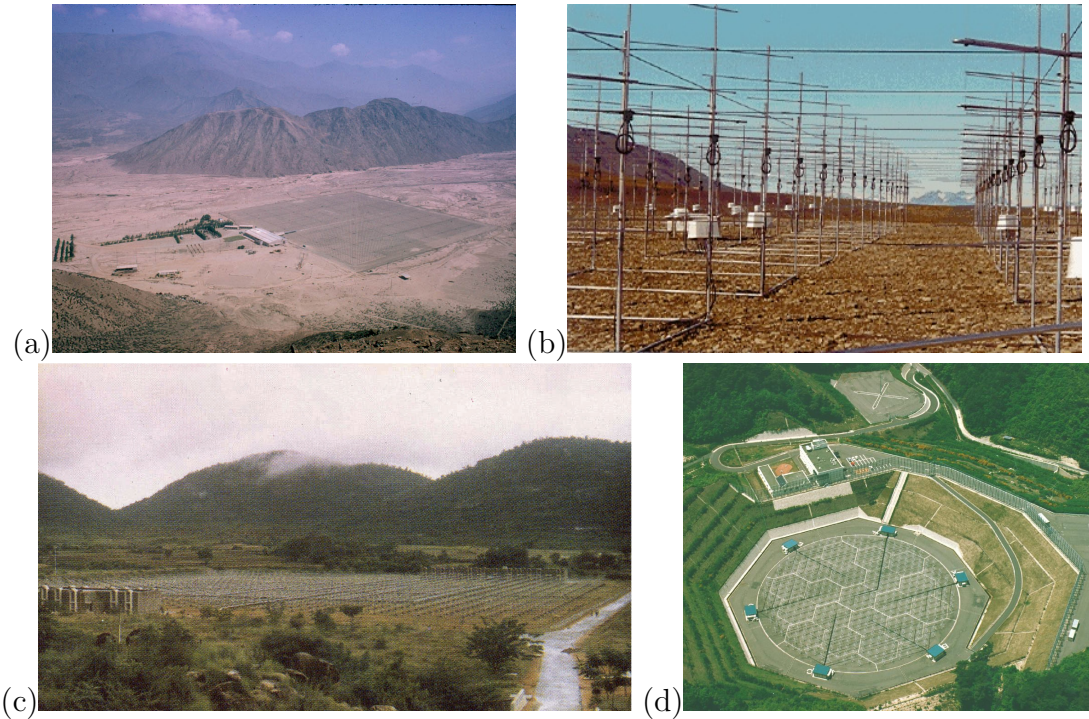


Figure 1.6: (a) Jicamarca Incoherent Scatter Radar at Lima, Peru (from <http://jro.igp.gob.pe>). (b) The SOUSY (SOUnding SYstem) Radar at Lindau, Germany (from <http://radars.uit.no/sousy/index.html>). (c) NARL MST Radar at Gadanki, India (from <http://www.narl.gov.in/>). (d) MU (Middle and Upper atmosphere) Radar at Shigaraki, Japan (from [http://www-lab26.kuee.kyoto-u.ac.jp/study/mu/mu\\_e.html](http://www-lab26.kuee.kyoto-u.ac.jp/study/mu/mu_e.html)).

and 1 GHz (VHF and UHF frequencies - see Figure 1.7), and they can be classified depending on their altitude coverage (see Table 1.3):

Table 1.3: Classification of radars according to their altitude coverage

Type of radar	Approximate range
MST (Mesosphere, Stratosphere, and Troposphere)	4 km - 85 km
ST (Stratosphere and Troposphere)	2 km - 22 km
BLT (Boundary Layer and Troposphere)	300 m - 8 km
BL (Boundary Layer)	200 m - 2 km

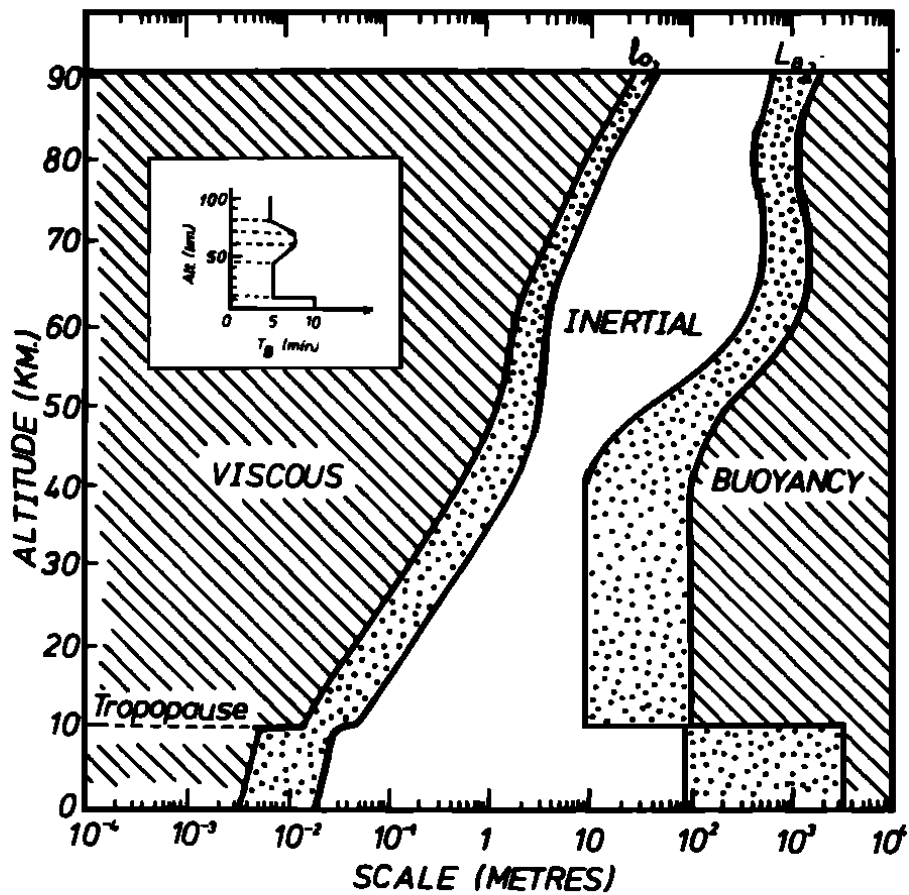


Figure 1.7: Schematic of the evolution of the inertial subrange with height. The horizontal axis represent the Bragg scale. In the troposphere, the Bragg scale extends safety from  $10^{-1}$  to 10 m, which corresponds to frequencies of 1.5 GHz (UHF) - 15 MHz (VHF), respectively (from Hocking (1985)).

To study the ABL, boundary layer radars (BLR) have been developed in the UHF band near 1 GHz and in the S-band with frequencies near 3 GHz (Van Zandt 2000). The S-band radars are more susceptible to hydrometeor, and they often cannot measure the vertical wind and the estimation of horizontal winds is difficult. Consequently, the UHF frequency is more common in clear-air studies. The UHF radar detects irregularities in the refractive index when the Bragg condition is met. This condition refers to scattering waves when continuous turbulent interfaces are in phase, and constructive interference provides a maximum in the intensity of the resulting wave. Therefore, the Bragg scale is such that BLRs are sensitive to turbulent structures with spatial scales near  $15 \text{ cm}$  ( $\lambda/2$ , where  $\lambda$  is the radar wavelength).

Enhanced refractive index variations are often associated with the *entrainment zone* just above the CBL, which can be detected by clear-air radar. There have been many studies in which BLRs are used to estimate the CBL depth and thickness of the entrainment layer (e.g., Angevine et al. 1994b; Angevine 1999; Cohn and Angevine 2000; Grimsdell and Angevine 2002). A good estimate of the CBL depth is important to understand the evolution and also for simulations of the CBL (Angevine et al. 1994b). Continuous profiles of the wind vector directly above the instrument can be obtained using the Doppler beam swinging (DBS) method (Balsley and Gage 1982). Due to its frequency of operation, as mentioned before, BLRs are also sensitive to Rayleigh scatter from hydrometeors and are used to study clouds and precipitation (e.g., Atlas and Hardy 1966; Hardy and Ottersten 1969; Konrad 1970; Harrold and Browning 1971; Gage et al. 1994; Ecklund et al. 1995). Thus, the BLR can be used to study the boundary layer under a wide variety of meteorological conditions and has been proven invaluable for such investigations (e.g., Rogers et al. 1993; Angevine et al. 1994b; Wilczak et al. 1996; Dabberdt et al. 2004). However, for cloud-free CBL studies, precipitation might be seen as signal contamination.

Another radar used in the ABL studies is the previously mentioned FM-CW. This radar differs from the conventional pulsed radars in that utilizes the Doppler frequency shift to detect moving targets (Skolnik 2001), and it requires a large bandwidth (a wide-frequency spread). Calculations of the radial velocity are very complicated in FM-CW radars. Strauch (1976) implemented a Doppler processing technique that uses a data acquisition system developed for pulsed Doppler radar for the extraction of the Doppler spectrum. Nevertheless, this radar has been used to show that the thermodynamic fields within the CBL can exhibit a high degree of complexity and that organized fine-scale structures with spatial scales of roughly one meter are

common (Richter 1969; Gossard and Richter 1970; Eaton et al. 1995). In contrast to FW-CW radars, BLRs must operate within stringent frequency management constraints, which limits their range resolution. The typical range resolution for BLR measurements of the ABL is approximately 100 m. This resolution is too coarse to adequately reproduce the entrainment zone’s embedded spatial structure. Several multiple frequency techniques have been introduced in the past as a means of improving the range resolution (e.g., Kuddeki and Stitt 1987; Palmer et al. 1990, 1999; Yu and Palmer 2001; Luce et al. 2001). These techniques use several close frequencies for transmission and reception, and after post-processing, the coarse original range resolution was improved. The minimum layer thickness obtained by Chilson et al. (2003) was 16 m. Multiple-frequency techniques have also been successfully used to study the ABL at UHF (Chilson et al. 2003; Chilson 2004; Yu and Brown 2004).

### 1.3 Large-Eddy Simulations to Characterize the Atmospheric Boundary Layer

In addition to field observations of the CBL by *in-situ* and remote sensing measurement methods, numerical simulation approaches – specifically, the large-eddy simulation (LES) technique – are widely employed to study physical processes in the atmospheric CBL. Large-eddy simulations of CBL-type flows have developed into a routine scientific exercise over the last three decades, see Deardorff (1972); Moeng (1984); Mason (1989); Schmidt and Schumann (1989); Moeng and Sullivan (1994); Sorbjan (1996, 2004); Khanna and Brasseur (1998); Sullivan et al. (1998); Van Zan-ten et al. (1999); Fedorovich et al. (2001, 2004a); Conzemius and Fedorovich (2006). These cited works are indicative of how the LES has gradually evolved into an applied research technique in CBL studies. However, the relation of LES to observations of the CBL, as well as to conceptual CBL models or theories, needs further examination and quantitative evaluation (Wyngaard 1998; Stevens and Lenschow 2001).

The LES method is based on the numerical integration of filtered equations of flow dynamics and thermodynamics, which resolves most of the energy-containing scales of turbulent transport. Any unresolvable motions are assumed to carry only a small fraction of the flow’s total energy and are parameterized with a subgrid (or subfilter) closure scheme. In the LES of the atmospheric CBL, environmental parameters such as surface heating, stratification, and shear can be precisely controlled. Retrieval of spatial turbulence statistics in LES do not necessarily rely on additional

assumptions like the Taylor (1938) frozen-turbulence hypothesis, which states that thermodynamic and kinematic properties of the simulated flow are known at all points of the numerical grid simultaneously. In this manner, LES has been a helpful tool in studying the statistics of (resolved) CBL turbulence and in visualizing its turbulent structure. However, the applicability of LES in atmospheric boundary layer studies is limited by the subgrid model's ability to adequately describe the subgrid motions' effect on the filtered (resolved) fields. This is the compromise to simulate turbulence in larger domains with heterogeneous turbulence properties. Also, like all numerical approaches based on temporal and spatial discretization of the governing flow equations, LES is subject to various numerical artifacts including: phase speed errors, artificial viscosity, and dispersion errors.

## 1.4 Motivation for Dissertation

A thorough understanding of the CBL is of significant importance in meteorological studies. One of the most important parameters used in scaling the CBL parameters is the CBL depth  $z_i$  or inversion layer height. However, there are discrepancies when this height is obtained from radar measurements (Botnick and Fedorovich 2008). A close comparison of this parameter can be obtained through the combination of LES and a LES-based radar simulator. Under these conditions, the gap between numerical simulations and remote sensing methods will be addressed.

Turbulence parameters needing quantification are the turbulence kinetic energy (TKE) and energy eddy dissipation rate ( $\epsilon$ ). Studies of  $\epsilon$  have been made from radar measurements of the return radar backscatter (Hocking 1983, 1985, 1992; Hocking and Mu 1997) and Doppler spectral width (Hocking 1983, 1985; White 1997; White et al. 1999; Jacoby-Koaly et al. 2002). However, these studies have been developed for the troposphere and stratosphere and have never been applied to the CBL. Also, derivations from the radar backscattering were made under stable conditions which consider gradients of potential refractive index profiles, and due to the high level of turbulence present in CBL, only the estimates obtained from the Doppler spectral width are suitable in CBL studies.

Horizontal wind components obtained from DBS or Spaced Antenna (SA) techniques have been found to be biased by the horizontal shear of vertical velocity, and depending on the level of the shear present in the CBL, estimates can be significantly

biased (Flowers et al. 1994; Zhang and Doviak 2007). Three-dimensional wind estimates have been obtained from both DBS and SA techniques for different levels of shear and compared with the theoretical formulation. Later, with the combination of LES and LES-based radar simulator, the bias was estimated for realistic conditions.

By definition, estimates of TKE have to be obtained from the variance of the three-dimensional winds. TKE estimates from LES will be compared and contrasted with the ones obtained from radar simulator measurements to find to what extent the estimates from radar are comparable with those commonly used in fluid dynamics (Stull 1988). Also, the influence of the horizontal shear of vertical velocity in the TKE estimates will be studied for different time averaging schemes.

## 1.5 Outline of Dissertation

Following the introduction, a more in-depth review of Doppler radars and LES is presented in Chapter 2, including scattering mechanisms and signal processing. In Chapter 3, a radar simulator based on LES is described, along with the different experimental setups and techniques that will be used to characterize the CBL. Estimations of turbulence parameters based on the virtual radar such as structure function parameter of refractive index  $C_n^2$ , three-dimensional wind fields ( $u$ ,  $v$ , and  $w$ ), vertical velocity variance  $\sigma_w^2$ , and the vertical velocity skewness are presented in Chapter 4. Here, these parameters are compared with estimates obtained from an operational wind profiler located in Lamont, OK. In Chapter 5, the effect of horizontal shear of vertical velocity on horizontal wind estimations will be studied, along with turbulence kinetic energy and turbulence-eddy dissipation rate for different conditions. The dissertation concludes in Chapter 6 with an assessment of the suitability of the radar estimates for the characterization of the CBL and future work recommendations.

## Chapter 2

# Large-Eddy Simulations and Doppler Radars: Theoretical Background

## 2.1 Large-Eddy Simulations

The LES code used in this work was developed following the methodology described in Nieuwstadt (1990), Fedorovich et al. (2004b,a), and Conzemius and Fedorovich (2006). This code was extensively tested in comparison with several other representative LES codes and with experimental data for clear CBLs with and without wind shear (Fedorovich et al. 2004b; Fedorovich and Conzemius 2008). The LES was found to confidently reproduce turbulence structure for a broad variety of flow regimes observed in the clear CBL. In its last version, the code was revised, optimized, and modified to incorporate realistic atmospheric sounding data retrieved from observations or larger-scale atmospheric model/analysis outputs (Botnick and Fedorovich 2008).

Following the established LES methodology adopted in atmospheric and engineering turbulence studies, motions in the simulated turbulent CBL flow are subdivided into larger-scale resolved motions. These motions are directly reproduced on the computational grid, and the smaller-scale so-called sub-grid motions are modeled through additional stress/flux terms in the discretized governing equations for the resolved quantities (Botnick and Fedorovich 2008). Here, the Einstein summation convention is used.

$$\begin{aligned} \frac{\partial \tilde{u}_i}{\partial t} &= -\frac{\partial \tilde{u}_i \tilde{u}_j}{\partial x_j} + g \frac{\tilde{\Theta}_v - \Theta_{v0}}{\Theta_{v0}} \delta_{i3} - \frac{\partial \tilde{\pi}}{\partial x_i} + f (\tilde{u}_j - u_{g_j}) \varepsilon_{ij3} \\ &\quad + \frac{\partial}{\partial x_j} \left[ \nu \left( \frac{\partial \tilde{u}_i}{\partial x_j} + \frac{\partial \tilde{u}_j}{\partial x_i} \right) - (\widetilde{u_i u_j} - \tilde{u}_i \tilde{u}_j) \right], \end{aligned} \quad (2.1)$$

$$\frac{\partial \tilde{u}_i}{\partial x_i} = 0, \quad (2.2)$$

$$\frac{\partial \tilde{\Theta}_v}{\partial t} = -\frac{\partial \tilde{u}_i \tilde{\Theta}_v}{\partial x_i} + \frac{\partial}{\partial x_i} \left[ \mu \left( \frac{\partial \tilde{\Theta}_v}{\partial x_i} \right) - (\widetilde{\Theta_v u_i} - \tilde{\Theta}_v \tilde{u}_i) \right], \quad (2.3)$$

where the tildes denote volume averaged (resolved) quantities,  $i, j = \{1, 2, 3\}$ ;  $t$  is time,  $x_i = (x, y, z)$  are the right-hand Cartesian coordinates,  $\tilde{u}_i = (\tilde{u}, \tilde{v}, \tilde{w})$  represent resolved velocity components,  $u_{g_{j=1,2}} = (u_g, v_g)$  are the geostrophic wind components,  $\nu$  is kinematic viscosity,  $\mu$  is molecular thermal diffusivity, and  $\tilde{\Theta}_v$  is resolved virtual potential temperature of dry-air that would have the same density as moist-air and is used as a convenient surrogate for density in buoyancy calculations (*AMS Glossary*). Components of subgrid kinematic momentum and subgrid heat fluxes are represented by  $\widetilde{u_i u_j} - \tilde{u}_i \tilde{u}_j$  and  $\widetilde{\Theta_v u_i} - \tilde{\Theta}_v \tilde{u}_i$ , respectively. Normalized pressure,  $\tilde{\pi}$ , is defined as  $\tilde{\pi} = (\tilde{p} - p_0) / \rho_0$ , where  $\tilde{p}$  is resolved pressure,  $p_0$  is hydrostatic atmospheric pressure,  $\rho_0$  is constant reference density, and  $\Theta_{v0}$  is constant reference potential temperature.

The sub-grid momentum and buoyancy flux are modeled in terms of the sub-grid eddy viscosity ( $K_m$ ) and the sub-grid eddy diffusivity ( $K_h$ ) (Deardorff 1980):

$$\widetilde{u_i u_j} - \tilde{u}_i \tilde{u}_j = \frac{2}{3} E \delta_{ij} - 2K_m \widetilde{s_{ij}}, \quad (2.4)$$

$$\widetilde{\Theta_v u_i} - \tilde{\Theta}_v \tilde{u}_i = -K_h \frac{\partial \tilde{\Theta}_v}{\partial x_i}, \quad (2.5)$$

where  $\widetilde{s_{ij}} = (\partial \tilde{u}_i / \partial x_j + \partial \tilde{u}_j / \partial x_i) / 2$  represents the deformation tensor for filtered velocity, and subgrid turbulence kinetic energy  $E$  is determined from the balance equation,

$$\frac{\partial E}{\partial t} + \frac{\partial \tilde{u}_i E}{\partial x_i} = 2K_m \widetilde{s_{ij}} \frac{\partial \tilde{u}_i}{\partial x_j} - K_h \frac{\partial \tilde{\Theta}_v}{\partial x_3} + \frac{\partial}{\partial x_i} \left[ 2K_m \frac{\partial E}{\partial x_i} \right] - \varepsilon, \quad (2.6)$$

where  $\varepsilon$  is the sub-grid TKE viscous dissipation rate. Eddy viscosity and diffusivity are expressed as

$$K_m = 0.12lE^{0.5}, \quad (2.7)$$

$$K_h = \left( 1 + \frac{2l}{\Delta} \right) K_m, \quad (2.8)$$

where  $\Delta = (\Delta x \Delta y \Delta z)^{1/3}$  is the effective grid-cell size, and  $l$  is the sub-grid mixing length. Finally,  $\varepsilon$  and  $l$  are evaluated as

$$\varepsilon = f_c \left( 0.19 + 0.51 \frac{l}{\Delta} \right) \frac{E^{3/2}}{l}, \quad (2.9)$$

$$l = \begin{cases} \Delta, & \frac{\partial \widetilde{\Theta}_v}{\partial z} \leq 0; \\ \min \left\{ \Delta, \frac{0.5\sqrt{E}}{\sqrt{\frac{\partial \widetilde{\Theta}_v}{\partial z}}} \right\}, & \frac{\partial \widetilde{\Theta}_v}{\partial z} > 0, \end{cases} \quad (2.10)$$

$$f_c = 1 + \frac{2}{\left( \frac{z_w}{\Delta z_w} + 1.5 \right)^2 - 3.3}, \quad (2.11)$$

where  $z_w$  is the distance from the ground, and  $\Delta z_w$  is the vertical dimension of the lowest grid cell.

A Poisson equation for  $\tilde{\pi}$  is constructed by combining the continuity and momentum balance equations as in Nieuwstadt (1990). The equation is solved numerically by the fast Fourier transform technique over horizontal planes and by tri-diagonal matrix decomposition in the vertical planes. Periodic boundary conditions for prognostic variables (velocity components, potential temperature, specific humidity, and  $E$ ) are prescribed on the simulation domain side-walls. In the upper 20% of the domain, a sponge layer is introduced in order to dampen vertical motions close to the domain top and to ensure steady-state conditions at the upper boundary. To minimize the sponge layer's inevitable spurious influence on the numerical solution, the time advancement is only maintained as long as the CBL depth is less than 70% of the domain height. The no-slip boundary condition for velocity and the zero-gradient condition for sub-grid energy are prescribed at the heated bottom surface. Monin-Obukhov similarity relationships are used point-by-point to couple local buoyancy and mechanical turbulence forcing within the lowest layer of grid cells. The surface roughness length, temperature, and moisture fluxes are prescribed as external parameters.

The LES was applied to reproduce a daytime CBL case observed at the Southern Great Plains (SGP) Atmospheric Radiation Measurement (ARM) Climate Research Facility (ACRF) in Lamont, OK (LMN), on June 8, 2007. The LES was initialized with realistic environmental profiles of horizontal velocity components  $u$  and  $v$ , potential temperature  $\Theta$ , and turbulent kinematic virtual heat flux  $\overline{w'\Theta'_v}$ . As schematically

indicated in Botnick and Fedorovich (2008), realistic environment settings should include multiple inversions (areas of high stability) and sharp wind changes with height (wind shears) typically observed in the atmosphere. The surface heat flux (see bottom panel of Figure 2.1b) reflects the solar heating evolution during the day. Represented in the top panel of Figure 2.1a, are the initialization profiles of wind and potential temperature. These profiles are kept constant above the CBL depth for the whole simulation. In the bottom panel of this figure is the surface heat flux for the simulation.

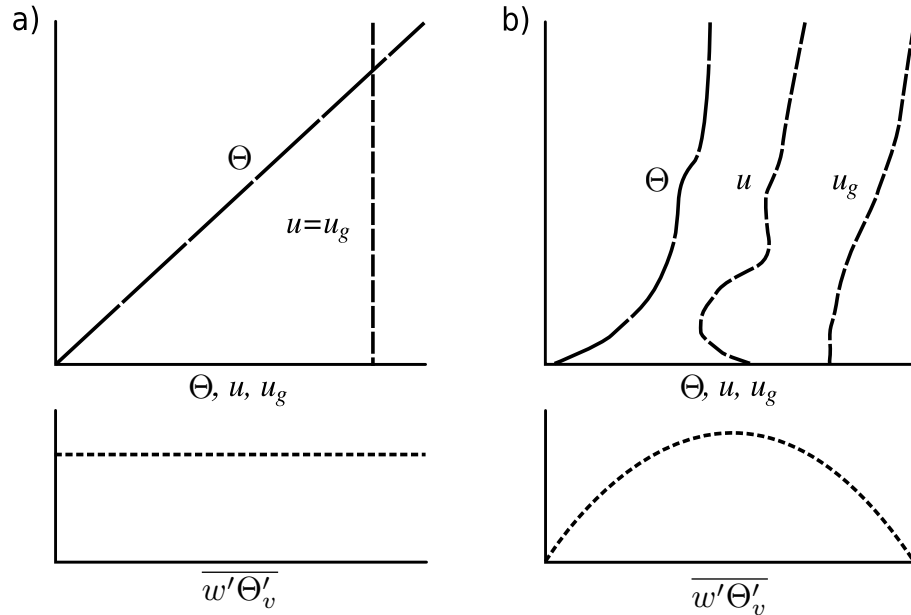


Figure 2.1: Schematic representation of idealized (a) and realistic (b) initial data (from Botnick and Fedorovich (2008)).

Surface fluxes of temperature and moisture were calculated from measured sensible  $H$  and latent  $LH$  heat fluxes using (Botnick and Fedorovich 2008):

$$\overline{w'\Theta'} = \frac{H}{\varrho_0 c_p}, \quad (2.12)$$

$$\overline{w'q'} = \frac{LH}{\varrho_0 L_v}, \quad (2.13)$$

$$\overline{w'\Theta'_v} = \overline{w'\Theta'} + 0.61\Theta_{v_0}\overline{w'q'}, \quad (2.14)$$

where  $\overline{w'\Theta'}$  is surface kinematic heat flux and  $\overline{w'q'}$  is surface kinematic moisture flux.  $c_p$  is specific heat for air, and  $L_v$  is latent heat of vaporization. Geostrophic wind components were evaluated from the Rapid Update Cycle (RUC) objective analysis data (Benjamin et al. 2004), which are available hourly. The geostrophic wind

is assumed to be height-constant. The geostrophic wind components are obtained through the calculation of horizontal gradients of pressure, which use four RUC grid points surrounding the LMN site.

$$u_g = \frac{-1}{\rho_0 f} \frac{\partial p}{\partial y}, \quad (2.15)$$

$$v_g = \frac{1}{\rho_0 f} \frac{\partial p}{\partial x}, \quad (2.16)$$

where  $f = 2\Omega \sin \Phi$  is the Coriolis parameter,  $\Omega$  is the Earth’s angular velocity,  $p$  is the surface pressure from RUC, and  $\Phi$  is the latitude. Wind profiles (obtained either from RUC and/or from the local sounding at LMN) are interpolated to the LES domain’s vertical nodes. Additionally, near-surface portions of these profiles are adjusted in order to match the no-slip condition at the surface, under the assumption of a logarithmic wind profile throughout the lowest LES cell layer. The simulation for the present study has been performed in a rectangular domain composed of 20 m grid cells. The LES settings are summarized in Table 2.1.

Table 2.1: Description of the LES settings

Parameter	Setting
Domain size	$5.12 \times 5.12 \times 4.0 \text{ km}^3$
Number of grid points	$256 \times 256 \times 200$
Spatial resolution	20 m
Time step	1 s
Output variables	Resolved $u, v, w, q$ , and $\Theta$ and E

The LES output included instantaneous fields of the filtered flow velocity components, potential temperature, specific humidity, and the sub-grid TKE are available with one-second time increments in the BLR sub-domain. Flow statistics were obtained locally by temporal averaging. Spatial statistics, obtained through horizontal planes averaging, were also included in the output. Evaluated statistics included mean flow variables, velocity, temperature, and humidity variances (both resolved and sub-grid), vertical fluxes of momentum, heat and moisture, and third-order moments of the resolved vertical velocity and temperature fields.

A sub-set of the LES output was employed as an input data-set for the virtual Boundary Layer Radar - BLR (see Chapter 3). This sub-domain had spatial limits

of  $1860 \text{ m} \leq X \leq 3260 \text{ m}$ ,  $1860 \text{ m} \leq Y \leq 3260 \text{ m}$ , and  $0 \text{ m} \leq Z \leq 2000 \text{ m}$ . The virtual BLR used three-dimensional fields of potential temperature  $\Theta$ , specific humidity  $q$ , sub-grid TKE  $E$ , and flow velocity components  $u$ ,  $v$ , and  $w$  along the coordinate directions  $x$ ,  $y$ , and  $z$ , respectively. A snapshot of the simulated CBL flow structure is given in Figure 2.2.

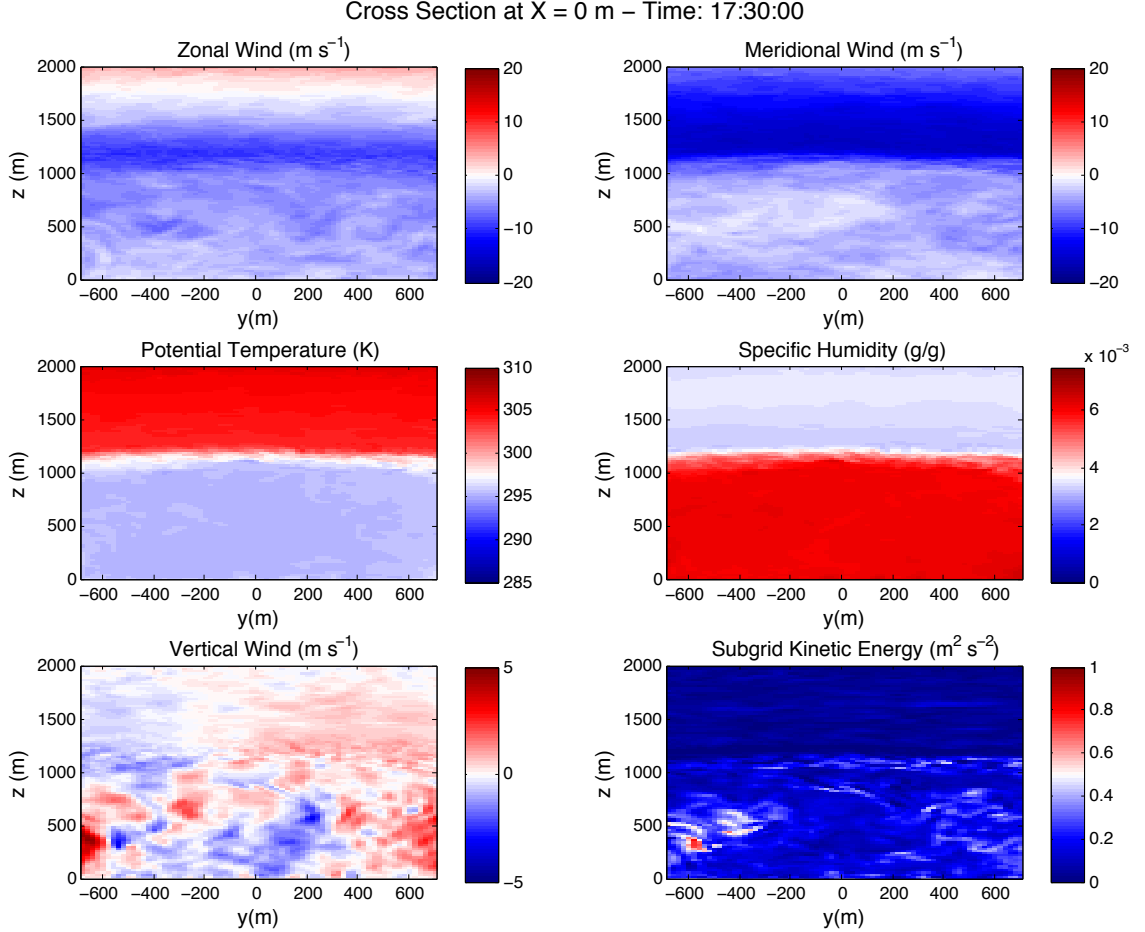


Figure 2.2: Examples of LES fields in the virtual radar sub-domain. Top-left: zonal wind. Top-right: meridional wind. Middle-left: potential temperature. Middle-right: specific humidity. Bottom-left: vertical wind. Bottom-right: sub-grid kinetic energy. All data presented refer to the same single realization in time.

The presented instantaneous flow fields illustrate the main features of the CBL turbulent flow structure. By its nature, the clear atmospheric CBL is a turbulent boundary layer whose turbulence is primarily forced by heating from the underlying surface. One may see an intensive turbulent mixing of momentum and scalar fields in the main portion of the CBL, beneath the capping inversion (seen in the plots as a zone

of sharp vertical gradients of potential temperature and specific humidity). Typically collocated with the capping inversion layer is the entrainment zone, through which the strongly turbulent CBL flow interacts with the relatively inactive free-atmospheric flow aloft. Another characteristic feature of the CBL flow is its coherent structure on larger scales that is represented by convective updrafts (thermals) and downdrafts which are clearly observed in the vertical velocity field pattern (see bottom panel of Figure 2.3). Rare, but more intense in comparison with downward motions, updrafts observed in the plot are indicative of positive skewness of vertical velocity in the atmospheric CBL.

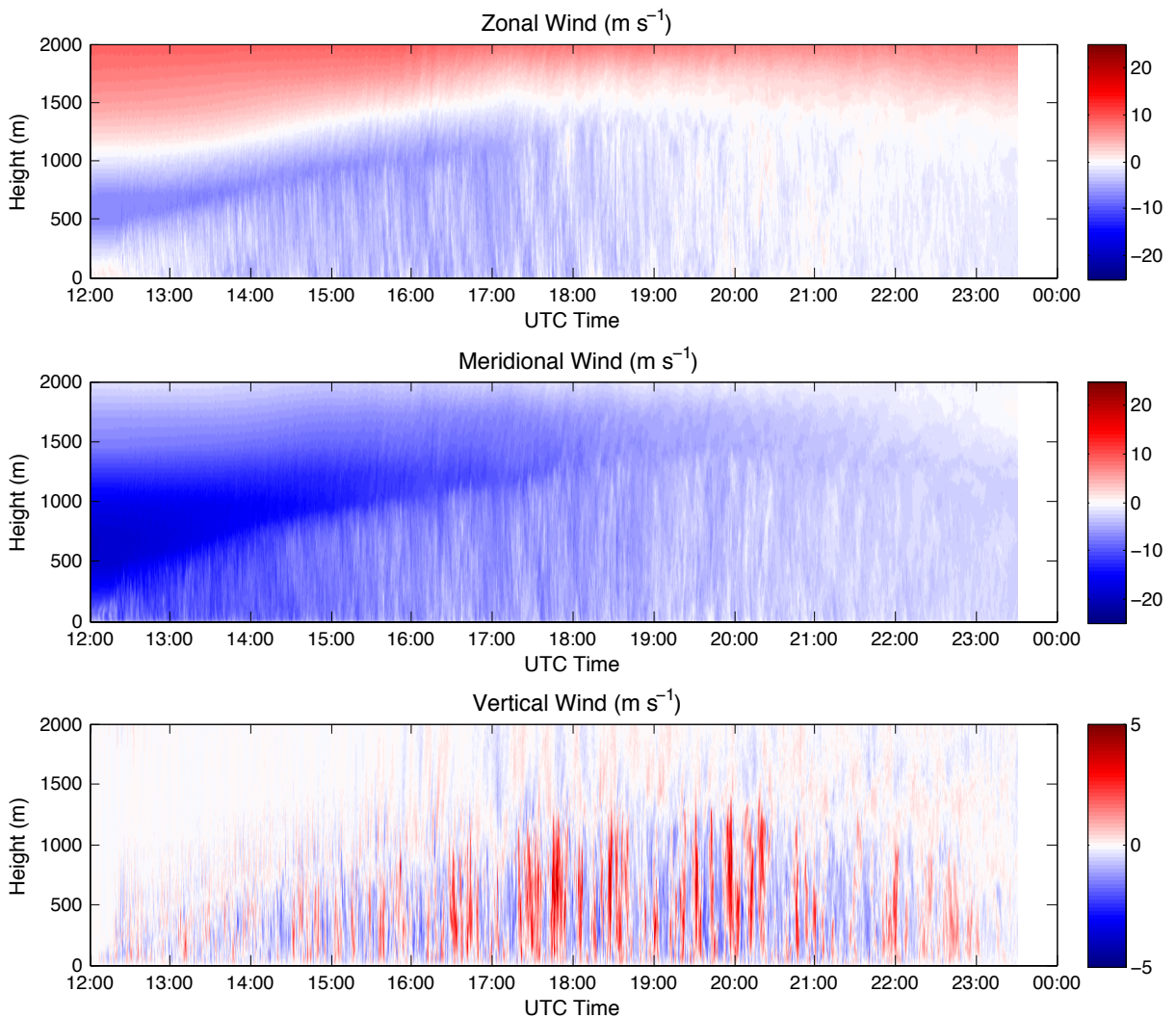


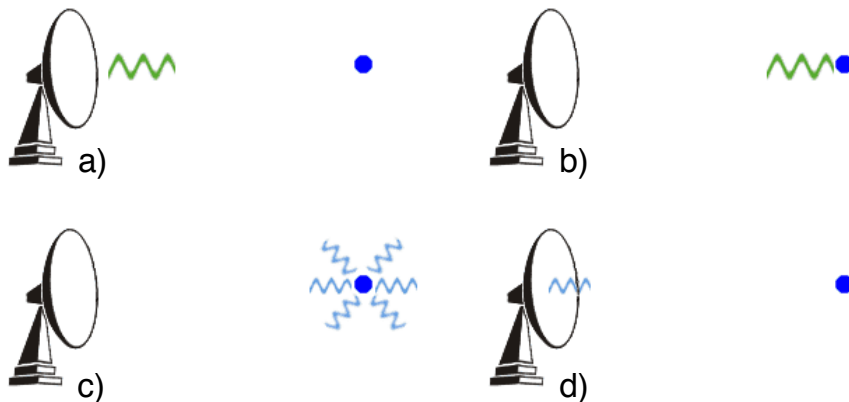
Figure 2.3: Three-dimensional wind fields obtained at the center of the LES sub-domain for the  $\sim 11.5$  hours of simulation. Top: zonal wind. Middle: meridional wind. Bottom: vertical wind.

## 2.2 Pulsed Doppler Radar

### 2.2.1 Basic Concepts

A radar is an electromagnetic system for detecting, locating, and characterizing reflective objects. These objects can be aircrafts, ships, spacecrafts, vehicles, people, and the natural environment (Skolnik 2001). Radars operate by radiating energy into space and detecting the echo signal reflected from an object or target. The returned echo indicates the presence of a target, as well as other valuable information, such as its distance from the radar, and information related to the target's size, and in some cases, its velocity relative to the radar. In most cases, a radar can operate both automatically and under extreme weather conditions.

The basic principle of operation is depicted in Figure 2.4. For illustrative purposes, only the antenna is depicted. A more detailed explanation of the design of a radar system is presented later in this section. An electromagnetic pulse is generated in the transmitter and radiated into space by the antenna (a). The pulse travels in space until it reaches the target (b). The transmitted energy is then intercepted by the target and reradiated in all directions (c). Some of this energy moves toward the antenna (d) and is delivered to the receiver. In a monostatic system, the transmitting and receiving antenna are the same. The system is considered bi-static if the antennas are physically separated.



Adapted from <http://weather.noaa.gov/radar/radinfo/radinfo.html>

Figure 2.4: Simple schematic of the basic principles of a radar. (a) A pulse is transmitted into space. (b) The pulse reaches the target. (c) The target scatters in all directions. (d) Some of the energy is reradiated towards the antenna and delivered to the receiver.

A simplified block diagram of a homodyne Doppler radar is presented in Figure 2.5. The stabilized local oscillator (STALO) generates a continuous wave (CW) signal that represents an almost perfect sinusoid (carrier frequency). This stable RF (radio frequency) signal is converted into a pulsed signal (on/off modulator). Once it has been modulated, the RF signal is amplified to produce intense microwave power (Doviak and Zrnić 1993). The amplified pulse is radiated into space by the antenna. The T/R switch has the important function of separating the transmitted pulse from the received signal. The received signal is “mixed” with the same RF signal which was used for the transmitter pulse obtained from the STALO. Through this coherent quadrature detection process, the so-called in-phase  $I(t, r_0)$  and quadrature  $Q(t, r_0)$  signals are obtained.

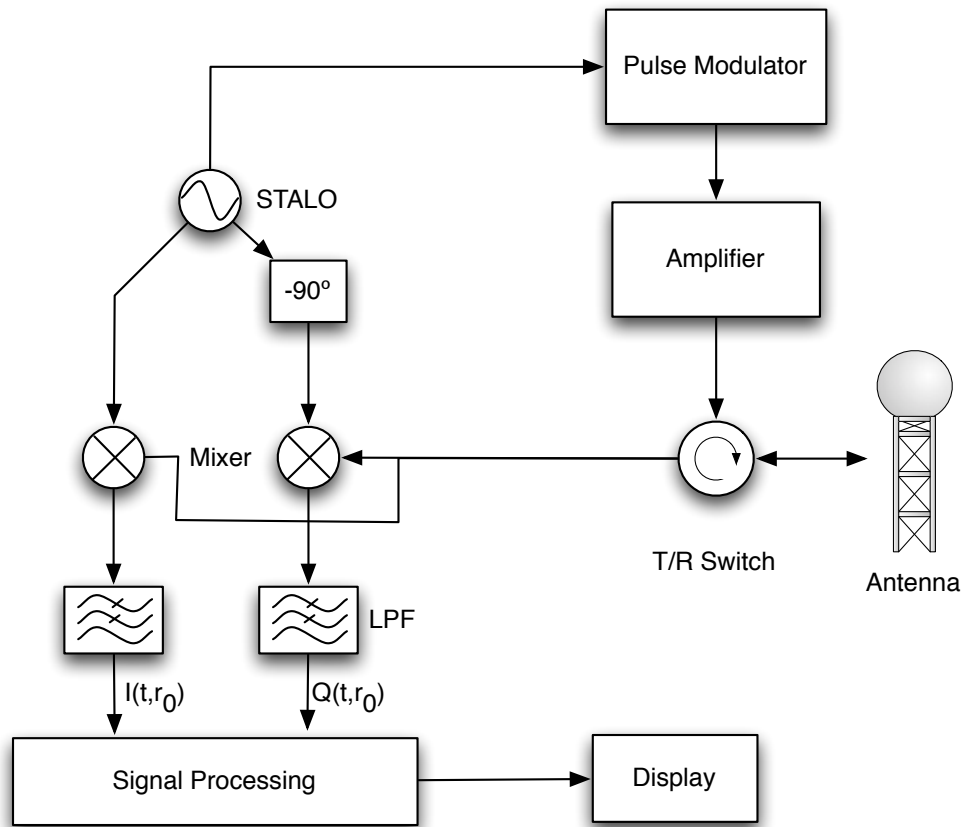


Figure 2.5: Block Diagram of a homodyne Doppler Radar. The RF signal generated by the STALO is modulated, amplified, and transmitted into space by the antenna. The received signal is “mixed” with the same RF from STALO, filtered, processed, and finally, displayed for the user.

An heterodyne Doppler radar (see Figure 2.6) generates the RF signal by combining the STALO with a coherent oscillator (COHO) signal. The modulated and

amplified pulse is transmitted through the antenna. Here, the received signal is mixed with the STALO generating an intermediate frequency (IF) signal. In an analog receiver, this IF signal is mixed with the COHO frequency to generate the  $I(t, r_0)$  and  $Q(t, r_0)$  signals. Today, a digital receiver samples the intermediate frequency (IF) signal of a radar receiver. Matched filtering, baseband conversion and phase referencing for coherent-on-receive operation are realized by digital signal processing hardware and software. Usually the filtering and demodulation is an integrated decimation process. The advantages of using digital receivers include higher dynamic range, perfect coherent quadrature detection, programable low pass filters (LPF), and matching filter to the transmitted pulse.

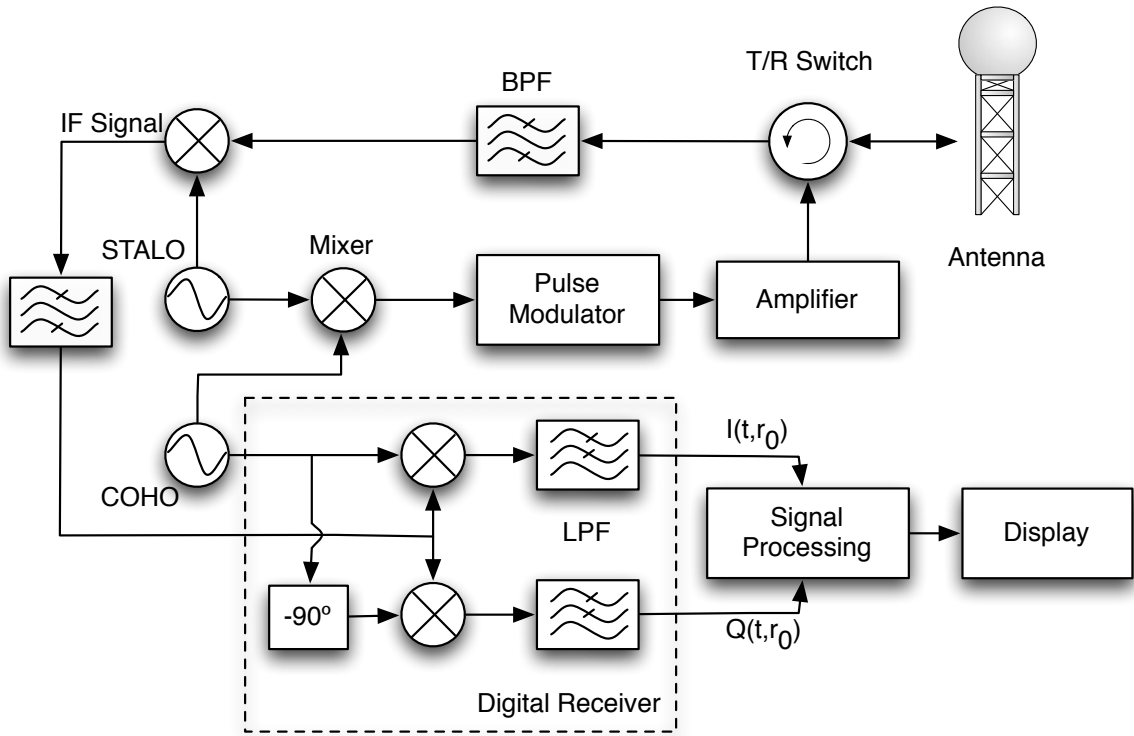


Figure 2.6: Block Diagram of a heterodyne Doppler Radar. A difference from the homodyne system presented in Figure 2.5 is the generation of the RF frequency by combining the STALO and COHO signals. The received signal is mixed with the STALO to obtain an IF signal. This IF signal is sampled by a digital receiver, where matched filtering, baseband conversion and phase referencing for coherent-on-receive operation are realized by digital signal processing hardware and software.

The distance, or the range, to a target is obtained by measuring the time it takes the radar signal to travel from the radar to the target and back. If the target is in motion,  $I(t, r_0)$  and  $Q(t, r_0)$  signals will be used to measure a return signal frequency

shift from the Doppler effect. This frequency shift is proportional to the radial velocity (velocity of the target relative to the radar). The Doppler frequency shift is used to separate the target’s desired movement from fixed “clutter” echoes originating from mountains, sea, buildings, etc. A recent upgrade to digital receivers of the WSR-88D was completed in 2006 as part of the NEXRAD Product Improvement Program Open Systems Radar Data Acquisition (ORDA) project (Crum et al. 1998). One of its main features was the incorporation of the ground clutter suppression algorithm known as Gaussian Model Adaptive Processing (GMAP) (Siggia and Passarelli Jr. 2004). GMAP identifies and removes 20 clutter points. Then, it replaces them with an estimated Doppler spectrum, thereby improving the quality of the post-filtering spectral estimates. Also, the algorithm only applies the filter to spectra that follow the known shape of stationary clutter. The problem with this assumption is that unwanted signals like cars, sea, and/or wind turbines are not removed because they appear as desired targets for the algorithm.

As mentioned previously, the target’s range is calculated by the time,  $T_r$ , it takes the radar signal to travel to the target and back (*range-time*) (see horizontal axis on Figure 2.7). The electromagnetic energy in free space travels at the speed of light, which is  $c \approx 3 \times 10^8 \text{ m s}^{-1}$ , so that the expression for the range  $r$  to the target can be expressed as:

$$r = \frac{cT_r}{2}. \quad (2.17)$$

Typically, multiple transmitted pulses are sent in a sequence at a rate determined by the longest expected target’s range. The time between pulses is also known as “pulse repetition time (PRT)” or “inter-pulse period (IPP)” and is represented by  $T_s$ . The PRT or *sample-time* (see oblique axis on Figure 2.7) also represents the frequency at which the radar signals are sampled. If the PRT is too short, a backscattered signal from a long-range target could arrive after the transmission of the next pulse, and this can be mistakenly associated with the latter pulse rather than the previous, which could lead to an incorrect or ambiguous range estimation (Skolnik 2001). These kinds of echos are called “second-trip echoes”. The maximum range after which targets appear as second-trip echoes is the “maximum unambiguous range”  $r_a$  and can be represented as:

$$r_a = \frac{cT_s}{2} = \frac{c}{2f_s}, \quad (2.18)$$

where  $f_s = 1/T_s$  represents the “pulse repetition frequency” (PRF).

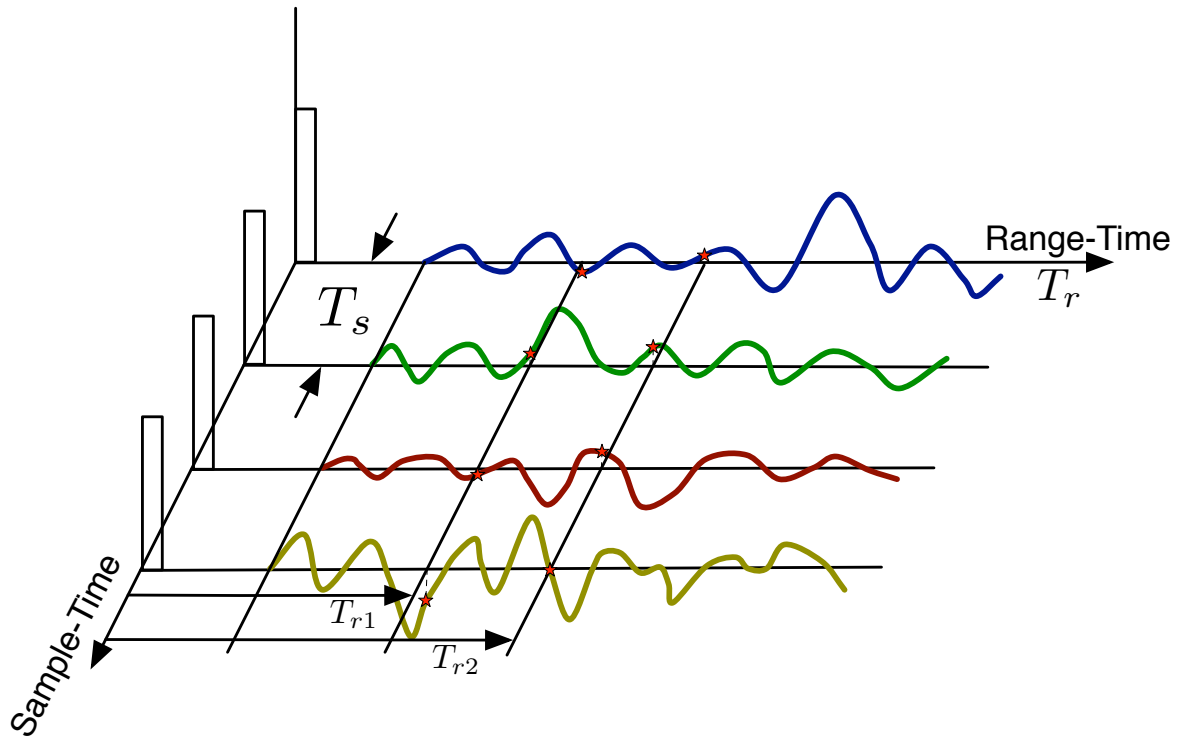


Figure 2.7: Idealized traces for the radar signal (adapted from (Doviak and Zrnić 1993)). Each trace represent a composite of echoes for each transmitted pulse. Instantaneous samples are taken at  $T_{r1}$ ,  $T_{r2}$ , etc. The red stars represent a probable time dependence of the sample at  $T_r$ . Samples at fixed  $T_r$  taken at  $T_s$  intervals are used to construct the Doppler spectrum from targets located at approximately the range  $cT_r/2$ .

The target’s velocity measurements are obtained from the received signal phase. The echo phase is sampled at intervals  $T_s$ , and its change over the interval  $T_s$  is a measure of the Doppler frequency  $f_d = -2v_r/\lambda$ , where  $v_r$  is the radial velocity,  $\lambda = c/f$  is the radar wavelength, and  $f$  is the frequency of the radar. According to the “Nyquist Sampling theorem”, the sampling frequency has to be greater than twice the highest frequency of interest in order to calculate the Doppler frequency without any ambiguities  $f_s > 2f_N$ . By combining both expressions, the “aliasing velocity” can be expressed as:

$$v_a = \pm \frac{\lambda}{4T_s}. \quad (2.19)$$

Unfortunately, both ambiguity conditions (Equations (2.18) and (2.19)) cannot be improved simultaneously. A large  $T_s$  is needed to avoid range ambiguities, and a short  $T_s$  is needed to avoid velocity aliasing. Both requirements must compromise to achieve good range and velocity estimates (“Doppler dilemma”). In practice (especially in weather radars), the volume scan is designed with two distinct PRTs to analyze range and velocity independently, as well as to possibly correct second-trip echos in post-processing. This method is called *batch PRT*, and it uses a sequence of two short PRTs to estimate velocity and another sequence of long PRTs to estimate power.

Other methods to mitigate the range velocity ambiguity include staggered PRT (SPRT) (Sirmans et al. 1976), dual PRF, and phase coding. SPRT alternates between a short and long PRT, with the preferred ratio of 2/3. The maximum unambiguous range is determined by the long PRT, while the maximum unambiguous velocity is obtained by SPRT velocity de-aliasing algorithm (Doviak and Zrnić 1993; Torres et al. 2004). The dual PRF (Dazhang et al. 1984) technique alternates two “batches” of PRTs, which improves the ground clutter filtering. The technique uses the SPRT dealiasing velocity algorithm. However, it fails when there is strong shear present. The systematic phase coding technique uses deterministic codes to reduce the effects of range overlaid echoes (Sachidananda and Zrnić 1986). This code is usually part of the SZ-2 algorithm developed by NSSL and The National Center for Atmospheric Research (NCAR) and has been operational on the NEXRAD network since 2007. The algorithm transmits a long PRT without coding and short PRT with a SZ(8/64) code to recover velocities from overlaid echoes.

## 2.2.2 The Radar Equation

Radars transmit pulses at a high power to maintain the required sensitivity to detect reflections from targets at a desired maximum range. The *radar equation* is used to determine the returned power  $P_r$  based on multiple parameters from a single target with backscattered cross-section  $\sigma_b$  (Skolnik 1990; Doviak and Zrnić 1993).

$$P_r = \frac{P_t G^2 \lambda^2 \sigma_b f^4(\theta, \phi)}{(4\pi)^3 r^4 l^2}, \quad (2.20)$$

where  $P_t$  is the transmitted power, and  $G^2$  represents the gain of the transmitting and receiving antennas for the monostatic case. The range to the target is represented by  $r$ ,  $l$  represents the attenuation losses, and  $f^4(\theta, \phi)$  is the two-way normalized power density pattern. The radar equation is important for characterizing a radar system. There are many forms of the radar equation, and depending on the application, different parameters are considered. For atmospheric scatter, however, it is almost impossible to have a single target within the resolution volume. Consequently, it is necessary to modify the equation to consider volume scattering. Hence, the the radar equation for a volume filled with targets (Doviak and Zrnić 1993; Cohn 1995; Hocking 1985, 1996; White 1997) can be presented as:

$$P_r = \frac{P_t G^2 \lambda^2}{(4\pi)^3 r_0^2 l^2} \times \frac{c\tau_w}{2} \times \frac{\pi\theta_1^2}{8 \ln 2} \times \eta \quad (2.21)$$

where  $r_0$  is the range to the center of the resolution volume. The radar resolution volume refers to the minimum separation between two volume targets that permits them to be distinguished by a radar. The second term on the right-hand-side of the equation represents the range resolution  $\Delta r = c\tau_w/2$ , where  $\tau_w$  is the transmitting pulse width. The third term on the right-hand-side represents the transmitting beamwidth, where  $\theta_1$  is the 3-dB width (in radians) of the one-way pattern (Doviak and Zrnić 1993). Finally, the radar reflectivity  $\eta$ , or average backscatter cross-section per unit volume (White 1997), is a measurement of the radar scattering intensity in units of  $\text{m}^{-1}$ .

## 2.2.3 Scattering Mechanisms

### 2.2.3.1 Weather Radar - Rayleigh Scatter

For weather radars, the radar reflectivity is related to the amount and type of precipitation in the resolution volume. If the diameter  $D$  of a spherical drop is small

compared to  $\lambda$  ( $D \leq \lambda/16$ ), then the process is approximated by Rayleigh scattering (Doviak and Zrnić 1993). Under the Rayleigh approximation, the backscattered cross-section  $\sigma_b$  is proportional to  $D^6$ . The radar reflectivity can be expressed as a function of the drop size distribution  $N(D)$  and  $\sigma_b$ :

$$\eta = \int_0^{\infty} \sigma_b(D)N(D)dD, \quad (2.22)$$

$$\sigma_b \approx \frac{\pi^5}{\lambda^4}|K_m|^2D^6. \quad (2.23)$$

The term  $K_m$  is called the complex dielectric factor and is defined as (Doviak and Zrnić 1993):

$$K_m = \frac{m^2 - 1}{m^2 + 2}, \quad (2.24)$$

where  $m = n - jn\kappa$  is the complex refractive index for water. The refractive index is  $n$ , and  $\kappa$  is the attenuation index. The typical value of  $|K_m|^2$  for liquid water is 0.92 for wavelengths between 0.01 and 0.10 m. Ice spheres have a  $|K_m|^2$  of approximately 0.18, which is independent of temperature and is valid for radar wavelengths in the microwave region (Doviak and Zrnić 1993).

The reflectivity can also be expressed as a function of  $Z$ , the so called “reflectivity factor”. This is a very common term which can be related to the intensity of precipitation.

$$\eta = \frac{\pi^5}{\lambda^4}|K_m|^2Z, \quad (2.25)$$

$$Z = \int_0^{\infty} N(D)D^6dD. \quad (2.26)$$

Whenever the Rayleigh approximation does not apply (usually for short-wavelength ( $\lambda < 10$  cm) weather radars), it is acceptable to express the reflectivity as (Doviak and Zrnić 1993):

$$\eta = \frac{\pi^5}{\lambda^4}|K_m|^2Z_e, \quad (2.27)$$

where  $Z_e$  is the “equivalent reflectivity factor”. The units of  $Z$  are  $\text{mm}^6 \text{m}^{-3}$ , but it is more common to express  $Z$  on a logarithmic scale (dBZ or  $10\log_{10} \frac{Z}{1\text{mm}^6\text{m}^{-3}}$ ). An example of the values of  $Z$  are taken from Doviak and Zrnić (1993) and presented in Table 2.2.

Table 2.2: Examples of the values of  $Z$

$Z$ value	Type of precipitation
0 dBZ	cumulus clouds
20 dBZ	light rain
60 dBZ	heavy rainfall and hail

### 2.2.3.2 Clear-Air Radar - Bragg Scatter

The energy spectrum of turbulence  $E(\kappa)$  proposed by Kolmogorov can be classified into three regions (see Figure 2.8): the energy-containing range, the inertial subrange, and the dissipation range (Pope 2000). Under this hypothesis (White 1997), there is no exchange of energy between the energy-containing range and the dissipation range. However, the rate of energy transfer from large scales in the energy-containing range is equivalent to the energy dissipation rate at small scales in the dissipation range. In the inertial subrange, the bulk of energy transfers from larger to smaller scales following a slope of  $-5/3$ , and it can be observed in Figure 2.8. This is also known as “energy cascade” assumption or “Kolmogorov  $-5/3$  turbulence spectrum” for isotropic turbulence, where the turbulence has the same variance in all directions (Stull 2000). Under these conditions the energy spectrum of turbulence per unit mass  $E(\kappa)$  can be expressed as:

$$E(\kappa) = A_e \epsilon^{2/3} \kappa^{-5/3}, \quad (2.28)$$

where  $A_e$  is a universal dimensionless constant between 1.53 and 1.68 (Gossard and Strauch 1983),  $\epsilon$  is the turbulence kinetic energy (eddy) dissipation rate, and  $\kappa$  represents the wavenumber. In the ABL inertial subrange, the large eddies usually have sizes of 200 m and the small eddies sizes of 1 cm (Wallace and Hobbs 2006).

The radar reflectivity for clear-air radars is a measurement of the intensity caused by refractive index fluctuations present in the radar resolution volume. If the radar half-wavelength (Bragg scale) lies within the inertial subrange, the radar reflectivity can be represented as:

$$\eta = 0.379 C_n^2 \lambda^{-1/3}, \quad (2.29)$$

where  $C_n^2$  is the structure function parameter of refractive index ( $\text{m}^{-2/3}$ ) (Tatarskii 1961; Ottersten 1969; Cohn 1995; Doviak and Zrnić 1993; White 1997).

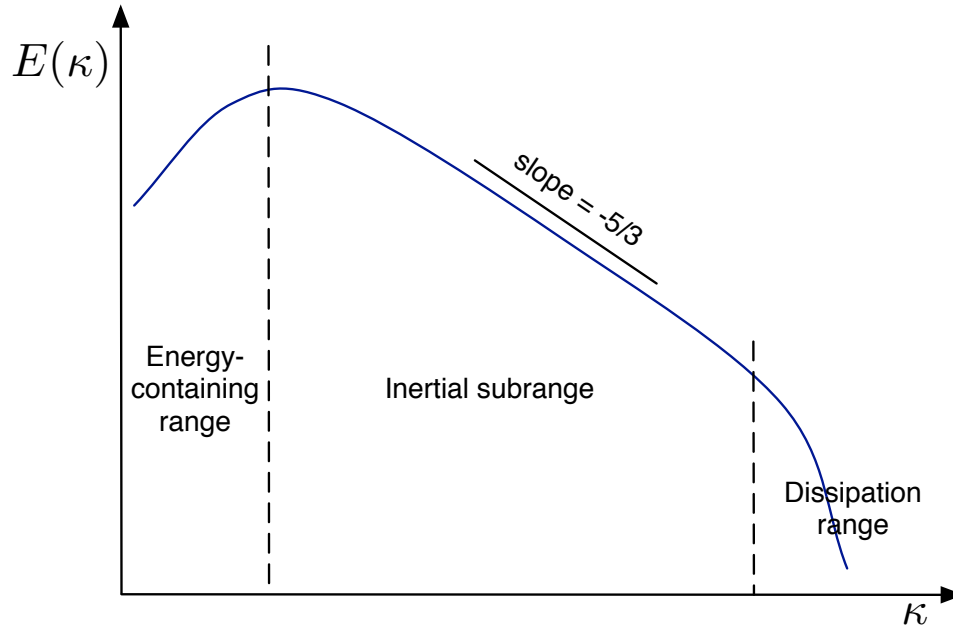


Figure 2.8: Simple diagram of the Kolmogorov turbulence spectrum (adapted from Pope (2000)). The energy spectrum of turbulence  $E(\kappa)$  and wavenumber  $\kappa$  axes are in logarithmic scale. In the inertial subrange, the large eddies from the energy-containing range cascades into the small eddies in the dissipation range following a slope of  $-5/3$ .

Typical values of  $C_n^2$  are extracted from Doviak and Zrnić (1993) and presented in Table 2.3. These values give an idea of the turbulence magnitude typically observed in the atmosphere.

Table 2.3: Examples of the magnitude and intensity of  $C_n^2$

$C_n^2$ value	Intensity of turbulence
$6 \times 10^{-17} \text{ m s}^{-2/3}$	weak
$2 \times 10^{-15} \text{ m s}^{-2/3}$	intermediate
$3 \times 10^{-13} \text{ m s}^{-2/3}$	strong

## 2.3 Signal Processing for Radars that Observe the Atmosphere

The received signal after the matched filter in Figure 2.5 has an in-phase and quadrature component, and can be represented as:

$$I(t, r_0) = \frac{|A|}{2} \cos \psi_e U(t - 2r_0/c), \quad (2.30)$$

$$Q(t, r_0) = -\frac{|A|}{2} \sin \psi_e U(t - 2r_0/c), \quad (2.31)$$

where  $A$  is the complex amplitude, and  $U(t)$  is the transmitted pulse shape defined as:

$$U(t) = \begin{cases} 1 & 0 \leq t \leq \tau_w \\ 0 & \text{elsewhere} \end{cases}. \quad (2.32)$$

The echo phase of the signal  $\psi_e$  is represented as (Doviak and Zrnić 1993):

$$\psi_e = \frac{4\pi r_0}{\lambda} + \frac{4\pi v_r t}{\lambda} - \psi_t - \psi_s, \quad (2.33)$$

where  $v_r$  is the average radial velocity within the resolution volume,  $\psi_t$  and  $\psi_s$  represent the transmitted phase and the scattering phase shift, respectively. Normally, the received complex echo voltage is the combination of the in-phase and quadrature components as:

$$V(t, r_0) = I(t, r_0) + jQ(t, r_0), \quad (2.34)$$

$$V(t, r_0) = \frac{|A|}{2} \exp(-j\psi_e) U(t - 2r_0/c). \quad (2.35)$$

The components of the complex echo voltage ( $I$ ,  $Q$ ) are considered random variables because the motion of the scatters within the resolution volume is unpredictable (Doviak and Zrnić 1993). Also, within this volume, the scatters are large in number, and none are dominant. This condition implies, through the *Central Limit Theorem*, that  $I$  and  $Q$  have a Gaussian distribution. Moreover, the atmosphere is constantly changing, and the time over which the complex echo voltage is taken is small compared to the time it takes for significant changes to occur. Under these conditions, the complex echo voltage  $V$  is a *wide-sense stationary* (WSS) random process. Finally, the received signals are considered to be *ergodic*, which means that temporal averaging will converge to ensemble averages and be used to investigate the statistical parameters of the process.

The time-series data obtained from the radar can reveal a wealth of information of the characteristics within the resolution volume. The most practical approach is to analyze the *Doppler spectrum*, which is the power-weighted distribution of radial velocities within the resolution volume. The Doppler spectrum is obtained from the Fourier transform of the autocorrelation function (ACF):

$$S(f) = \mathcal{F}\{R(\tau)\}, \quad (2.36)$$

where  $R(\tau)$  is the ACF assuming a WSS random process

$$R(\tau) = E[V^*(t)V(t + \tau)], \quad (2.37)$$

where  $*$  represents complex conjugate, and  $E[\cdot]$  represents the expected value.

Since the complex echo voltage is sampled through the pulsed radar design, the Doppler spectrum or power spectral density (PSD) must be obtained through the calculation of the discrete time Fourier transform (DTFT):

$$\hat{S}(f) = T_s \sum_{m=-(M-1)}^{M-1} \hat{R}(k)e^{-j2\pi f T_s k}, \quad (2.38)$$

where  $k$  represents the lag, and  $M$  represents the total number of samples. The  $\hat{\cdot}$  represents an estimated value. For a discrete WSS signal, the biased estimator of ACF is given by:

$$\hat{R}(k) = \frac{1}{M} \sum_{m=0}^{M-|k|-1} V^*(m)V(m+k). \quad (2.39)$$

In this equation, the term  $T_s$  is omitted in the finite complex echo voltage  $V(mT_s)$ .

The bias of a signal estimator  $\alpha$  refers to the difference between the expected value of the estimator and the true value  $\text{Bias}(\hat{\alpha}) = E[\hat{\alpha}] - \alpha$ . The mean-square-error (MSE) can be expressed in terms of the variance and the bias  $E[(\hat{\alpha} - \alpha)^2] = \text{Var}(\hat{\alpha}) + \text{Bias}^2(\hat{\alpha})$ .

Another estimator of the Doppler spectrum can be obtained through the *periodogram* as:

$$\hat{S}(f) = \frac{T_s}{M} |Z(f)|^2, \quad (2.40)$$

where  $Z(f)$  is the DTFT of  $V(mT_s)$  (Doviak and Zrnić 1993; Shanmugan and Breipohl 1988) calculated as:

$$Z(f) = \sum_{m=0}^{M-1} V(m)e^{-j2\pi f m T_s}. \quad (2.41)$$

Since  $\widehat{S}(f)$  is estimated based on a finite number of pulses, there is a bias resulting from the multiplication of the complex echo voltage signal and the rectangular window of length  $M$  (data window), which is required for truncated data. The Doppler spectrum estimate is the convolution between the true spectrum with the Fourier transform of the corresponding lag window and results in a broadening of the true spectrum and transfer of power from the peak into the sidelobes (Doviak and Zrnić 1993). The lag window is obtained through the calculation of ACF of the data window.

### 2.3.1 Spectral Moments

The Doppler spectrum is often assumed to have a Gaussian shape and is represented as:

$$S(v) = \frac{S}{\sqrt{2\pi}\sigma_v} \exp\left[-\frac{(v - v_r)^2}{2\sigma_v^2}\right] + \frac{2NT_s}{\lambda}, \quad (2.42)$$

where  $S$  represents the signal power,  $N$  is the noise power which is assumed to be white, and  $v_r = -\lambda f_d/2$  is the mean radial velocity within the resolution volume. A schematic of the Doppler spectrum is depicted in Figure 2.9. Also, for direct calculations of the radial velocity, the Doppler spectrum presented in Equation (2.42) is now represented in terms of velocity instead of frequency (see Equation (2.38)).

The most important characteristics of the signals obtained from the Doppler spectrum are described below (Doviak and Zrnić 1993).

1. Total power or the *zeroth moment* of the Doppler spectrum: Depending on the type of radar, this can be indicative of the turbulence level (clear-air radars), or the liquid water content or precipitation (weather radars).
2. Mean Doppler velocity or the *first moment* of the power-normalized spectra: This is indicative of the scatterers' radial velocity.
3. Spectrum width  $\sigma_v$ , the square root of the *second moment* about the first of the normalized spectrum: This a measure of shear or turbulence within the resolution volume.

The ACF (see Figure 2.10) is calculated from the inverse Fourier transform of  $S(v)$  and is presented below:

$$R(mT_s) = S \exp\left[-8\left(\frac{\pi\sigma_v mT_s}{\lambda}\right)^2\right] e^{-j4\pi v_r mT_s/\lambda} + N\delta_m, \quad (2.43)$$

where  $\delta_m$  is the Kroneker delta function.

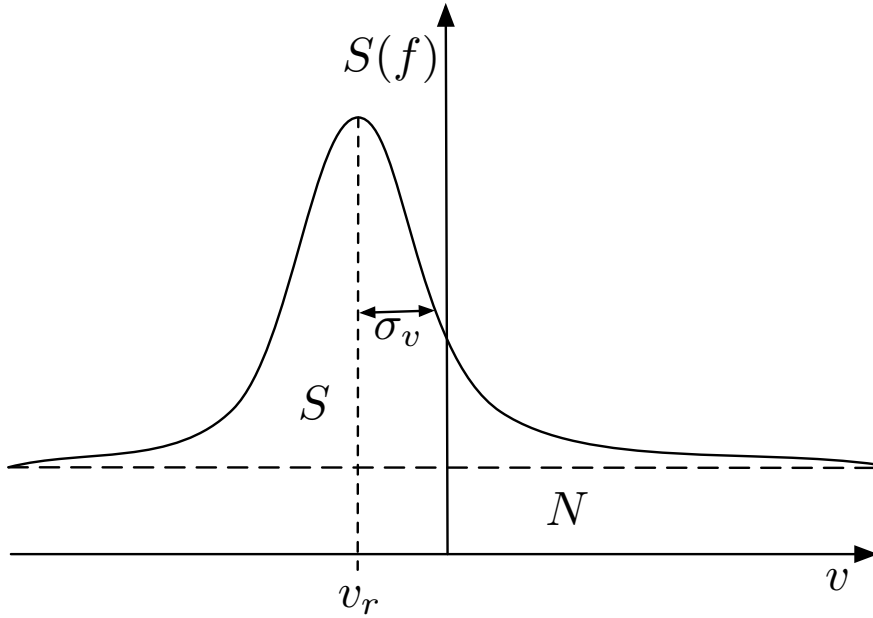


Figure 2.9: Schematic of the Doppler spectrum.  $S$  represents the signal power,  $N$  is the noise power (usually assumed “white”),  $v_r$  is the mean radial velocity, and  $\sigma_v$  represents the Doppler spectral width.

### 2.3.1.1 Moment Estimation in the Time Domain

The total power  $P$ , or the zeroth moment, is estimated from the ACF at lag zero ( $m = 0$ ). In comparison to Equation (2.43), it can be observed that the estimated power is the sum of the estimated power signal  $S$  and estimated noise power  $N$ :

$$\hat{P} = \hat{S} + \hat{N}, \quad (2.44)$$

$$\hat{P} = \hat{R}(0) = \frac{1}{M} \sum_{m=0}^{M-1} V^*(m)V(m), \quad (2.45)$$

$$\hat{S} = \hat{R}(0) - \hat{N}. \quad (2.46)$$

The noise power appears at the center of the ACF (see Figure 2.10). The signal power is estimated by removing the center point and replacing it by an interpolated value using the closest four points around the center. The noise power is then obtained by subtracting the initial ACF at lag zero minus the estimated signal power.

An improvement in the accuracy of the power estimation is obtained when the dwell time is long (i.e., number of samples  $M$  large). However, this improvement in accuracy sacrifices the data update time (Doviak and Zrnić 1993).

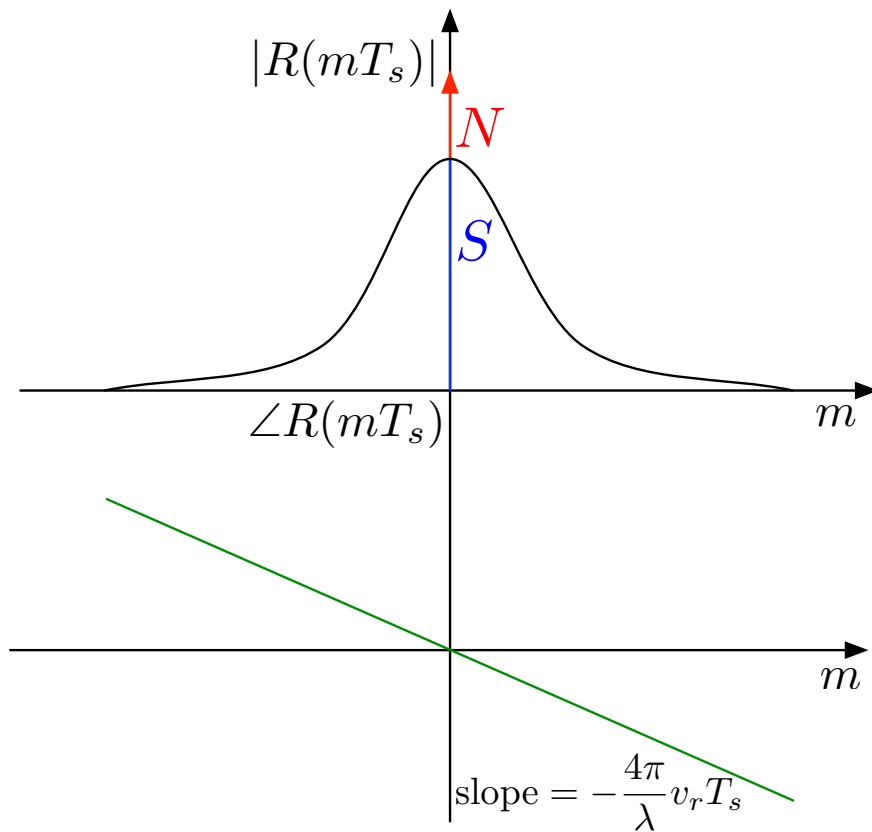


Figure 2.10: Schematic of the autocorrelation function. Top: magnitude of the ACF. Signal power is represented by  $S$ ,  $N$  is the noise power. Bottom: phase of the ACF. The radial velocity  $v_r$  is calculated based on the phase of the ACF at lag 1 ( $\tau = 1$ ).

An estimate of the mean radial velocity can be obtained from the autocorrelation function at lag one ( $m = 1$ ) in Equation (2.43):

$$\hat{v}_r = \frac{-\lambda}{4\pi T_s} \angle(\hat{R}(T_s)), \quad (2.47)$$

where  $\angle$  represents the phase of the ACF.

Finally, for the Doppler spectral width estimates, two lags are necessary. The direct way is to use lag zero and lag one; however, the magnitude of the ACF at lag zero is contaminated with noise power. Here, the estimate of  $\sigma_v$  will be obtained from lag one ( $\hat{R}(T_s)$ ) and lag two ( $\hat{R}(2T_s)$ ) as:

$$\hat{\sigma}_v = \frac{\lambda}{2\sqrt{6}\pi T_s} \left[ \ln \left( \frac{\hat{R}(T_s)}{\hat{R}(2T_s)} \right) \right]^{1/2}. \quad (2.48)$$

Note that this procedure could lead to undetermined values of Doppler spectral width due to calculations of fractional values of  $\ln(\cdot)$ , and these values need to be discarded as  $\sigma_v$  should always be positive.

Computationally, estimates of the moments are more efficient in the time domain (Doviak and Zrnić 1993). Nevertheless, estimates in the frequency domain can help to remove unwanted signals (i.e., interference) or to study other signal characteristics (i.e., non-Gaussian shape (Yu et al. 2009)). Finally, Lei et al. (2011) introduced a new technique that uses multi-lag correlation estimators to obtain polarimetric radar measurements in the presence of low signal-to-noise ratio (SNR).

### 2.3.1.2 Moment Estimation in the Frequency Domain

An estimate of the total power in the frequency domain is obtained by summing the contributions of all velocities of the periodogram as:

$$\hat{P} = \frac{\lambda}{2MT_s} \sum_{k=0}^{M-1} \hat{S}(k). \quad (2.49)$$

The signal power  $\hat{S}$  is obtained after subtracting the white noise contribution  $\hat{N}$  using a noise level estimation scheme such as that proposed by Hildebrand and Sekhon (1974).

The estimate of the mean radial velocity  $\widehat{v}_r$  and Doppler spectrum width  $\widehat{\sigma}_v$  are obtained from Doviak and Zrnić (1993):

$$\widehat{v}_r = \frac{-\lambda}{2MT_s} \left[ \sum_{k=k_m-M/2}^{k_m+M/2+1} k \widehat{S}_n(\text{mod}_M(k)) - \frac{M}{2} \right], \quad (2.50)$$

$$\widehat{\sigma}_v^2 = \left( \frac{\lambda}{2MT_s} \right)^2 \sum_{k=k_m-M/2}^{k_m+M/2-1} (k - k_m)^2 \widehat{S}_n(\text{mod}_M(k)), \quad (2.51)$$

where  $k_m$  is a rough estimate of the peak of the spectra, and  $\text{mod}(\cdot)$  represents the “modulo” operator. These calculations mitigate biases due to aliasing if spectra are symmetric (Doviak and Zrnić 1993). An expression for the normalized spectrum  $\widehat{S}_n(k)$  is obtained from:

$$\widehat{S}_n(k) = \frac{\widehat{S}(k)}{\sum_{k=0}^{M-1} \widehat{S}(k)}. \quad (2.52)$$

The measured spectrum width  $\sigma_v^2$  is the contribution of many independent broadening factors such as: shear  $\sigma_s^2$ , turbulence  $\sigma_{11}^2$ , and signal processing  $\sigma_x^2$  (Doviak and Zrnić 1984; Doviak and Zrnić 1993). The spectrum width can be represented as  $\sigma_v^2 = \sigma_s^2 + \sigma_{11}^2 + \sigma_x^2$ . Consequently, the Doppler spectrum due to turbulence is contaminated by all the other contributions. These contributions can be eliminated depending on their cause. For example, the shear contribution can be represented as a function of the horizontal wind (Doviak and Zrnić 1993), and the signal processing contribution is related to  $M$  number of points. Both effects can be removed successfully. However, if the turbulence is very weak, there might be cases where the resultant spectrum could be negative and should be discarded (Hocking 1988).

## 2.4 Techniques for the Estimation of the Three-Dimensional Wind Field

### 2.4.1 Doppler Beam Swinging

Doppler Beam Swinging (DBS) is a technique used to estimate the three components of the wind field in clear-air. This technique is based on measurements of mean radial velocity using three or more non-coplanar beams. The radar usually points vertically, or nearly vertically. DBS is based on the assumption of homogeneity and stationarity during the time of the scan. A summary of the technique can be found in the work of Gage and Balsley (1978), Balsley (1981), and Balsley and Gage (1982).

Radial velocity can be expressed as a function of the three wind field components: the zonal wind  $u_o$  positive to the East, the meridional wind  $v_o$  positive to the North, the vertical wind  $w_o$  positive away from the radar (upward). The radial velocity, presented in the left panel of Figure 2.11, can be expressed as a function of the horizontal velocity  $v_H$  and  $w_o$ , and  $v_H$ , presented in the right panel of Figure 2.11, as a function of  $u_o$ ,  $v_o$ , the azimuth angle  $\theta$ , and zenith angle  $\phi$  as:

$$v_r = v_H \sin \phi + w_o \cos \phi, \quad (2.53)$$

$$v_H = u_o \sin \theta + v_o \cos \theta, \quad (2.54)$$

$$v_r(\theta, \phi) = u_o \sin \theta \sin \phi + v_o \cos \theta \sin \phi + w_o \cos \phi. \quad (2.55)$$

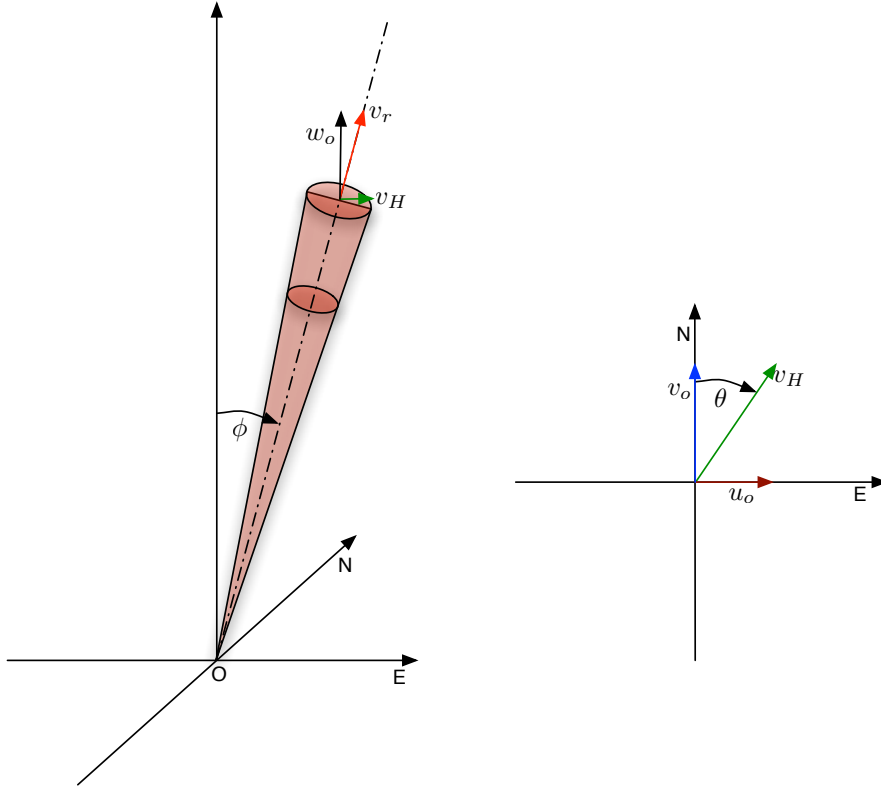


Figure 2.11: Schematic of the calculations of radial velocity  $v_r$  as a function of the three wind fields components. Left: the radial velocity is expressed as a function of the horizontal velocity and the vertical wind field. Right: the horizontal velocity is expressed as a function of the zonal and meridional wind fields.

When combining the radial velocities from at least three beams of similar height (see Figure 2.11), it is more convenient to express Equation (2.55) in matrix form,

$$\mathbf{v}_r = \mathbf{A}\mathbf{u}, \quad (2.56)$$

where :

$$\mathbf{A} = \begin{bmatrix} \sin \theta_1 \sin \phi_1 & \cos \theta_1 \sin \phi_1 & \cos \phi_1 \\ \vdots & \vdots & \vdots \\ \sin \theta_n \sin \phi_n & \cos \theta_n \sin \phi_n & \cos \phi_n \end{bmatrix}, \quad (2.57)$$

$$\mathbf{u} = \begin{bmatrix} u_o & v_o & w_o \end{bmatrix}^T, \quad (2.58)$$

$$\mathbf{v}_r = \begin{bmatrix} v_{r1} & \cdots & v_{rn} \end{bmatrix}^T. \quad (2.59)$$

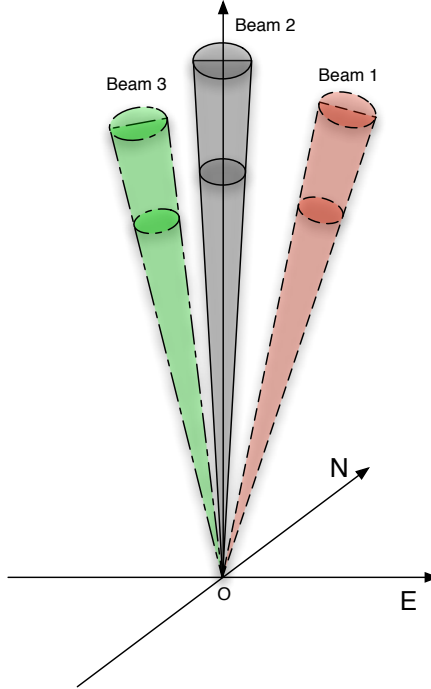


Figure 2.12: Schematic of the Doppler Beam Swinging Technique. DBS uses at least three non-coplanar beams to estimate the three components of the wind field under the assumptions of homogeneity and stationarity during the time of the scan.

The minimum number of independent radial velocities needed to estimate the three-dimensional velocity vector  $\mathbf{u}$  is three ( $n = 3$ ). If  $n < 3$ , the system becomes undetermined. If  $n > 3$ , the solution to the set of equations can be estimated in the least-squares sense using:

$$\mathbf{u} = (\mathbf{A}\mathbf{A}^T)^{-1} \mathbf{A}^T \mathbf{v}_r. \quad (2.60)$$

## 2.4.2 Spaced Antenna

Another technique used to estimate the three-dimensional wind is called the Spaced Antenna (SA) method, which technique uses one transmitter and three or more closely

spaced receivers. By calculating the cross-correlation function (CCF) between the received radar signals, it is possible to estimate the horizontal wind and wind variability (turbulence). The SA technique was first presented by Briggs et al. (1950), and its implementation using the Full Correlation Analysis (FCA) was described in Briggs (1984).

The generalized theoretical expression for the CCF used by SA to measure horizontal wind is presented in Doviak et al. (1996) and Holloway et al. (1997). The equation is presented below:

$$c_{12}(\tau) = \exp \left[ -2jk_o w_o \tau - 2(k_o \sigma_t \tau)^2 - \beta_h^2 \left( u_o \tau - \frac{\Delta x}{2} \right)^2 - \beta_h^2 \left( v_o \tau - \frac{\Delta y}{2} \right)^2 - \frac{1}{8} \left( \frac{w_o \tau}{\sigma_r} \right)^2 \right], \quad (2.61)$$

where  $\tau$  represents the time lag,  $k_o = 2\pi/\lambda$  is the radar wavenumber, and  $\Delta x$  and  $\Delta y$  represent the separation of the two receivers along the  $x$  and  $y$  direction, respectively. The root-mean-square error (rms) wind variability of each wind component for isotropic turbulence is represented by  $\sigma_t$ ,  $\sigma_r$  is the second central moment of the range weighting function, which is assumed to be equal for both receivers,  $\beta_h$  is related to the scale length of the diffraction pattern (see Equations (3), (4), (5), and (6) of Holloway et al. (1997)). The effect of the vertical wind  $w_o$  is typically small and will be omitted in the future (Holloway et al. 1997; Zhang and Doviak 2007).

By taking the magnitude of Equation (2.61) and rewriting in a more convenient form, the normalized ACF ( $\Delta x, \Delta y=0$ ) and CCF ( $\Delta y=0$ ) are obtained:

$$|c_{11}(\tau)| = \exp \left[ -\beta_h^2 (u_o^2 + v_o^2) - 2k_o^2 \sigma_t^2 \tau^2 \right] + \frac{N}{S} \delta(\tau), \quad (2.62)$$

$$|c_{12}(\tau)| = \exp \left[ -\beta_h^2 \left( u_o \tau - \frac{\Delta x}{2} \right)^2 - \beta_h^2 v_o^2 \tau^2 - 2k_o^2 \sigma_t^2 \tau^2 \right]. \quad (2.63)$$

A new notation for ACF  $c_{11}(\tau)$  is included here to be consistent with CCF. However both  $c_{11}(\tau)$  and  $R(\tau)$  are equivalent to denote the ACF. Typically, the ACF and CCF are assumed to be Gaussian functions. The wind estimates using FCA are obtained based on their Gaussian fitted parameters using:

$$|\hat{c}_{12}(\tau)| = \exp \left[ -\hat{\eta} - \frac{(\tau - \hat{\tau}_p)^2}{2\hat{\tau}_c^2} \right] + \hat{c}_0, \quad (2.64)$$

where  $\hat{\eta}$  is the decorrelation parameter,  $\hat{\tau}_p$  is the peak time delay of  $|\hat{c}_{12}(\tau)|$ ,  $\hat{\tau}_c$  is the square root of the second central moment of  $|\hat{c}_{12}(\tau)|$ , and  $\hat{c}_0$  accounts for the observed

amplitude offset of ACF and CCF (Holloway et al. 1997). This offset is caused by a DC component present in the received voltage signals. A schematic of the ACF and CCF is presented in Figure 2.13.

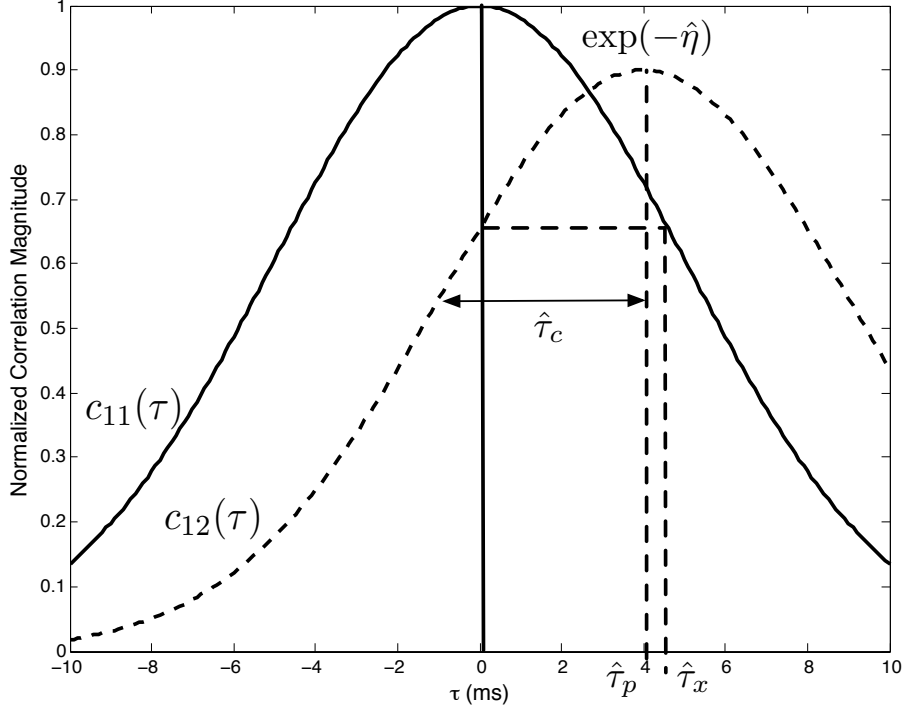


Figure 2.13: Normalized autocorrelation ( $c_{11}(\tau)$ ) and cross-correlation ( $c_{12}(\tau)$ ) functions.  $\hat{\eta}$  represents the decorrelation parameter,  $\hat{\tau}_p$  is the peak time of CCF,  $\hat{\tau}_c$  is the square root of the second central moment of CCF, and  $\tau_x$  is the lag such that  $|c_{11}(\tau_x)| = |c_{12}(0)|$ .

The process of calculating the winds from the Briggs' FCA algorithm can be complicated, but for horizontal isotropic scatters, the baseline wind in the zonal direction can be written as (Briggs 1984; Holloway et al. 1997; Zhang et al. 2003; Doviak et al. 2004):

$$\hat{u} = \frac{\Delta x \hat{\tau}_p}{2\hat{\tau}_x^2}, \quad (2.65)$$

where  $\hat{\tau}_x$  is the lag such that  $|c_{11}(\tau_x)| = |c_{12}(0)|$ . If both the ACF and CCF have Gaussian shape, the technique method is called FCA-Gaussian (FCA-G), and the expression for the baseline wind can be expressed in terms of the Gaussian parameters as (Holloway et al. 1997; Zhang et al. 2003; Doviak et al. 2004):

$$\hat{\tau}_x^2 = 2\hat{\eta}\hat{\tau}_c^2 + \hat{\tau}_p^2, \quad (2.66)$$

$$\hat{u} = \frac{\Delta x \hat{\tau}_p}{2(2\hat{\eta}\hat{\tau}_c^2 + \hat{\tau}_p^2)}. \quad (2.67)$$

In this chapter, the basics of the LES have been presented along with fundamental radar theory. The LES is used in the simulation of a realistic CBL case. This case will be studied with the synthesis of a virtual BLR based on LES. Through radar theory, estimates of power, radial velocity, and spectral width obtained from the virtual BLR will be used to compare and contrast parameters from the CBL. Finally, calculations of the ACF and CCF will be used to estimate the three-dimensional winds using SA, compared with those obtained from the radial velocities through DBS, and contrasted with the “true” winds from LES.

## Chapter 3

# Radar Simulator Design Based on Large-Eddy Simulations

### 3.1 Time Series Radar Simulator

The radar equation (Equation (2.21)) reveals that the backscattered signal power from a distributed target is directly proportional to the radar reflectivity  $\eta$ . The value of  $\eta$  represents the average backscattering cross-section per unit volume. Clear-air scatter will develop from turbulent variations in the refractive index  $n$ . The radar reflectivity  $\eta$  is given as a function of the structure function parameter of refractive index  $C_n^2$  and radar wavelength  $\lambda$  (see Equation (2.29)).

In addition to the assumptions that the turbulence is both isotropic and in the inertial subrange, it is further assumed that the radar resolution volume is uniformly filled with turbulence. In this case, the structure function parameter of refractive index  $C_n^2$  is derived from the refractive index field using (Tatarskii 1971):

$$D_n(\boldsymbol{\delta}) = \langle [n(\mathbf{r} + \boldsymbol{\delta}) - n(\mathbf{r})]^2 \rangle_r, \quad (3.1)$$

$$D_n(\delta) = C_n^2 \delta^{2/3}, \quad (3.2)$$

$$C_n^2 = \frac{\langle [n(\mathbf{r} + \boldsymbol{\delta}) - n(\mathbf{r})]^2 \rangle_r}{|\boldsymbol{\delta}|^{2/3}}, \quad (3.3)$$

where  $D_n$  is the structure function for locally homogeneous perturbations, and  $\langle \cdot \rangle_r$  denotes the spatial average over a volume within which the  $n$  irregularities are assumed to be statistically isotropic and homogeneous. Here,  $\mathbf{r}$  represents the position vector,  $\boldsymbol{\delta}$  denotes the spatial separation, and  $\delta = |\boldsymbol{\delta}|$ . The refractive index is related to the refractivity  $N$  through  $n = 1 + N \times 10^{-6}$ . If the background atmospheric pressure profile is in hydrostatic balance, then the refractivity is found directly from

the simulation output parameters through the following equations (Bean and Dutton 1966; Holton 2004):

$$N = \frac{77.6}{T} \left( P + 4811 \frac{e}{T} \right), \quad (3.4)$$

$$d \ln P = -\frac{g}{RT} dz, \quad (3.5)$$

$$T = \Theta \left( \frac{P}{P_0} \right)^{0.286}, \quad (3.6)$$

$$e = \frac{qP}{0.622 + q}, \quad (3.7)$$

where  $P$  is total atmospheric pressure (hPa),  $e(q, T)$  is the partial pressure of water vapor (hPa),  $P_0$  represents the pressure at  $z = 0$  m (1000 hPa),  $g$  is the gravitational acceleration ( $9.81 \text{ m s}^{-1}$ ),  $R$  is the gas constant for dry air ( $287 \text{ J kg}^{-1} \text{ K}^{-1}$ ), and  $T$  is the absolute temperature (K). The electron density term has been omitted in Equation (3.4) due to its influence only in the ionosphere.

Various approaches are available in the literature that have been used to generate time-series data for radar simulations. One approach that was studied by Sheppard and Larsen (1992); Holdsworth and Reid (1995); Yu (2000); and Cheong et al. (2004a) uses the Lagrangian framework approach. This approach consists of creating a *sampling domain* populated with scattering points. These points move within the domain according to the instantaneous wind vector field.

Another method follows the Eulerian framework approach which considers the grid cells of the model as a scattering center. The phase of the radar signal from the scattering center is modulated by the local instantaneous velocity field (Muschinski et al. 1999; Scipi3n et al. 2008). Therefore, by varying the phase without actually moving the scatterer, the expected Doppler velocity can be generated. Some implementation advantages exist with this method such as simple calculations of oblique  $C_n^2$  and fast updates of velocity at each grid point.

The LES sub-domain description and output variables used in the radar simulator are presented in Table 3.1. To calculate  $C_n^2$  within each LES domain grid cell, Equation (3.3) is applied along a line (beam) which connects the position of the virtual radar to the center of the grid cell where  $C_n^2$  is estimated (see left panel of Figure 3.1). However, the radar is sensitive to the Bragg scale ( $\delta = \lambda/2$ ) to which the scale  $\delta$  corresponds. This Bragg scale ( $\sim 16$  cm for a frequency of 915 MHz) is much smaller

Table 3.1: Description of the LES settings

Parameter	Setting
Domain size	$1.4 \times 1.4 \times 2.0 \text{ km}^3$
Number of grid points	$70 \times 70 \times 100$
Spatial resolution	20 m
Time step	1 s
Output variables	$u, v, w, E, q, \Theta$

than the LES grid cell size ( $\Delta \sim 20 \text{ m}$ ). Nevertheless, due isotropy assumed within the LES fields, Equation (3.3) can be expressed as:

$$C_n^2 = \frac{(\Delta n')^2}{\delta^{2/3}} = \frac{(\Delta n)^2}{\Delta^{2/3}}, \quad (3.8)$$

where  $\Delta n'$  represents the refractive index  $n$  gradient at the Bragg scale (which is considered isotropic on the radar scale),  $\Delta n$  represents the refractive index gradient at the grid scale, and  $\Delta$  represents the oblique distance between the layers where the  $\Delta n$  is estimated.

To estimate  $\Delta n$ , the refractive index  $n$  is calculated in the center of the grid cell at level  $z$  with respect to the ground and at two levels displaced from  $z$  in height by an increment  $\Delta z$  (see right panel of Figure 3.1). That is, the points at  $z$ ,  $z - \Delta z$ , and  $z + \Delta z$  are considered. A bilinear interpolation is then applied in order to obtain an estimate of  $n$  between the closest four points on the upper and lower planes, thereby calculating values of  $n$  along the beam:

$$\begin{aligned} n_{xy} &= (1 - dx)(1 - dy)n_{x_0y_0} + (dx)(1 - dy)n_{x_1y_0} + \\ &\quad (1 - dx)(dy)n_{x_0y_1} + (dx)(dy)n_{x_1y_1}, \\ dx &= \frac{x - x_0}{x_1 - x_0}, \quad dy = \frac{y - y_0}{y_1 - y_0}, \end{aligned} \quad (3.9)$$

where  $n_{xy}$  represents the refractive index  $n$  at point  $(x, y)$  (which does not match any of the grid points), and  $n_{x_iy_j}$  denotes refractive index values at  $x_i, y_j$ ;  $i, j = 0, 1$ .

This modification along with the average over two consecutive layers constitute a significant refinement from the work of Muschinski et al. (1999) and yields:

$$C_n^2(x, y, z, t) = \frac{1}{2} \left[ \frac{(n_1 - n)^2}{\Delta^{2/3}} + \frac{(n - n_2)^2}{\Delta^{2/3}} \right], \quad (3.10)$$

where  $n_1$ ,  $n$ , and  $n_2$  represent the refractive index at levels  $z + \Delta z$ ,  $z$ , and  $z - \Delta z$ , respectively, as depicted in right panel of Figure 3.1.

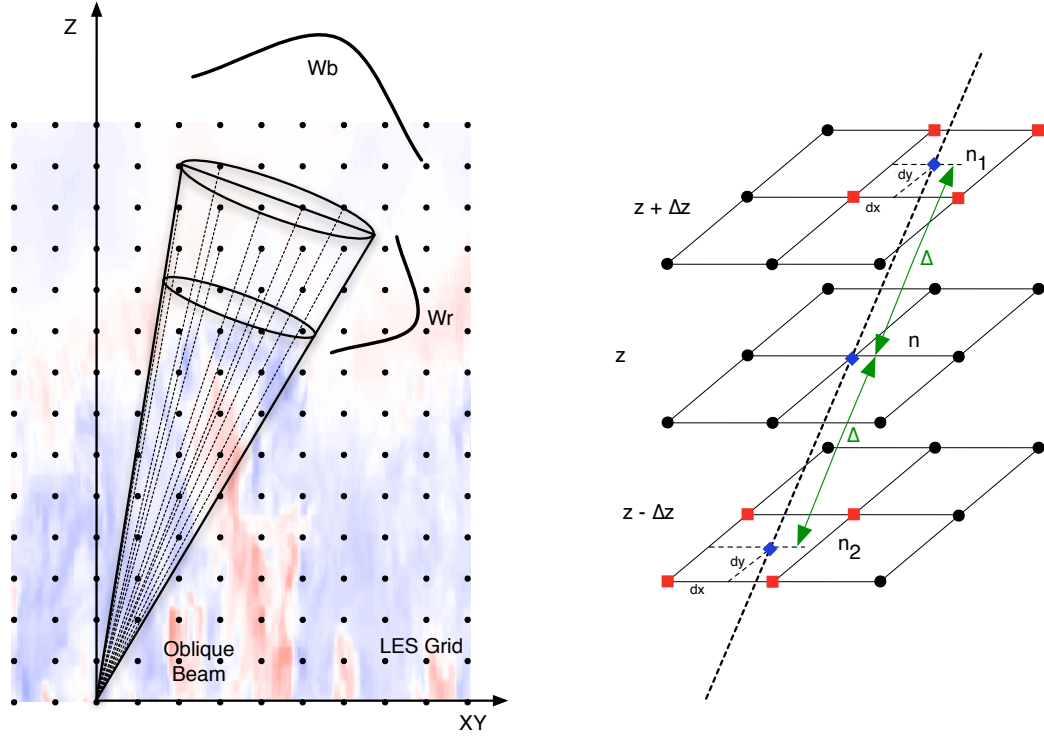


Figure 3.1: Left: scheme that represents an off-vertical pointing beam. The dotted lines represent the radial from the location of the radar to the grid points of the LES within the resolution volume. Along these dotted lines,  $C_n^2$  is calculated, and later weighted in range ( $W_r$ ) and beam width ( $W_b$ ). Right: the dotted line represents the axis along which  $C_n^2$  needs to be estimated. First, the value of  $n$  at level  $z$  is obtained from the LES matrix; however, at levels  $z + \Delta z$  and  $z - \Delta z$ , the dotted line does not match any of the LES grid points. In order to obtain an estimate at those heights, a linear interpolation is made using the four closest points. Finally, an average of the two estimates of structure function parameter of  $n$  (from  $z$  and  $z + \Delta z$ , and  $z$  and  $z - \Delta z$ ) with an oblique separation  $\Delta$  is computed.

Presented as a single realization in time, Figure 3.2 depicts an example of the specific humidity  $q$  vertical profile from the LES output at the center of the sub-domain, as well as the corresponding calculated profiles of refractivity  $N$ , and the horizontally averaged structure parameter of refractive index  $C_n^2$ . The observed turbulence level of  $C_n^2$  is intermediate with an enhancement of at least one order of magnitude at approximate 1000 m. This enhancement can be identified as the CBL top, and according to Table 2.3, the intensity level of turbulence is strong. The vertical profile structure of  $C_n^2$  are in excellent agreement with Figure 11.15 of Doviak and Zrnić (1993), and radar measurements of marine air over OK gave a mean of  $C_n^2 = 5 \times 10^{-13} \text{ m}^{2/3}$  and peak values as high as  $3 \times 10^{-12} \text{ m}^{2/3}$  for mid-afternoon skies (Doviak and Berger 1980; Doviak and Zrnić 1993).

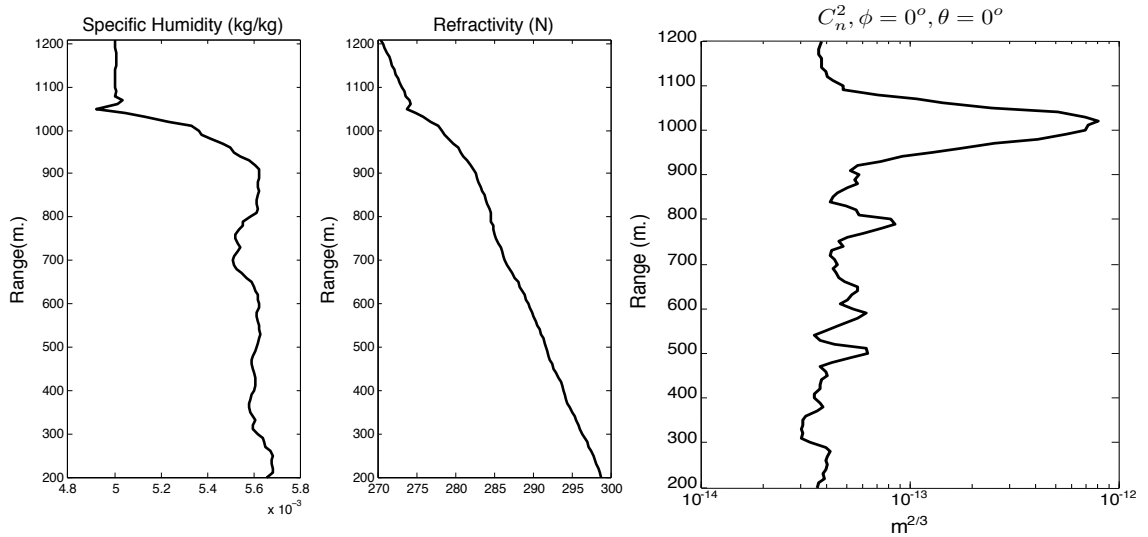


Figure 3.2: Left: vertical profile of specific humidity characteristics for the CBL. Center: vertical profile of refractivity calculated from the LES fields. Right: vertical profile of the horizontally averaged structure function parameter of refractive index  $C_n^2$ . All data were calculated from a single realization in time.

The received voltage  $V$  from the Eulerian framework is expressed in its exponential form (recall Equation (2.35)) at time  $t_0 + \Delta t$  as:

$$V(t_0 + \Delta t) = \sum_{p=1}^M A^{(p)}(t_0 + \Delta t) \exp(-j\psi_e^{(p)}(t_0 + \Delta t)), \quad (3.11)$$

$$A^{(p)}(t_0 + \Delta t) = A' \sqrt{C_n^2(t_0 + \Delta t)^{(p)} W_r^{(p)} W_{btx}^{(p)} W_{brx}^{(p)}}, \quad (3.12)$$

$$A' = \frac{\sqrt{G_{tx} G_{rx}}}{\lambda r_{tx0} r_{rx0}} \sqrt{0.0330} k_B^{-11/6}, \quad (3.13)$$

$$\begin{aligned} \psi_e^{(p)}(t_0 + \Delta t) &= \psi_0^{(p)} + k_0(r_{tx}^{(p)} + r_{rx}^{(p)}) \\ &\quad + k_0(\hat{\mathbf{e}}_{tx}^{(p)} + \hat{\mathbf{e}}_{rx}^{(p)}) \cdot \mathbf{v}^{(p)}(t_0 + \Delta t) \Delta t, \end{aligned} \quad (3.14)$$

where the amplitude  $A^{(p)}$  is proportional to the square root of  $C_n^2$  and inversely proportional to the range of the center to the resolution volume from the transmitter  $r_{tx0}$  and receiver  $r_{rx0}$ . The LES time is represented as  $t_0$  and  $\Delta t$  is the time increment which is a function of the PRT. Each individual grid point of the  $M$  points contained within the resolution volume is represented by  $p$ , and  $G_{tx}$  and  $G_{rx}$  are constants proportional to the gain of the transmitter and receiver, respectively. Random initial phase is represented as  $\psi_0^{(p)}$ ,  $k_0$  is the radar wavenumber,  $\hat{\mathbf{e}}_{tx}^{(p)}$  is the unit vector directed from the transmitter antenna to the  $p^{th}$  LES grid cell,  $\hat{\mathbf{e}}_{rx}^{(p)}$  is the unit vector directed from the receiver antenna to the  $p^{th}$  LES grid cell, and  $k_B$  is the Bragg wavenumber ( $k_B = \frac{4\pi}{\lambda}$ ). The instantaneous three-dimensional wind field  $\mathbf{v}^{(p)}$  is estimated from the LES resolved wind fields ( $u_o, v_o$ , and  $w_o$ ) and the sub-grid TKE  $E$  as:

$$u = u_o + u', \quad (3.15)$$

$$v = v_o + v', \quad (3.16)$$

$$w = w_o + w', \quad (3.17)$$

where  $u$ ,  $v$ , and  $w$  represent the resultant wind fields, and  $u'$ ,  $v'$ , and  $w'$  are the sub-grid fluctuations of the velocity fields. Under the assumptions of isotropy, the variance of the fluctuations is defined as a function of  $E$  as:

$$E = \frac{1}{2}(\sigma_u^2 + \sigma_v^2 + \sigma_w^2), \quad (3.18)$$

$$\sigma_u^2 = \sigma_v^2 = \sigma_w^2 = \frac{2}{3}E. \quad (3.19)$$

Therefore, the fluctuation component of any of the wind fields can be represented as a random Gaussian variable with zero mean and  $\sqrt{\frac{2}{3}E}$  standard deviation.

The range weighting function  $W_r$  represents the convolution between the impulse response of the receiver with the transmitted pulse and is described by (Holdsworth and Reid 1995; Scipi3n et al. 2008) as:

$$W_r(x, y, z) = \exp\left[\frac{(r - r_0)^2}{2\sigma_r^2}\right], \quad (3.20)$$

where  $r$  represents the projection of each grid point range  $\sqrt{x^2 + y^2 + z^2}$  over the pointing direction, and the variance is  $\sigma_r = 0.35c\tau_w/2$ , where  $\tau_w$  is the pulse width (Doviak and Zrni3c 1993). Finally,  $W_{btx}$  and  $W_{brx}$  represent the one-way transmitter and receiving beam pattern weighting function (Yu 2000; Cheong et al. 2004a; Scipi3n et al. 2008).

$$W_{btx}(x, y, z) = \exp\left[-\frac{(\theta_x - \bar{\theta}_{xtx})^2}{4\sigma_x^2} - \frac{(\theta_y - \bar{\theta}_{ytx})^2}{4\sigma_y^2}\right], \quad (3.21)$$

$$W_{brx}(x, y, z) = \exp\left[-\frac{(\theta_x - \bar{\theta}_{xrx})^2}{4\sigma_x^2} - \frac{(\theta_y - \bar{\theta}_{yrx})^2}{4\sigma_y^2}\right], \quad (3.22)$$

$$\theta_x = \tan^{-1}\left(\frac{x}{z}\right), \quad \theta_y = \tan^{-1}\left(\frac{y}{z}\right),$$

where  $\bar{\theta}_{xtx}$  and  $\bar{\theta}_{ytx}$  describe the transmitting antenna beam pointing;  $\bar{\theta}_{xrx}$  and  $\bar{\theta}_{yrx}$  describe the receiving antenna beam pointing in degrees for both cases; and  $\sigma_x = \sigma_y = \theta_1/2.36$  is proportional to the beamwidth. The range weighting function and beam weighting function are illustrated in the right panel of Figure 3.1.

Muschinski et al. (1999) introduced a radar simulator based on LES only with a vertical beam and for one realization in time. Improvements over that work are:

- Values of  $C_n^2$  are calculated over oblique beams along the radial.
- $C_n^2$  and velocity are interpolated at each time  $\Delta t$ .
- The location of each grid point with respect to transmitter and receiver are now part of the equation.
- Radial velocities at each LES are calculated as the resultant of both the transmitter and receiver components.
- Radar beamwidth effect is also calculated independently for the transmitter and receiver.

All these additions permit multiple frequency applications, as well as monostatic and bi-static. This allows opportunities for many experiments based on LES fields.

Since the LES generates data for variables with 1 s temporal resolution, and the radar inter-pulse period (IPP) is on the order of milliseconds, an estimation of all of the variables  $X$  at  $t_0 + \Delta t$  is needed. In order to achieve this, the desired value is calculated using the linear interpolation scheme presented by Cheong et al. (2004a):

$$X(t_0 + \Delta t) = (1 - \Delta t)X(t_0) + (\Delta t)X(t_1), \quad (3.23)$$

where  $t_0$  and  $t_1$  are two consecutive time steps of the LES, and  $\Delta t$  is the intermediate value taken from 0 to 1. Also suppose that the  $VAR(X(t_0)) = VAR(X(t_1)) = VAR(X)$ , where  $VAR(\cdot)$  denotes the variance. Thus the variance of the interpolated random variable  $X(t_0 + \Delta t)$  is:

$$VAR(X(t_0 + \Delta t)) = [(1 - \Delta t)^2 + 2\rho(1 - \Delta t)\Delta t + \Delta t^2]VAR(X), \quad (3.24)$$

which causes  $VAR(X(t_0 + \Delta t))$  to be reduced in a quadratic form as a function of  $\Delta t$  as shown in the previous equation. In order to reverse this artifact, the interpolated value can be scaled with the inverse-square-root function of the equation. Therefore, the scaled interpolated value is (Cheong et al. 2004a):

$$f'_i(x) = \frac{1}{\sqrt{(1 - \Delta t)^2 + 2\rho(1 - \Delta t)\Delta t + \Delta t^2}} f_i(x), \quad (3.25)$$

where  $\rho$  is the cross-correlation factor of  $X(t_0)$  and  $X(t_1)$ .

In order to produce realistic results from the radar simulator, it is necessary to introduce additive white Gaussian noise (AWGN) to our generated time-series data. First, the minimum power of the signal is estimated from the time-series data. Second, the variance of the background is computed based on a desired SNR. The complex white noise is generated based on the assumption that it has a Gaussian distribution described by the previously calculated variance. This procedure is independently applied to the real and imaginary components of the time-series data. The complex Gaussian noise is simply added to the original time-series data. An example of time-series data corresponding to a vertically pointing beam is presented in Figure 3.3. The complex AWGN shown was calculated for a minimum SNR of -3 dB.

## 3.2 Possible Configurations of the Virtual Radar

Some of the “virtual” experiments that will be used along with this work require special radar configurations. These configurations might require one or more virtual radars which are located at different positions with the LES sub-domain and are

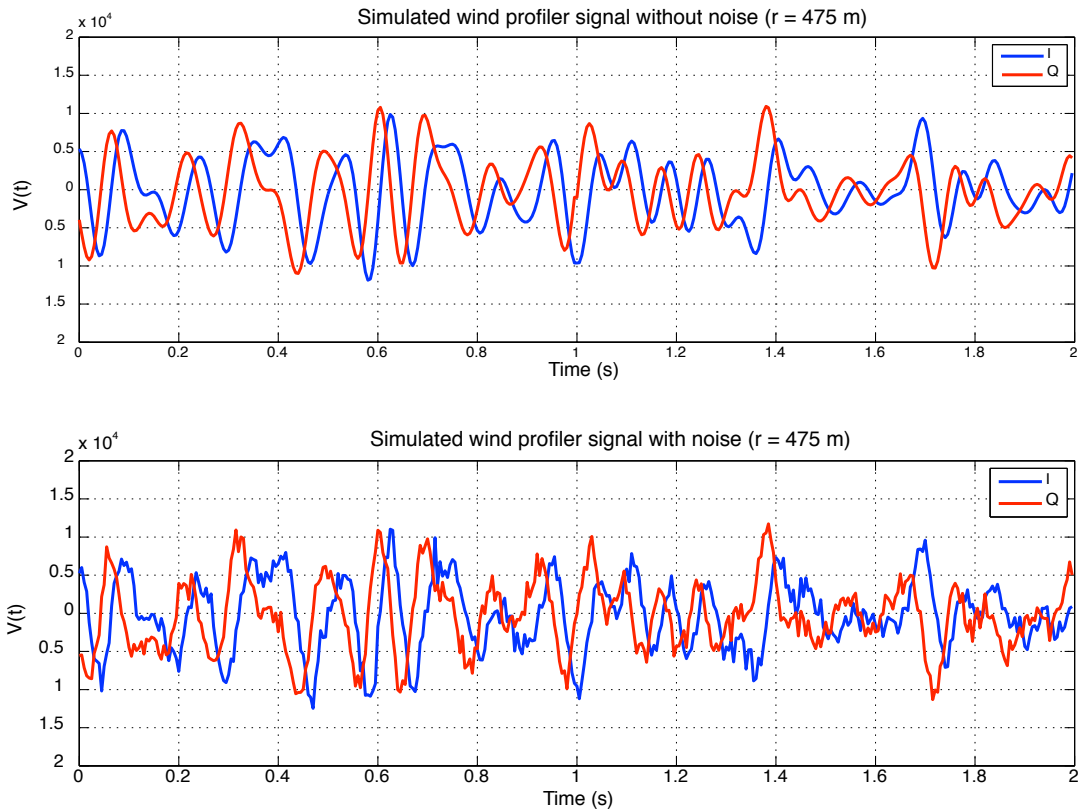


Figure 3.3: Time-series data from the simulated BLR data  $V(t)$  obtained at a range of 475 m. The blue line represents the real part (in-phase) of  $V(t)$ , and the red line is the imaginary part (quadrature) of  $V(t)$ . Top: without AWGN. Bottom: with AWGN (minimum SNR = -3 dB).

presented in the following sub-sections. Some of them may require a simplification in the radar equation, while others just include a diagram of the radar location and pointing direction to specify the experiment configuration.

### 3.2.1 Monostatic Configuration

The monostatic configuration uses the same antenna for both transmission and reception. An illustration of the beam pattern is presented in Figure 3.4. As can be observed, the resolution volume is located inside the LES sub-domain, which is represented by the rectangular volume. This configuration allows the radar to possess both a vertical and an oblique pointing beam.

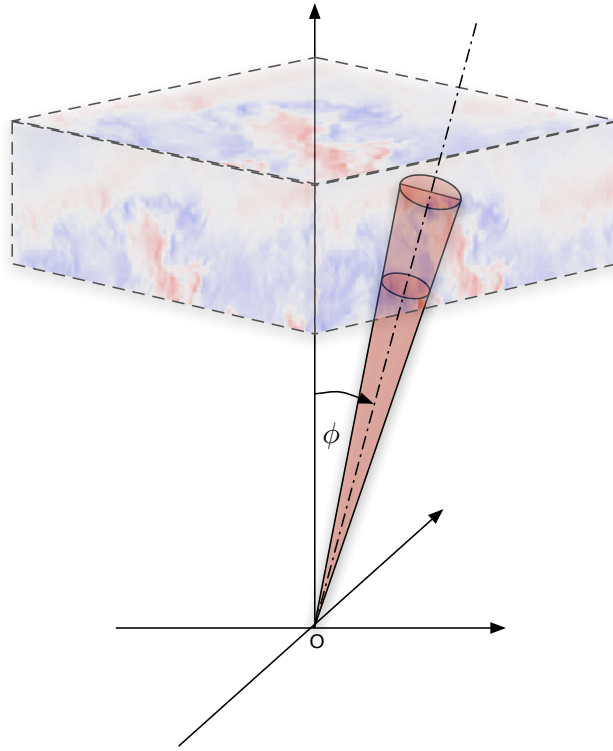


Figure 3.4: Schematic of the monostatic radar configuration. The simulated radar has the capability to point at any desired azimuth and zenith angle provided the resolution volume is located within the LES sub-domain.

As a consequence of the co-located antennas, they share the same beam-pattern weighting function. Also, the relative distance and unit vectors from each of the LES

particles to the transmitter and receiver are the same. The resulting simplified radar voltage can be expressed as (Scipi3n et al. 2008):

$$V(t_0 + \Delta t) = \sum_{p=1}^M A^{(p)}(t_0 + \Delta t) \exp(-j\psi_e^{(p)}(t_0 + \Delta t)),$$

$$A^{(p)}(t_0 + \Delta t) = A' \sqrt{C_n^2(t_0 + \Delta t)^{(p)} W_r^{(p)} W_b^{(p)}}, \quad (3.26)$$

$$A' = \frac{G}{\lambda r_0^2} \sqrt{0.0330} k_B^{-11/6}, \quad (3.27)$$

$$\psi_e^{(p)}(t_0 + \Delta t) = \psi_0^{(p)} + k_B r^{(p)} + k_B (\hat{\mathbf{e}}^{(p)} \cdot \mathbf{v}^{(p)})(t_0 + \Delta t) \Delta t, \quad (3.28)$$

where  $\hat{\mathbf{e}}^{(p)}$  represents the unit vector from the center of the antenna to the to  $p^{th}$  LES grid cell,  $G = \sqrt{G_{tx} G_{rx}}$  is proportional to the transmitted power and transmitting and receiving antenna gain, and  $r_0^2 = r_{tx0} r_{rx0}$  is the distance from the radar to the center of the resolution volume. Finally,  $W_b$  is the two-way beam weighting function (Yu 2000; Cheong et al. 2004a; Scipi3n et al. 2008):

$$W_b(x, y, z) = \exp \left[ -\frac{(\theta_x - \bar{\theta}_x)^2}{2\sigma_x^2} - \frac{(\theta_y - \bar{\theta}_y)^2}{2\sigma_y^2} \right], \quad (3.29)$$

$$\theta_x = \tan^{-1} \left( \frac{x}{z} \right), \quad \theta_y = \tan^{-1} \left( \frac{y}{z} \right).$$

By combining three or more monostatic radar beams, DBS or multiple radar configurations can be obtained, as explained next.

### 3.2.1.1 Doppler Beam Swinging

DBS is the most common configuration to estimate the three-dimensional wind fields using a single monostatic radar. In this configuration, the radar beam stays in one position for a specific amount of time (*dwell time*), then switches to the next position until all the needed beams to estimate the three wind components have been scanned. The time that takes the radar to go back to the starting beam position is called the “*scan time*”. Even though the technique only requires three non-coplanar beams, it usually uses five: one vertical beam and four oblique beams which point toward the cardinal directions. The use of more than three beams provides a better estimate of the horizontal wind while reducing the variance of the estimates. A representation of DBS is illustrated in Figure 3.5.

To obtain the wind estimates, the radial velocity of the five beams are combined after the *scan time* (see Section 2.4.1). The assumptions made in these calculations are homogeneity over the volume containing the radar beams and stationarity during the time of the scan.

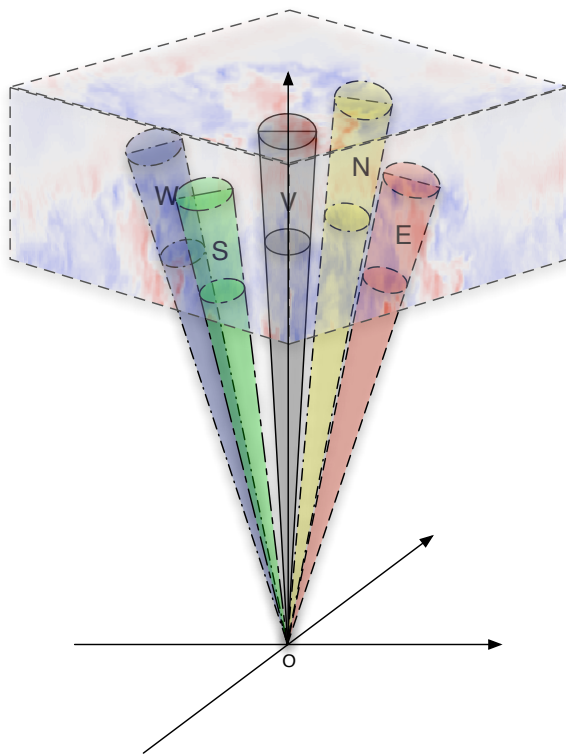


Figure 3.5: Doppler beam swinging configuration. The configuration is based in a single monostatic radar that points in five different, non-coplanar directions. Usually, the oblique beams point to the four cardinal directions.

### 3.2.1.2 Multiple Radar Configuration

The multiple radar configuration (MRC) consists of five different radars which are located equidistant from one another within the LES sub-domain. A diagram indicates the location of the radars in Figure 3.6. A vertical pointed radar is located in the center of the LES sub-domain. The other four radar beams are directed off-vertically but point towards the vertical beam of the first radar at different heights. The spacing between the heights will be chosen depending on the resolution desired for the study.

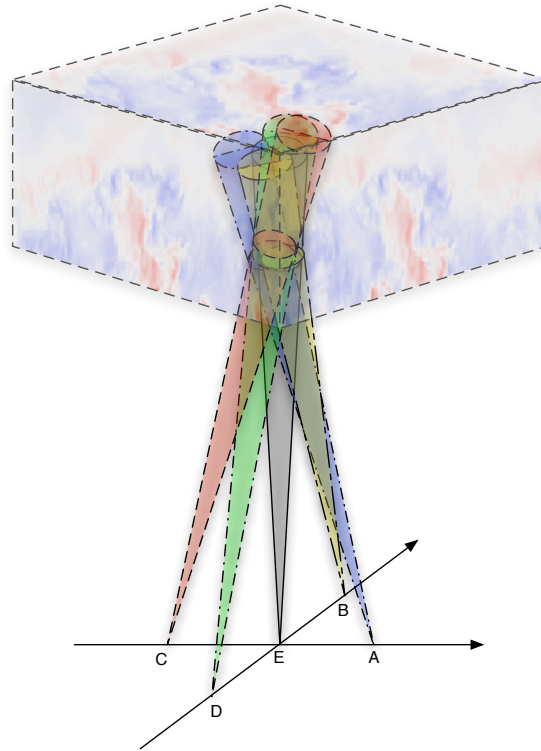


Figure 3.6: Multiple monostatic radar setup. The configuration uses the assumption that five simultaneous monostatic radars point towards the same resolution volume inside the LES.

The procedure to obtain the three-dimensional winds at each height is the same presented for DBS. However, this configuration allows us to obtain more accurate results than DBS when compared with the “true” LES fields because they do not rely on spatial homogeneity or stationarity over the dwell time. This is possible because the radar coverage volume is small in comparison with the effective DBS sampling volume, and all radars are available simultaneously. That avoids the *scan time*. Although this configuration obtained better results than DBS (Scipi3n et al. 2007), it is impractical due to expense.

### 3.2.2 Spaced Antenna

The SA technique (Briggs et al. 1950) consists a pseudo-monostatic radar where the transmitting and receiving antennas point vertically and are not collocated in the strict sense. However, the separation between the center of the antennas can be as small as the diameter of the receiving antenna. The method uses one transmitter and three or more closely spaced receivers. The common volume is reached as a consequence of the close spacing between the transmitting and receiving radar beams.

Estimates of the horizontal wind are obtained using the interferometry pattern of signals received along the baseline of pair of separate (spaced) antennas (see RxA and RxB in Figure 3.7). The calculations of the interference or diffraction pattern are based on the ACF and CCF of the received signals, and the detailed procedure is described in Section 2.4.2.

A basic diagram of the transmitting and receiving beams is illustrated in Figure 3.7. It can be observed that the transmitting and receiving beamwidths are not the same, which is certainly not a mandatory condition. In the illustration, the transmitting beamwidth is half the receiving beamwidth. Also, at low heights the transmitting and receiving beams do not intercept, which will result in erroneous calculations of the refractive pattern and, consequently, in undetermined horizontal wind estimates.

In this chapter, the radar simulator based on LES fields was presented along with the modifications and/or simplifications for different experimental setups. In the next chapter, the specific parameters for each radar simulator will be presented. Also, results and comparisons with real data will be provided.

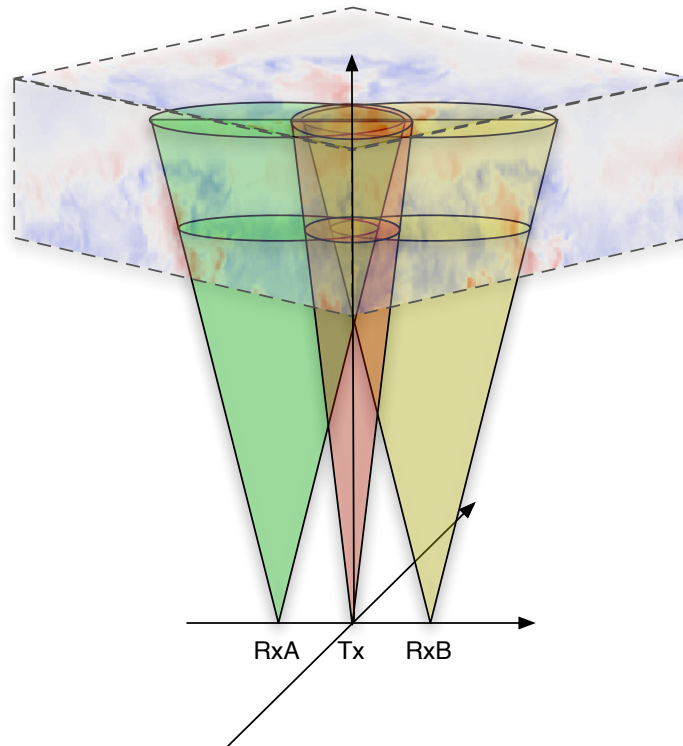


Figure 3.7: Spaced Antenna Setup. This experiment uses one antenna for transmission and three or more for reception. The distance between the transmitter (Tx) and receivers (RxA and/or RxB) is small, so it allows the beams to intercept. The different transmitter and receiver beamwidths have been incorporated in the radar simulator. Here, the beamwidth is exaggerated for diagram purposes.

## Chapter 4

# Characterization of the Boundary Layer: Validation with Realistic Data

In this chapter, the simulated radar signals based on LES fields that were presented in Chapter 3 are compared with the “true” LES fields and realistic data. The compared parameters are the structure function parameter of refractive index, the three-dimensional wind fields, the vertical velocity variance, and the vertical velocity skewness. The realistic data are obtained from the 915 MHz radar wind profiler/radio acoustic sounding system (RWP/RASS) which is located at the SGP ACRF site.

### 4.1 Experimental Configuration

The 915 MHz RWP/RASS provides wind profiles and backscattered signal strength in the height range of 0.1 km to 5 km (nominally) and virtual temperature profiles from 0.1 km to 2.5 km (see Figure 4.1). Typically, the radar operates in two modes with different range resolutions. The low-mode has a range resolution of 62.5 m and a maximum range of 2600 m, while the high-mode has a 212.55 m resolution and a maximum range of 6670 m. The radar has a 9° beamwidth, and points in the four cardinal directions with a zenith angle of 15.5°. The dwell time in each mode during the considered observation period is approximately 30 s, while the *scan time* is between 6 and 7 min. The radar simulator has a range resolution of 60 m. Consequently, only the low-mode is considered in this study. Three spectral moments are calculated based on the Doppler wind spectra downloaded from the ARM website (<http://www.arm.gov/>).



Figure 4.1: Picture of the Radial Wind Profiler (RWP) located at the SGP ACRF. In addition to the wind profiles, the system can obtain virtual temperatures through the Radio Acoustic Sounding System (RASS) co-located with the radar (Courtesy of Dr. P. Chilson).

## 4.2 Structure Function Parameter of Refractive Index

As mentioned in Chapter 2, the received radar power  $P_r$  is proportional to the radar reflectivity  $\eta$ , which is a measure of the radar scattering intensity. Also,  $\eta$  is proportional to the structure function parameter of refractive index  $C_n^2$  (see Equation (2.29)). If the radar is calibrated, profiles of  $C_n^2$  can be obtained for every radar dwell time.

Unfortunately, an accurate radar calibration can be complex, requiring detailed measurements of the various radar parameters (see Equation (2.21)), such as the transmitted power  $P_t$ , antenna gain  $G$ , radar beamwidth  $\theta_1$ , etc. After combining Equations (2.21) and (2.29) and grouping all the known radar parameters, the estimation of  $C_n^2$  can be expressed as:

$$\log C_n^2 = \log(P_r \times r^2) - 2 \log l + \log C, \quad (4.1)$$

where  $P_r \times r^2$  represents the total range-corrected power,  $C$  is the radar calibration constant, and  $l$  represents the one-way system losses.

Range-time-intensity (RTI) plots of  $C_n^2$  are presented in Figure 4.2. Here, the middle panel represents the  $C_n^2$  that was obtained directly from the LES fields for a vertically pointed radar beam. This represents the same estimate obtained from the LES parameters following the procedure described in Scipi3n et al. (2008) and used in the magnitude term of the radar simulator (see Equation (3.11)). The top panel represents the  $C_n^2$  that was obtained from the range-corrected power of the virtual BLR (RadSim). To calculate  $C_n^2$  from Equation (4.1), the loss term was omitted, and the constant  $C$  was obtained empirically by comparing the level of turbulence around the maximum of  $C_n^2$  from RadSim with the “true”  $C_n^2$  from LES. This represents a rudimentary estimate of the CBL top. Finally, in the bottom panel, there is an empirical calibration of the range-corrected SNR that was obtained from the vertical beam of the radar located at the SGP ACRF (Radar<sub>ARM</sub>) for the same date of the simulation.

As studied in Section 2.1, the LES was setup to reproduce the cloud free CBL case of June 8, 2007. Profiles of potential temperature and horizontal wind for the LES initialization were obtained from the same location as the RWP (SGP ACRF). The evolution of the LES is controlled by the turbulent kinematic heat flux for the whole simulation period obtained from the same location. However, the LES code is nudged with hourly profiles obtained from the RUC interpolated at every second. This combination gives the LES the freedom to evolve accordingly to the heat flux from LMN and RUC profiles. There is a good agreement between the estimates from the RadSim and LES, except at the lowest height where there are not enough points within the virtual resolution volume to characterize the  $C_n^2$  appropriately. Also, there is an unrealistic increase in the intensity of  $C_n^2$  observed above 1000 m at the RadSim RTI, which is caused by applying the range-corrected algorithm to regions with low SNR. Additionally, the LES RTI presents some artificial layers that appear as discrete bands at determinant heights, which are caused by residual layers present at the initialization profiles of the LES run. Finally, the LES captures the evolution of the CBL during the day. Even so, the code is apparently unable to reproduce the evolution of external atmospheric forcing, which is observed at the heights of maximum  $C_n^2$  between LES and Radar<sub>ARM</sub>. Nevertheless, the LES produces  $C_n^2$  that closely matches the trend in radar data (Botnick and Fedorovich 2008).

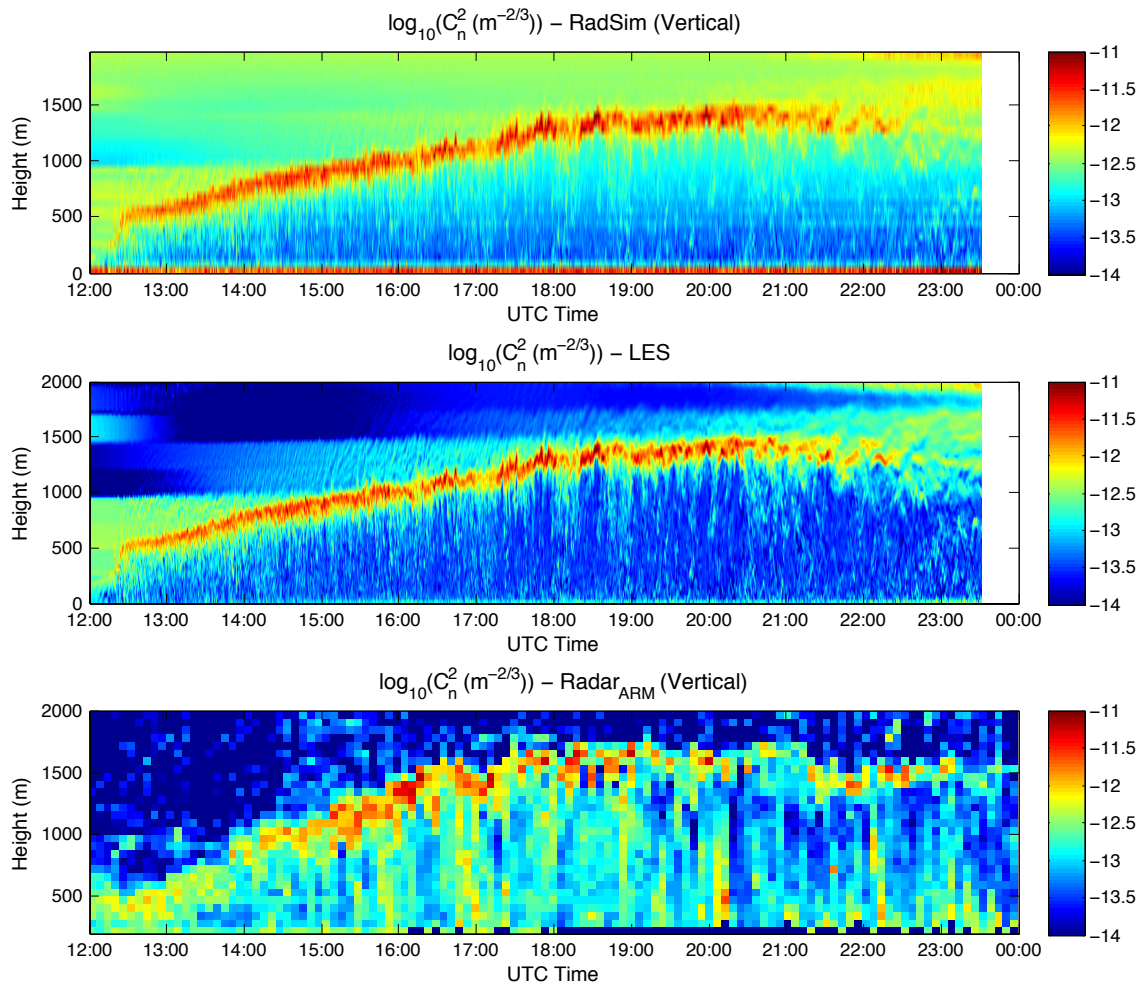


Figure 4.2: Structure function parameter of the refractive index estimates on June 8, 2007. Top: estimates from the vertical beam of the radar simulator. Middle: LES-profile at center of domain. Bottom: estimates from the vertical beam of the SGP ACRF radar.

### 4.3 Wind Field Comparisons

The following three quantities are analyzed for each of the three wind components ( $u$ ,  $v$ , and  $w$ ): DBS values calculated from the radial velocities of the virtual BLR which points in the same directions of RWP (RadSim<sub>DBS</sub>), resolved LES values along a vertical profile at the center of the simulation sub-domain (LES), and DBS estimates from the RWP (Radar<sub>ARM</sub>). Based on the *revisit time* of the RWP, wind estimates are retrieved every 12 minutes. In order to provide a fair comparison between the three quantities, the averaging time for RadSim<sub>DBS</sub> and LES velocities is also set to 12 min.

The following procedure is used to obtain the RadSim<sub>DBS</sub> values. First, radial velocities from each of the five virtual BLR beams are estimated with a dwell time of 30 s. Second, velocity samples are computed every 6 min corresponding to the scan time of the RWP measurements. Third, the velocities are averaged over 12-min periods based on the DBS revisit time. Finally, the DBS technique is used to retrieve the three wind components. The LES data are averaged in time to obtain 12-min estimates used for comparison. Radial velocities from Radar<sub>ARM</sub> are averaged over the same time period. Values with SNR<sub>≤</sub>-10 dB are censored from further analysis.

Values of the three wind components obtained by different techniques are presented in Figures 4.3 (zonal), 4.4 (meridional), and 4.5 (vertical). The RadSim<sub>DBS</sub> estimates do not appear as smooth as those from LES. This is primarily due to the realistic noise contamination and associated measurement error. In general, the wind fields retrieved from LES of the fair CBL case, in terms of the classification applied in Botnick and Fedorovich (2008), agree well with the Radar<sub>ARM</sub> estimates. The observed discrepancies (especially, in the zonal and vertical winds) seem to result from the evolution of external atmospheric forcing, which is unaccounted for in this version of the LES code. The LES is initialized using data from a rawinsonde launched at 11:30 UTC at the SGP ACRF site. The background atmospheric state represented by this initial sounding is assumed to be steady throughout the simulation. Therefore, evolution of turbulence fields within the CBL is determined entirely by surface heating. It is reproduced realistically based on data from surface heat balance measurements at the SGP ACRF site and the variable geostrophic forcing. The agreement observed between the LES and the Radar<sub>ARM</sub> reflects the extent of the LES code's ability to reproduce the basic properties of the evolving CBL flow fields.

The relationship between the  $\text{RadSim}_{DBS}$  and the  $\text{Radar}_{ARM}$  demonstrates how the virtual BLR is able to reproduce these fields similarly to the real radar.

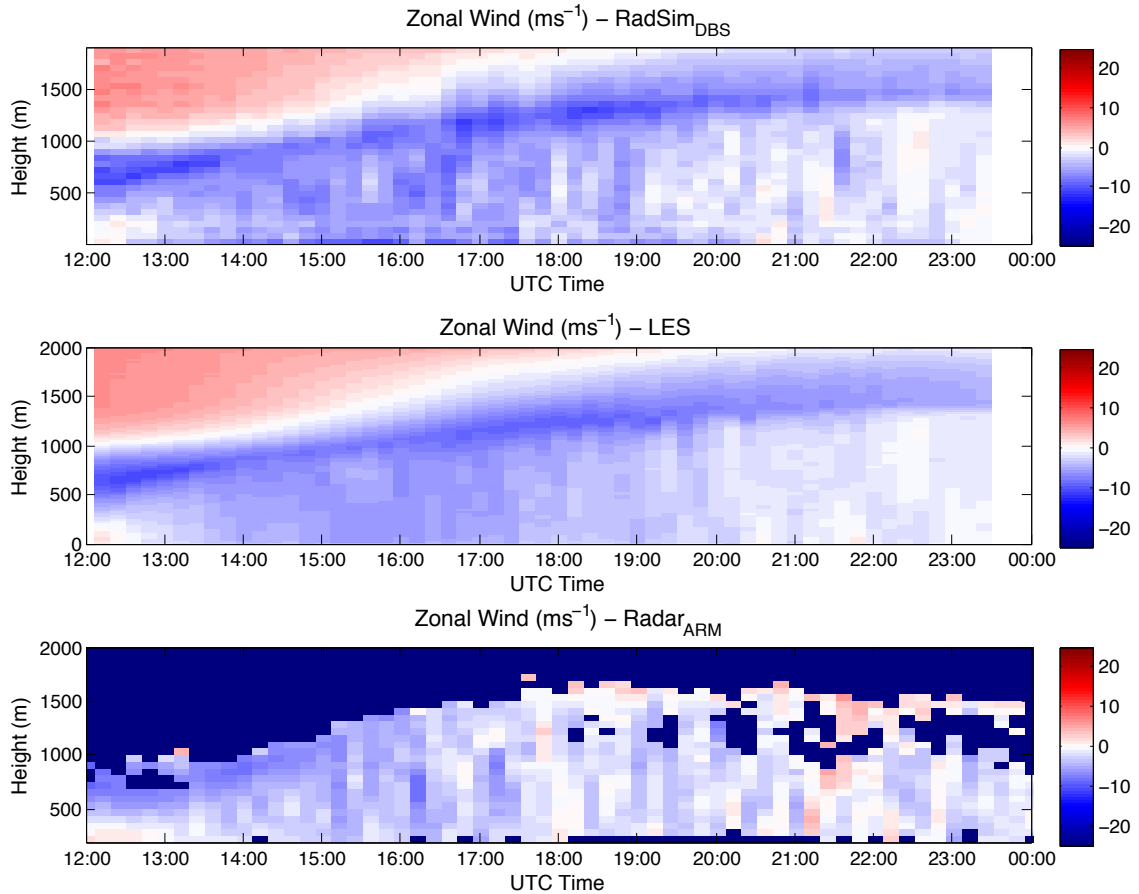


Figure 4.3: Zonal wind estimates averaged every 12 min on June 8, 2007. Top: LES-DBS. Middle: LES-Profile at center of domain. Bottom: DBS estimates from the SGP ACRF radar.

To quantify the wind parameters, two cross-sectional cuts are made in the wind fields referring to altitudes  $\sim 530$  m and  $\sim 1030$  m. Wind component estimates for all three sources are presented in Figure 4.6 along with corresponding sounding data at 12:00, 18:00, and 00:00 UTC. There is a general agreement between the estimates from  $\text{RadSim}_{DBS}$ , LES, and the sounding data for both heights and at all times. The agreement between the estimates from the LES and  $\text{Radar}_{ARM}$  is especially good for low elevations. The reason for this agreement is that the wind estimates for all quantities at that altitude correspond to the CBL mixed layer region.

There are some discrepancies at higher altitudes partially due to low SNR at particular time intervals. An additional cause might be attributed to the horizontal

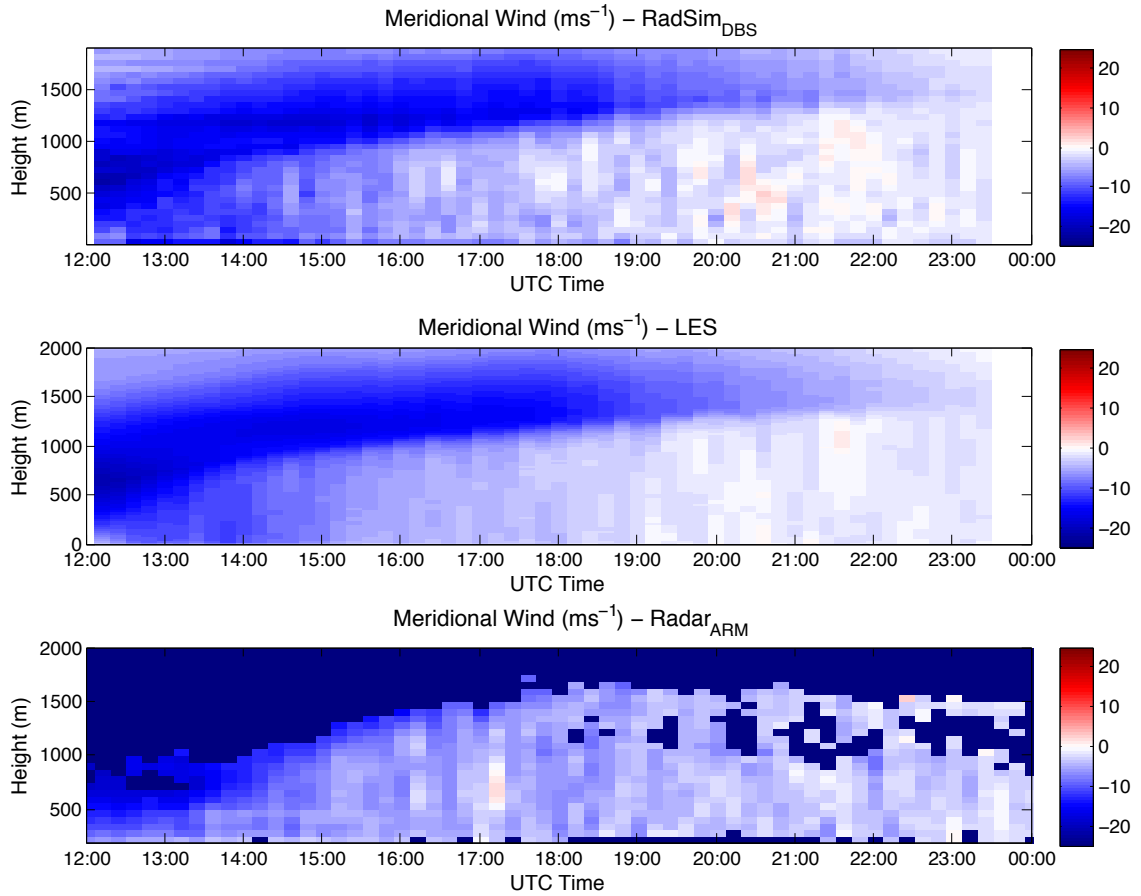


Figure 4.4: Meridional wind estimates averaged every 12 min on June 8, 2007. Top: LES-DBS. Middle: LES-Profile at center of domain. Bottom: DBS estimates from the SGP ACRF radar.

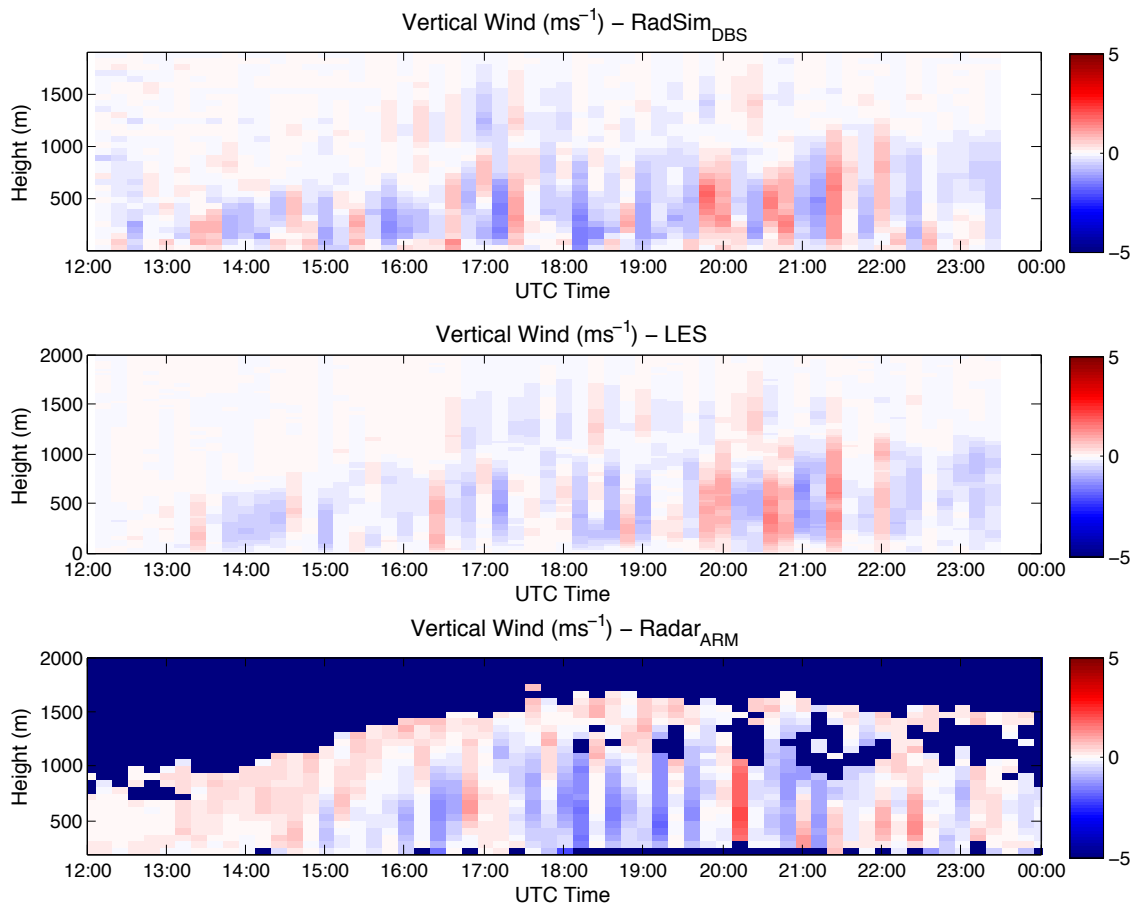


Figure 4.5: Vertical wind estimates averaged every 12 min on June 8, 2007. Top: LES-DBS. Middle: LES-Profile at center of domain. Bottom: DBS estimates from the SGP ACRF radar.

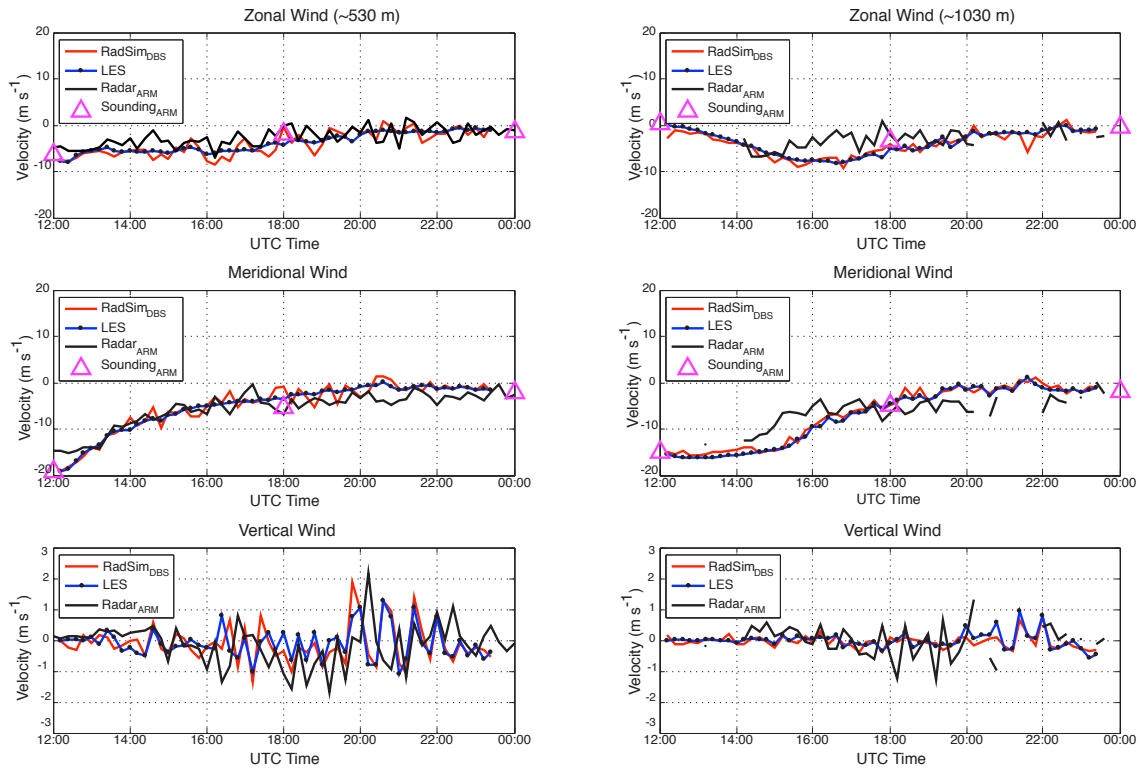


Figure 4.6: Wind comparison from the RadSim<sub>DBS</sub>, LES, Radar<sub>ARM</sub>, and a sounding (launched at three different times: 12:00, 18:00, and 00:00 UTC) at ~530 m (left) and ~1030 m (right) on June 8, 2007. Top: zonal wind. Middle: meridional wind. Bottom: vertical velocity.

shear of vertical velocity (see Section 5.1), which can bias the horizontal wind field estimates when the CBL is very active. Another cause for the observed discrepancies is the apparent inability of the LES code in its current version to account for the evolution of environmental (larger-scale) forcing, whose contribution at certain stages of the CBL evolution is comparable to the effects of simulated surface and shear forcing. This causes the pace of the CBL growth in the LES to be more gradual than is observed at the SGP ACRF site and reproduced by the local radar. For instance, wind field estimates at approximately 1030 m correspond to different CBL regions. In the Radar<sub>ARM</sub>, this elevation is within the mixed layer, while for the LES and RadSim<sub>DBS</sub>, the estimated wind refers to an elevation with two different CBL regions. Before 15:45 UTC, the free atmosphere above the CBL top, and after 15:45 UTC, the mixed layer inside the CBL. The estimations of the different regions for the LES and RadSim<sub>DBS</sub> are obtained based on  $C_n^2$ , which were presented in Section 4.2.

## 4.4 Vertical Velocity Variance

The values of vertical velocity  $w$  obtained by all three techniques (LES, RadSim<sub>DBS</sub>, and Radar<sub>ARM</sub>) are used to estimate the vertical variance of  $w$ . With regard to the LES, this procedure involves estimating the fluctuating component of the vertical velocity ( $w'$ ) from the time series of the resolved  $w$  field retrieved from the LES output for a particular location (center of the LES domain). To account for the effect of sub-grid turbulence, a sub-grid component of variance is added to the resolved variance (Equation (4.2)). This component is represented (assuming isotropy of the sub-grid turbulence) by two thirds of the time-averaged values of the sub-grid turbulence kinetic energy.

$$\sigma_w^2(LES) = \overline{w'w'} + \frac{2}{3}\overline{E}, \quad (4.2)$$

$$\sigma_w^2(Radar) = \overline{w'w'}, \quad (4.3)$$

where the over-bar represents a time average. Before calculating the deviation from the mean, a linear de-trending procedure is performed for all the vertical wind estimates (Angevine et al. 1994a). Estimates of the vertical velocity variances from RadSim, LES, and Radar<sub>ARM</sub> for the CBL case of June 8, 2007 applying an averaging time of two hours for different periods of time (14:00-16:00; 16:00-18:00; 18:00-20:00; and 20:00-22:00 UTC) are presented in Figure 4.7. The CBL top is also presented in the same figure as a horizontal dashed line at each of the averaged periods as a

reference. The CBL/inversion layer top estimated from the maximum of the LES  $C_n^2$  from Section 4.2 is located at 850 m, 1050 m, 1100 m, and 1250 m for each averaged period, respectively. The LES  $w$  field, considered as a reference data source, and RadSim vertical velocity are sampled every 6 min. The averaging and sampling times used clearly filter the high frequency components of the variance, especially for LES. However, their use is justified for realistic comparisons with the RWP at SGP ACRF since the vertical velocity estimates from the Radar<sub>ARM</sub> are obtained after each *re-visit time*. Later, in Section 5.2.2, a more appropriate study of the vertical velocity variance obtained from LES and RadSim will reveal that the best agreement between the estimates are obtained when the calculations are made with high-temporal resolution (at each dwell time  $\sim 30$  s), which avoids the filtering of the high frequency components of the vertical velocity.

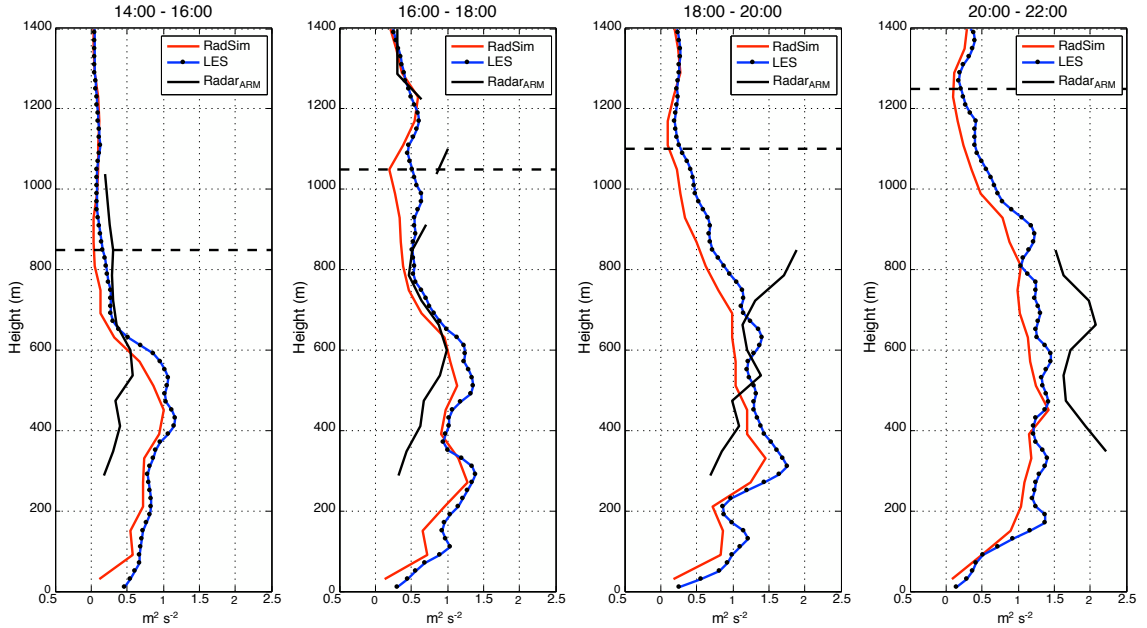


Figure 4.7: Vertical velocity variance as a function of height for different periods of time from left to right (14:00-16:00; 16:00-18:00; 18:00-20:00; and 20:00-22:00 UTC). Red line: estimates from the virtual BLR. Blue line: estimates from the LES. Black line: estimates from the BLR located at the SGP ACRF site. The horizontal dashed line represents the CBL top obtained from the LES  $C_n^2$  maximum averaged over the period under study.

The decrease in the vertical velocity variance observed (especially noticeable in the RadSim profiles) is a clear indication of the CBL/inversion layer top. As can be seen in the plot, the drop in variance corresponds roughly to the upper boundary of the CBL, and the height of this feature increases over time as the CBL continues to develop. For

the four periods, the minimum is observed at approximately 850 m, 1050 m, 1100 m, and 1250 m for the 14:00-16:00; 16:00-18:00; 18:00-20:00; and 20:00-22:00 UTC period, respectively. These results are in excellent agreement with the estimates obtained as reference from  $C_n^2$ . The discrepancy between the RadSim and the LES estimates are  $\leq 1.4 \text{ m}^2 \text{ s}^{-2}$  and may be in part to the differences in spatial and temporal extent of the vertical velocity samples and to the noise added to the simulated time-series data. The primary cause of discrepancies in the  $w$  variance profile shapes from the LES and Radar<sub>ARM</sub> estimates is attributed to the aforementioned inconsistency of prediction of the CBL depth evolution associated with external forcings.

## 4.5 Vertical Velocity Skewness

The skewness of the vertical velocity in the CBL is a signature feature of the CBL flow structure (Moeng and Rotunno 1990):

$$skewness = \frac{\overline{w'w'w'}}{(\overline{w'w'})^{\frac{3}{2}}}. \quad (4.4)$$

Positive  $w$  skewness throughout the main portion of the CBL is indicative of localized and intense upward vertical motions (updrafts) as compared to relatively widespread and gentle downward motions (downdrafts) (see Figure 2.3). The height dependence of the vertical velocity skewness in the CBL has been previously analyzed using LES in conjunction with observations (Moeng and Rotunno 1990) and LES in conjunction with wind tunnel measurements (Fedorovich et al. 1996, 2001). The chosen sampling period filters the high frequency components of the spectrum and skewness as well, but it is the most appropriate for comparisons with real data. Here, we calculate vertical profiles of skewness using vertical velocity data from RadSim, LES, and Radar<sub>ARM</sub> for the CBL case of June 8, 2007 applying an averaging time of two hours for different stages of the CBL evolution (14:00-16:00; 16:00-18:00; 18:00-20:00; and 20:00-22:00 UTC). The vertical velocity fields from LES and RadSim are sampled every 6 min to reproduce the revisit time of the Radar<sub>ARM</sub>. The results are presented in Figure 4.8 for comparison. Note that the estimates of skewness from all three sources exhibit similar behavior. That is, within the main portion of the CBL, the values are found to be positive. This is consistent with the large-scale pattern in the vertical velocity, which is characteristic of the mixed layer. Skewness increases in magnitude and range of positive values of  $w$  toward the CBL top; this growth can be clearly identified at each time period.

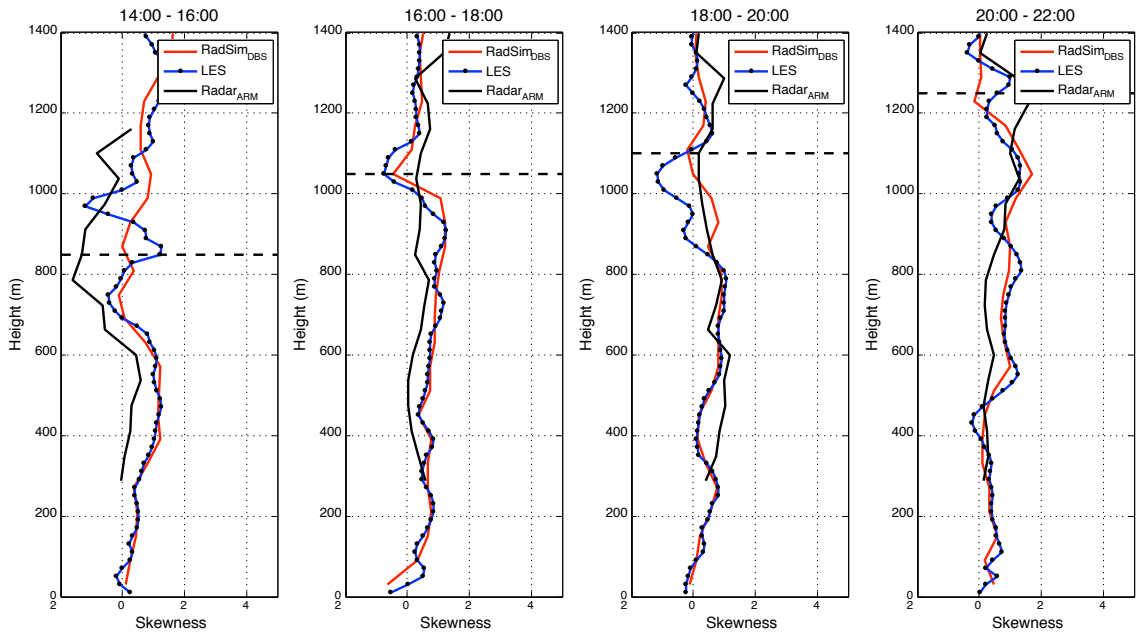


Figure 4.8: Skewness of the vertical velocity as a function of height for different periods of time from left to right (14:00-16:00; 16:00-18:00; 18:00-20:00; and 20:00-22:00 UTC). Red line: estimates from the virtual BLR. Blue line: estimates from the LES. Black line: estimates from the BLR located at the SGP ACRF site. The horizontal dashed line represents the CBL top obtained from the LES  $C_n^2$  maximum averaged over the period under study.

In the simulated CBL, the skewness reaches a maximum near the base of the inversion, and then drops to zero in the interior of the inversion layer, where the upward component of turbulent motion is in approximate equilibrium with the downward component (Fedorovich et al. 2001). From 14:00 to 16:00 UTC, the increase in skewness is observed at approximately 600 m, reaching the top of inversion layer at nearly 750 m. In this period, the skewness estimates are rather inconsistent and, as a consequence, the estimate of the CBL top based on the skewness profile appears to be unreliable. For the other time periods (16:00-18:00; 18:00-20:00; and 20:00-22:00 UTC), the maximum in skewness occurs at 900 m, 950 m, and 1100 m; and the CBL/inversion layer top estimated from vertical velocity variance and the maximum of  $C_n^2$  are located at 1050 m, 1100 m, and 1250 m, respectively. Coincidentally, the difference between the estimates from the vertical velocity variance, and the maximum in skewness is 150 m. Radar estimates of skewness agree well with the LES estimates and are similar to those presented in Fedorovich et al. (1996, 2001). While analyzing the obtained skewness profile, one should keep in mind that skewness is extremely sensitive to the sample size, which in the reported retrieval procedures was rather small due to the necessity of bringing data from all sources to one sampling time window that corresponds to the radar revisit time.

In this chapter, estimates of  $C_n^2$ , three-dimensional winds, vertical velocity variance, and vertical velocity skewness have been compared between LES and RadSim<sub>DBS</sub>. These estimates have also been contrasted with “real” radar data obtained from the RWP located in SGP ACRF. Even when the average time for comparison is set too high ( $\sim 12$  min for wind comparisons and  $\sim 6$  min for vertical velocity variance and vertical velocity skewness), which corresponds to the RWP *revisit time*, it is acceptable for realistic comparisons. The obtained results are satisfactory in all studied cases. This confirms the ability of the LES to reproduce the real atmosphere.

In the next chapter, the horizontal shear of vertical velocity effect will be investigated in depth using theoretical formulations and comparisons using LES fields and virtual radar. Also, turbulence kinetic energy will be obtained from the DBS wind estimates and analyzed for different averaging periods. Finally, the turbulence (eddy) dissipation rate will be obtained from the Doppler spectrum width for the five DBS beams and compared with the estimates obtained from LES.

## Chapter 5

# Comparison between LES and Virtual Boundary Layer Radar

Virtual radar estimates of structure function parameter of refractive index, three-dimensional winds, vertical velocity variance, and vertical velocity skewness have been compared with their corresponding estimates obtained directly from LES, in Chapter 4. These estimates have been contrasted with “real” data from the wind profiler located in LMN, OK for the date of the simulation with good agreement. This confirms the ability of the LES code to accurately reproduce the CBL. Here, the effect of horizontal shear of vertical velocity on horizontal wind estimations will be studied, along with turbulence kinetic energy and turbulence-eddy dissipation rate for different conditions.

## 5.1 Effect of Horizontal Shear of Vertical Velocity on Horizontal Wind Estimates

### 5.1.1 Theoretical Formulation

#### 5.1.1.1 Doppler Beam Swinging

In order to estimate winds, DBS technique assumes that the three-dimensional wind components are constant across the region defined by the beam locations (see Section 2.4.1). However, if the vertical velocity assumption is not considered constant

within the DBS sampling volume and the horizontal components of the vertical velocity shear are introduced, then the equations for the radial velocity for any oblique beam can be written as:

$$v_r(\theta, \phi) = u_o \sin \phi \sin \theta + v_o \sin \phi \cos \theta + w \cos \phi, \quad (5.1)$$

$$w = w_o + s_u z_o \tan \phi \sin \theta + s_v z_o \tan \phi \cos \theta, \quad (5.2)$$

$$s_u = \frac{w_u - w_o}{z_o \tan \phi}, \theta = 90^\circ, \quad (5.3)$$

$$s_v = \frac{w_v - w_o}{z_o \tan \phi}, \theta = 0^\circ, \quad (5.4)$$

where  $z_o$  is the vertical range where the radial velocity is calculated;  $w$  is the true vertical velocity at the beam position;  $w_u$  and  $w_v$  represent the true vertical velocity at the zonal and meridional directions, respectively; and finally,  $s_u$  and  $s_v$  represent the horizontal shear components of the vertical velocity caused by the horizontal gradient in the true vertical velocity ( $w$ ) and the assumed constant mean vertical wind ( $w_o$ ) within the DBS sampling volume.

Regrouping terms leads to an expression similar to the one presented in Equation (2.55) for radial velocity:

$$\begin{aligned} v_r(\theta, \phi) &= (u_o + s_u z_o) \sin \phi \sin \theta + (v_o + s_v z_o) \sin \phi \cos \theta + w_o \cos \phi, \\ v_r(\theta, \phi) &= \tilde{u} \sin \phi \sin \theta + \tilde{v} \sin \phi \cos \theta + w_o \cos \phi, \end{aligned} \quad (5.5)$$

where  $\tilde{u} = u_o + s_u z_o$  and  $\tilde{v} = v_o + s_v z_o$  are the DBS-measured zonal and meridional wind biased by the horizontal shear of the vertical wind in the  $x$  and  $y$  direction, respectively. The solution to the set of equations of radial velocities for multiple beams shows that the horizontal shear effect caused by the vertical velocity cannot be separated from the horizontal wind estimates.

### 5.1.1.2 Spaced Antenna

The generalized theoretical expression that includes the shear terms for the CCF used in spaced antenna interferometry is presented in Zhang and Doviak (2007). However, the equations have been derived for a horizontal pointing weather radar. This theory needs to be adapted for a vertically pointing wind profiler in the same fashion that

is presented in Doviak et al. (1996), and Holloway et al. (1997), and Equation (2.61). The modified equation is presented below:

$$c_{12}(\tau) = \exp \left[ -2jk_o w_o \tau - 2k_o^2 (\sigma_r^2 s_w^2 - \sigma_t^2) \tau^2 - \beta_h^2 \left[ (u_o + s_u z_o) \tau - \frac{\Delta x}{2} \right]^2 - \beta_h^2 \left[ (v_o + s_v z_o) \tau - \frac{\Delta y}{2} \right]^2 - \frac{1}{8} \left( \frac{w_o \tau}{\sigma_r} \right)^2 \right], \quad (5.6)$$

where  $s_u$ ,  $s_v$ , and  $s_w$  are the three components of the vertical velocity shear. The effects of the vertical wind  $w_o$  and vertical shear  $s_w$  are typically small and will be omitted in the future (Holloway et al. 1997; Zhang and Doviak 2007).

By re-writting the magnitude of Equation (5.6) in a more convenient form, the expression for the normalized ACF and CCF are obtained. The expressions are similar to Equations (2.62) and (2.63):

$$|c_{11}(\tau)| = \exp \left[ -\beta_h^2 (\tilde{u}^2 + \tilde{v}^2) - 2k_o^2 \sigma_t^2 \tau^2 \right] + \frac{N}{S} \delta(t), \quad (5.7)$$

$$|c_{12}(\tau)| = \exp \left[ -\beta_h^2 \left( \tilde{u} \tau - \frac{\Delta x}{2} \right)^2 - \beta_h^2 \tilde{v}^2 \tau^2 - 2k_o^2 \sigma_t^2 \tau^2 \right], \quad (5.8)$$

where  $\tilde{u} = u_o + s_u z_o$  and  $\tilde{v} = v_o + s_v z_o$  are the SA measured wind components in the  $x$  and  $y$  direction, respectively. They represent the baseline wind biased by the baseline shear (Zhang and Doviak 2007). These equations are the same as the ones presented in Holloway et al. (1997) and Section 2.4.2 and are used to estimate the measured wind and turbulence. Once again, it is clear that it is impossible to separate the horizontal shear component of the vertical velocity from the measured wind. If the horizontal shear term is significantly large, the estimates of the horizontal wind will be erroneous.

To calculate the magnitude of the effect of the shear in both simulations of DBS and SA techniques, a constant amount of shear of vertical velocity will be applied to the zonal wind. In this way, the amount of bias will be measured and compared between the simulated and the theoretical described previously.

### 5.1.2 Test Configurations

A controlled experiment is setup in order to quantify the effects of the vertical velocity shear in the horizontal wind estimates. Of all the LES fields used in the radar simulator presented in Section 3.1, the only quantities that are variables here are the

Table 5.1: Description of the field domain used by the radar simulators

Property	Specification
Number of grid points	$70 \times 70 \times 100$
Spatial resolution	20 m
Time step	1 s
Dimensions of the sub-domain	$1400 \times 1400 \times 2000 \text{ m}^3$
Variables	$u, v, w$
Constants	$E, q, \Theta$

wind components. The amplitude of the signal is assumed to be constant and to have high SNR. The parameters used in the radar simulators are presented in Table 5.1.

The meridional wind is set to be constant and equal to  $5 \text{ m s}^{-1}$ . The zonal wind is variable and changes from  $-15 \text{ m s}^{-1}$  to  $15 \text{ m s}^{-1}$  in steps of  $0.125 \text{ m s}^{-1}$ . The vertical velocity fields are generated (using Equation (5.2)) with shear only in the zonal direction ( $s_v = 0$ ). The magnitude of the vertical velocity is controlled using an external parameter called “vertical velocity fraction” (*sfrac*) and denotes the fractional contribution of the shear in the range of 0 to 1. That is, when *sfrac* is 0, the vertical velocity is set to zero; when it is one, the vertical velocity is set to the maximum shear.

### 5.1.2.1 DBS Configuration

The main parameters used in the DBS simulation are presented in Table 5.2. The experiment setup consists of generating 5 beams: one vertical and four steered at  $15.5^\circ$  off-vertical along 4 azimuth angles:  $0^\circ$ ,  $90^\circ$ ,  $180^\circ$ , and  $270^\circ$ . Radial velocities are estimated using the spectral moments, which are later used to calculate the wind components.

Presented in Figure 5.1 are the zonal wind estimates calculated using different values of *sfrac* versus the ideal zonal wind. The x-axis in the scatter plot represents the “ideal” zonal winds used by the radar simulator. The y-axis represents the measured zonal wind ( $\tilde{u}$ ) for the different shear conditions. The estimates have a correlation of 0.99 for the three presented cases of Figure 5.1. However, as the shear increases (controlled by *sfrac*), bias increases. This increase in bias is observed as a displacement of the wind estimates toward larger values (see right panel of Figure 5.1).

Table 5.2: Specifications of DBS configuration

Quantity	Value
Frequency	915 MHz
Wavelength	32.8 m
Full half-power beam width	9°
Inter-Pulse Period	10 ms
Resolution	60 m
Range ( $z_o$ )	1650 m
Beam inclination	variable
Simulation Time	30000 s

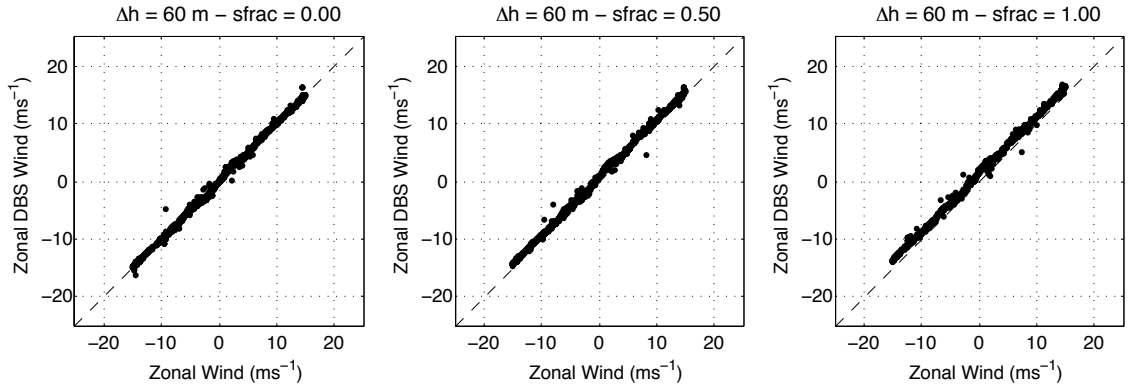


Figure 5.1: Zonal wind estimates obtained using DBS for different shear conditions. Left:  $sfrac = 0.00$  (no shear). Middle:  $sfrac = 0.50$ . Right:  $sfrac = 1.00$ .

In this unique situation,  $w$  at each DBS beam direction is recorded directly from the input vertical wind field. The ideal bias for DBS is also referred to as “range corrected shear ( $s_u z_o$ )”, and it is plotted as a continuous line in Figure 5.2. The cumulative bias calculated from the DBS zonal wind estimates plotted in Figure 5.1 for the different  $sfrac$  conditions are plotted as dots.

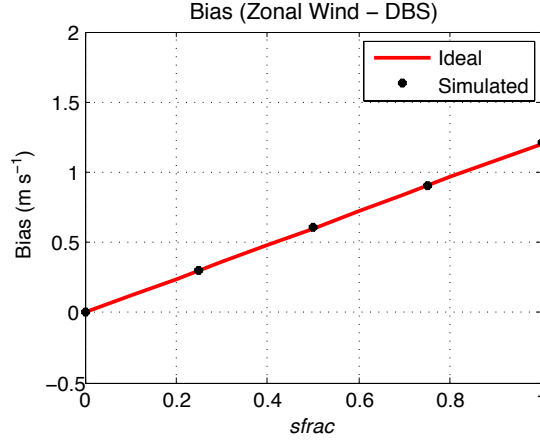


Figure 5.2: Zonal wind bias. Line: Ideal bias. Dots: estimated from the DBS simulation for different values of  $sfrac$ .

The correlation between the ideal bias calculated from  $w$  using Equation (5.3) and the cumulative error obtained from the data presented in Figure 5.1 for the different values of  $sfrac$  is extremely high. The simulated values are well represented by the theory. When  $sfrac$  is zero, the bias is zero, and when  $sfrac$  is one, the bias is maximum. The mean square error (MSE) between the measured and theoretical bias from Figure 5.2 is  $1.55 \times 10^{-4} \text{ m}^2 \text{ s}^{-2}$ .

### 5.1.2.2 Spaced Antenna Configuration

Four closely spaced receivers (see Figure 5.3) are used to estimate the zonal and meridional wind using the SA technique. The transmitter is located at the center of the sub-domain. Furthermore, the receivers are located in a cross-configuration: receivers RxA and RxB are located in the zonal direction at -0.25 m and 0.25 m, respectively. Receivers RxC and RxD are located in the meridional direction at -0.25 m and 0.25 m, respectively. This configuration is designed to allow for direct determination of the horizontal wind components along each baseline. The parameters used in the SA simulation are described in Table 5.3.

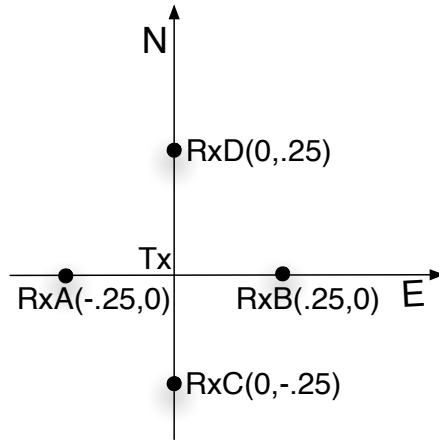


Figure 5.3: Diagram showing the location of the SA transmitter (Tx) and receivers (RxA, RxB, RxC, and RxD). The black dots represent the location of the four receivers in the cross-configuration. As noted, they are located symmetrically, with respect to the Tx, along the zonal and meridional axes.

Table 5.3: Specifications of SA configuration

Quantity	Value
Frequency	915 MHz
Wavelength	32.8 m
Full half-power transmitter beam width	9°
Full half-power receiver beam width	18°
Number of receivers	4
Inter-Pulse Period	2 ms
Resolution	60 m

Zonal wind estimates for the different *sfrac* cases versus the ideal zonal wind are presented in Figure 5.4. As in Figure 5.1, the y-axis corresponds to the zonal wind estimates but the estimates are obtained using the FCA-Gaussian for the SA technique (see Section 2.4.2). The correlation for the SA case for the different *sfrac* values is 0.99. However, the estimates are not aligned as well as in the case of DBS. The effect of the shear in the estimates can still be seen (i.e., the estimates shift up in value as *sfrac* increases).

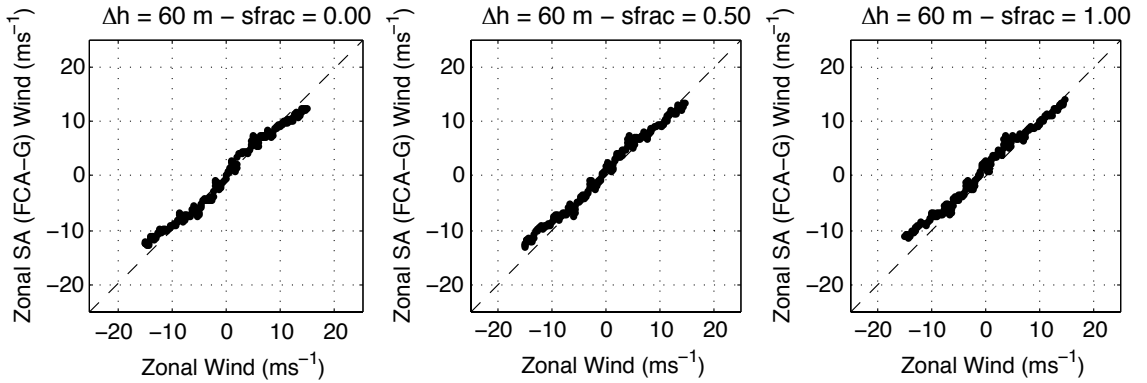


Figure 5.4: Zonal wind estimates obtained using SA for different shear conditions. Left: *sfrac* = 0.00 (no shear). Middle: *sfrac* = 0.50. Right: *sfrac* = 1.00.

The shear applied to both SA and DBS techniques are the same. However, in contrast to DBS, the ideal bias for the SA is calculated within the resolution volume as the averages of the vertical velocities gradient along the *x* and *y* directions. The ideal bias for the SA case is the same as the DBS bias, and it is plotted as a continuous line in Figure 5.5. The cumulative measured bias for the different *sfrac* values obtained from Figure 5.4 are presented as black dots. The MSE for the SA (FCA-G) obtained from Figure 5.5 is  $1.83 \times 10^{-2} \text{ m}^2 \text{ s}^{-2}$ , and is larger than the one calculated from DBS.

The good agreement between the ideal bias and the cumulative bias obtained from the zonal wind estimates for DBS and SA techniques supports the theoretical formulation of the horizontal shear of vertical velocity effect in the horizontal wind estimates.

### 5.1.3 Results

After the theory has been validated through a controlled experiment in the previous sections, it is pertinent to study the effect of the horizontal shear of vertical velocity

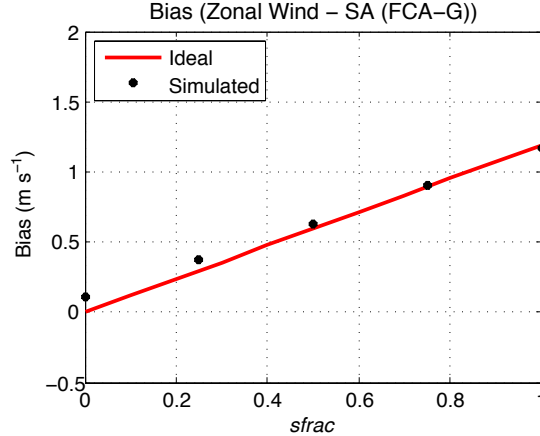


Figure 5.5: Zonal wind bias. Line: Ideal bias. Dots: estimated from the SA simulation for different values of *sfrac*.

under realistic conditions. For this study, radar signals for both techniques (DBS and SA) are simulated for approximately 8 hours of the LES run and within the LES sub-domain. The simulated radar signals follow the same parameters presented in Table 5.2 for DBS and Table 5.3 for SA. To produce realistic signals, AWGN has been added to the radar signals obtained at each receiver (see top panel of Figure 5.6). As a consequence, wind estimates at certain sectors are not reliable due to low SNR. The SNR threshold used for censoring the radar signals is set to -3 dB. However, due to initialization parameters of the LES, the returned signal from a residual layer found at the beginning of the simulation is not removed. Usually, turbulence above the BL top is weak, so the wind estimates are not reliable and have been removed. The procedure used consists of estimating the maximum of the  $C_n^2$ , which matches the maximum of the SNR (see asterisks at the top panel of Figure 5.6) corresponding to an estimate of the BL top (see Section 4.2). Any estimates above the BL top are censored (see bottom panel of Figure 5.6).

Estimates of horizontal wind ( $\tilde{u}$  and  $\tilde{v}$ ) are analyzed for three different quantities: resolved LES values along a vertical profile at the center of the simulation sub-domain, DBS estimates calculated from the radial velocities of the virtual BLR pointing in the five directions, and SA estimates calculated from the four spaced receivers. The averaging time chosen for all the estimates is 5 min.

To obtain the DBS values, the following procedure is used. First, radial velocities from each of the five virtual BLR beams are estimated with a dwell time of 30 s. Second, velocity samples are computed every 2.5 min representing the DBS *scan time*.

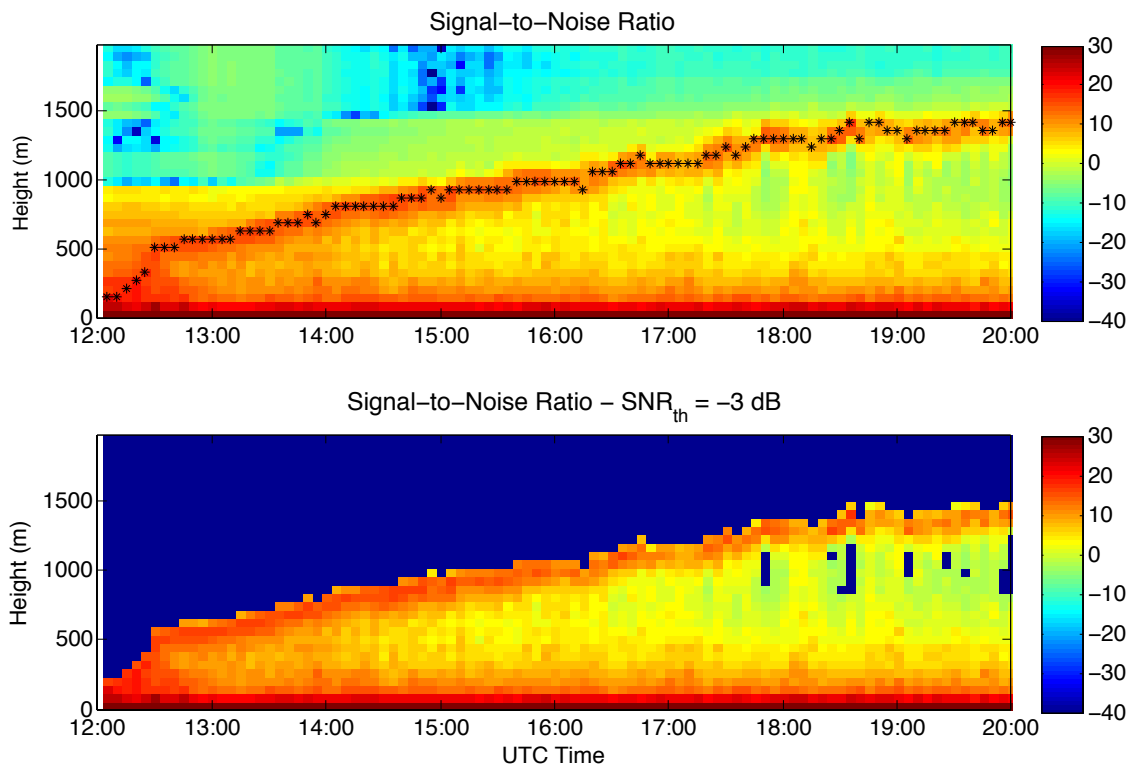


Figure 5.6: Top: Signal-to-Noise Ratio as a function of time. The asterisks represent estimates of the BL top. Bottom: censored SNR plot. Values less than -3 dB and above the BL top have been removed.

Third, the DBS technique is used to retrieve the three wind components. Finally, the wind components are averaged over 5 min. The LES data are averaged in time to obtain the 5-min (*revisit time*) estimates used for comparison. Estimates from SA are calculated every 150 s (DBS scan time) and are averaged over the same 5-min period.

Zonal and meridional wind estimates plots for  $sfrac = 1$  are presented in Figures 5.7 and 5.8, respectively. In the top panel the “true” wind obtained from the LES is presented. Estimates obtained from the DBS technique are presented in the middle panel. Finally, the bottom panel displays the estimates obtained from SA (FCA-G). The first height is removed for DBS due to corrupted wind estimates; meanwhile, for SA, the three first heights are removed due to the lack of points in the common volume used by the technique.

A comparison between the horizontal wind estimates (zonal and meridional) obtained from DBS are presented versus their corresponding “ideal” values obtained from the LES in Figure 5.9 for different  $sfrac$  values. The measured wind estimates exhibit good agreement with their corresponding values from LES. However, as the  $sfrac$  increases, the bias of the estimates increases. The effect of this increase in bias is observed as a spread in the wind estimates for both horizontal components. The maximum spread is observed when  $sfrac = 1$ , and its minimum when  $sfrac = 0$ . As previously studied, the main cause of this bias error is the horizontal shear of vertical velocity. In realistic measurements, it is impossible to separate this effect from the real wind estimates and/or to evaluate this quantity.

The range corrected shear, or ideal bias, is calculated from the LES fields in the same fashion as described in Section 5.1.1.1. Presented in the middle-top and bottom panels of Figure 5.10 are the ideal biases for the case when  $sfrac = 1$  for the zonal and meridional components, respectively. The calculations have been made at each height and along the whole simulation time. The ideal bias has low values at the beginning of the simulation. The top and middle-bottom panels represent the measured bias from the wind estimates obtained from the radar measurements. The plot shows a good correlation between the bias error in the zonal and meridional estimates, and the bias caused by the horizontal shear of vertical velocity calculated from the LES wind fields. However, there is an overestimation of the wind in certain areas. This overestimation might be caused by inhomogeneities within the volume that encloses the five DBS beams (Cheong et al. 2008).

For better comparison, the ideal bias error is compared in a scatter plot with the range corrected shear for each horizontal wind component in Figure 5.11. The

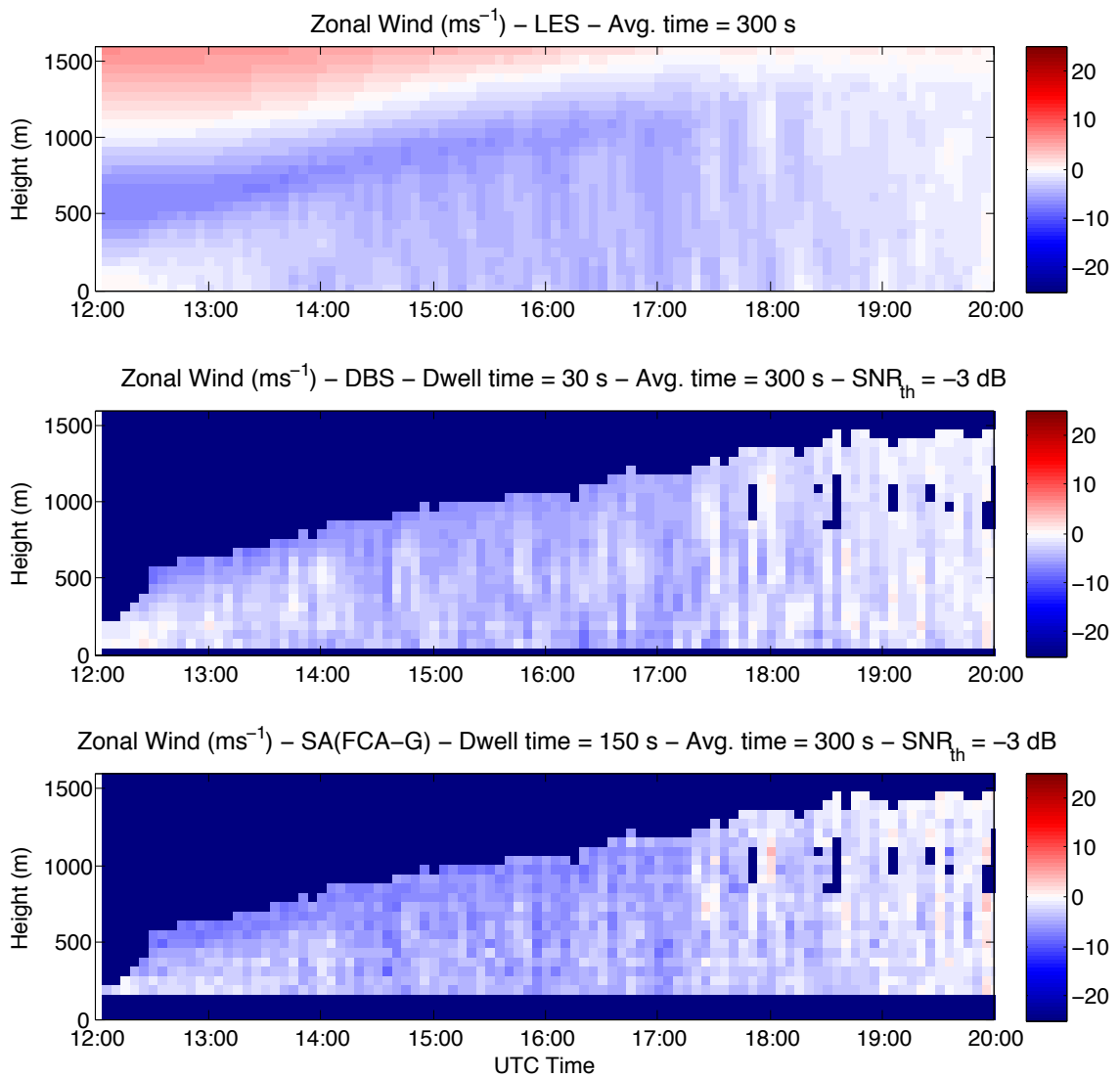


Figure 5.7: Zonal wind estimates as a function of time for  $sfrac = 1.00$ . Top: LES estimates. Middle: DBS estimates. Bottom: SA estimates obtained from the FCA-Gaussian method. The first height is removed for DBS, and the first three heights for SA.

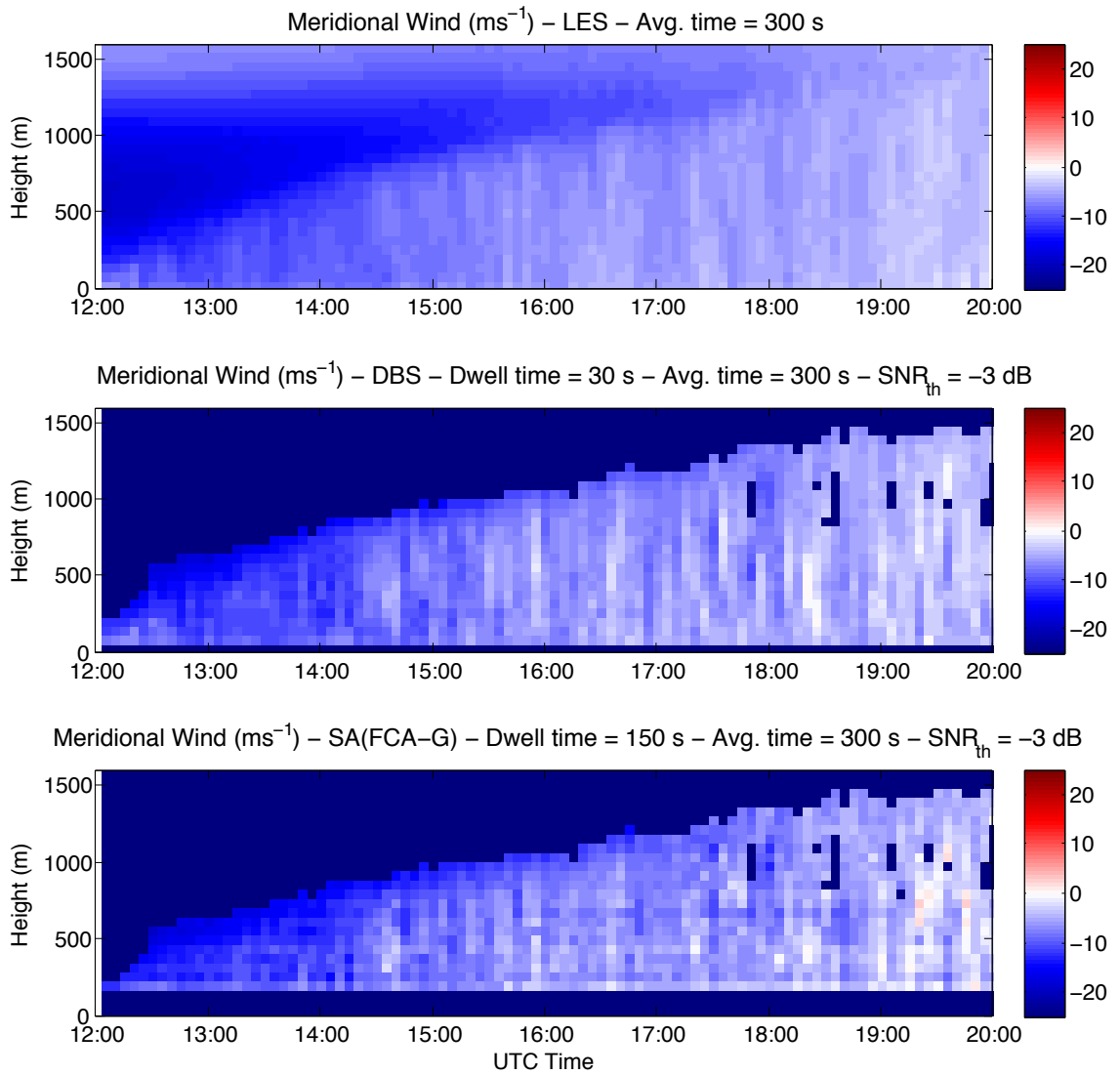


Figure 5.8: Same as Figure 5.7, except for the meridional wind.

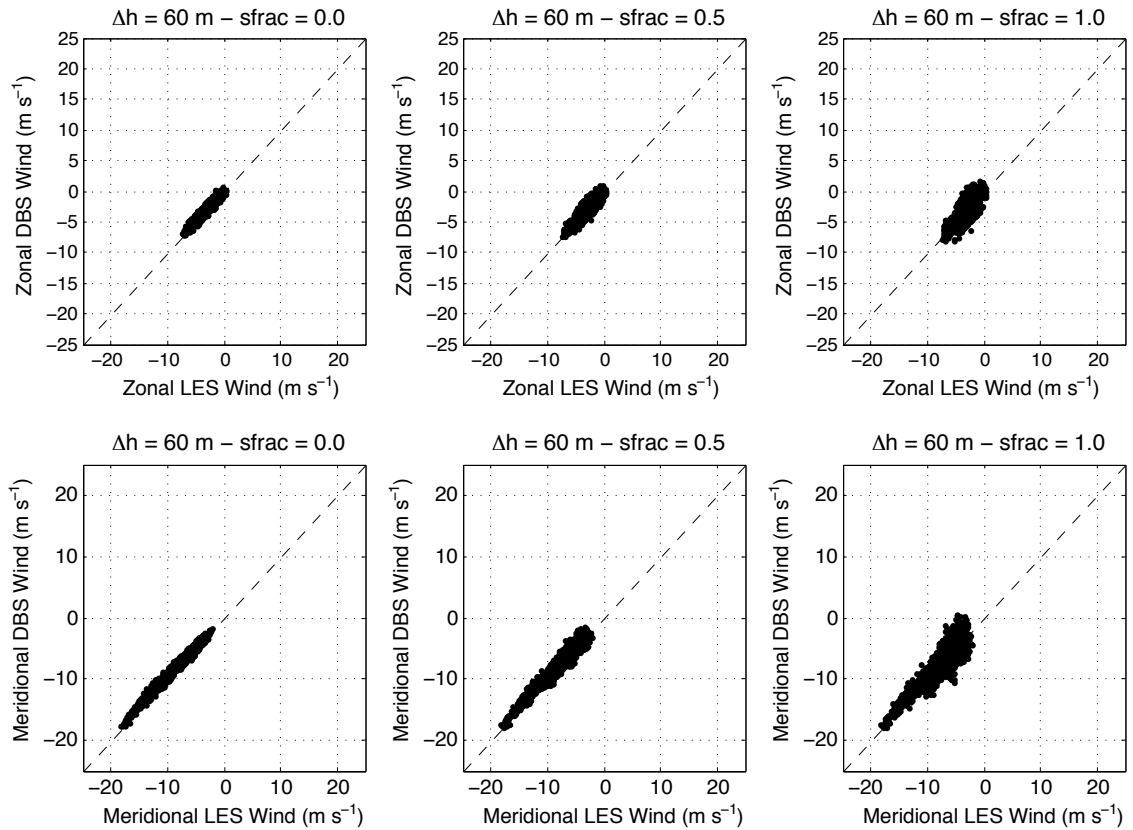


Figure 5.9: Comparison between the DBS estimates versus LES fields. Top: zonal wind for different  $sfrac$  values. Bottom: meridional wind for the same  $sfrac$  values. Left:  $sfrac = 0.00$ . Middle:  $sfrac = 0.50$ . Right :  $sfrac = 1.00$ .

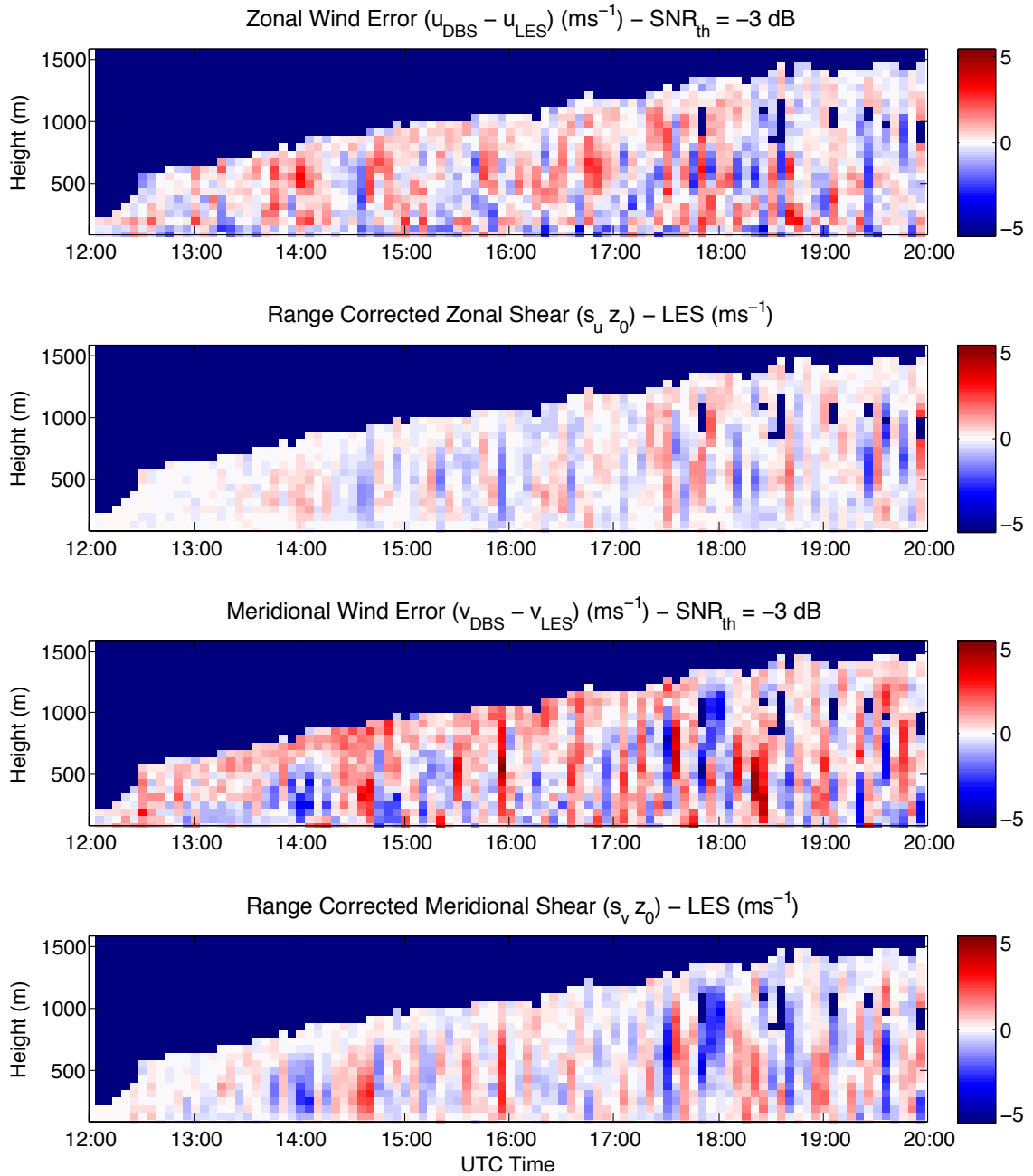


Figure 5.10: Error analysis as a function of time for  $sfrac = 1$ . Top: zonal wind error from DBS estimates. Middle-top: range corrected zonal shear from LES. Middle-bottom: meridional wind error from DBS estimates. Bottom: range corrected meridional shear from LES.

region after the censoring corresponds to the CBL, where strong updrafts and mild downdrafts are present. Consequently, the zone is more susceptible to the horizontal shear of vertical velocity effect. The correlation for zonal wind is 0.36. Meanwhile, for the meridional wind is 0.66, which indicates the presence of other factors that can cause an error in the wind estimates that cannot be attributed to the vertical velocity shear, such as the horizontal wind shear especially observed in the LES zonal wind.

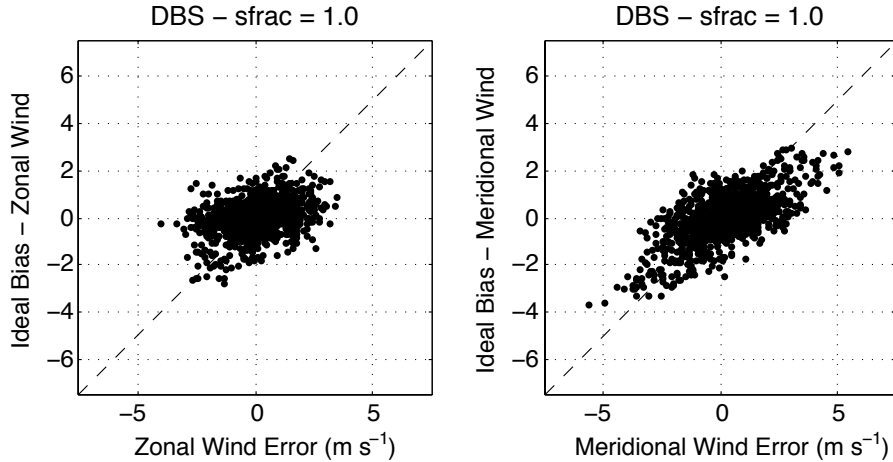


Figure 5.11: Error from the DBS estimates vs. range corrected shear from LES for  $sfrac = 1.00$ . Left: zonal wind. Right: meridional wind.

As in the theoretical analysis, the cumulative measured bias as a function of  $sfrac$  is presented in Figure 5.12. Notice that when  $sfrac = 0$ , the measured bias is different than zero (theoretical value). This is another indication that there are other factors that contribute to the error in the wind estimates. However, the theoretical tendency of the bias increases as the  $sfrac$  does, and it is observed in both wind components.

As in the case of DBS, the bias error is analyzed for the SA technique. The comparison between the zonal and meridional wind estimates from SA and LES are presented in Figure 5.13. Again, it can be observed that as the  $sfrac$  increases, the bias in the measured wind estimates also increases. Here, the estimates are more variable than for DBS, especially in the zonal wind.

The theoretical shear is presented in Figure 5.14 for the zonal (middle-top) and meridional (bottom) wind components. Again, there is a correlation between the bias error and the horizontal shear of vertical velocity. Nevertheless, there are discrepancies that need further analysis.

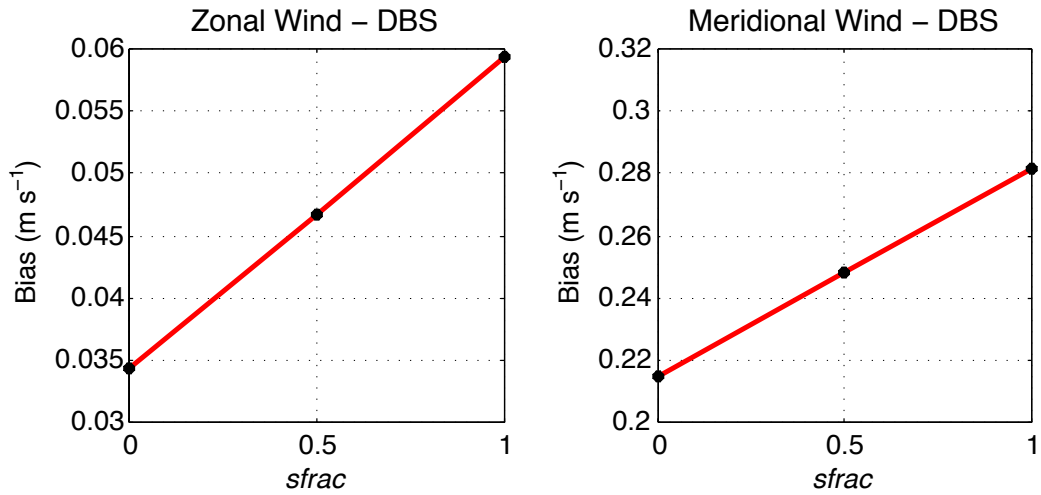


Figure 5.12: Wind bias for DBS. Left: zonal wind. Right : meridional wind.

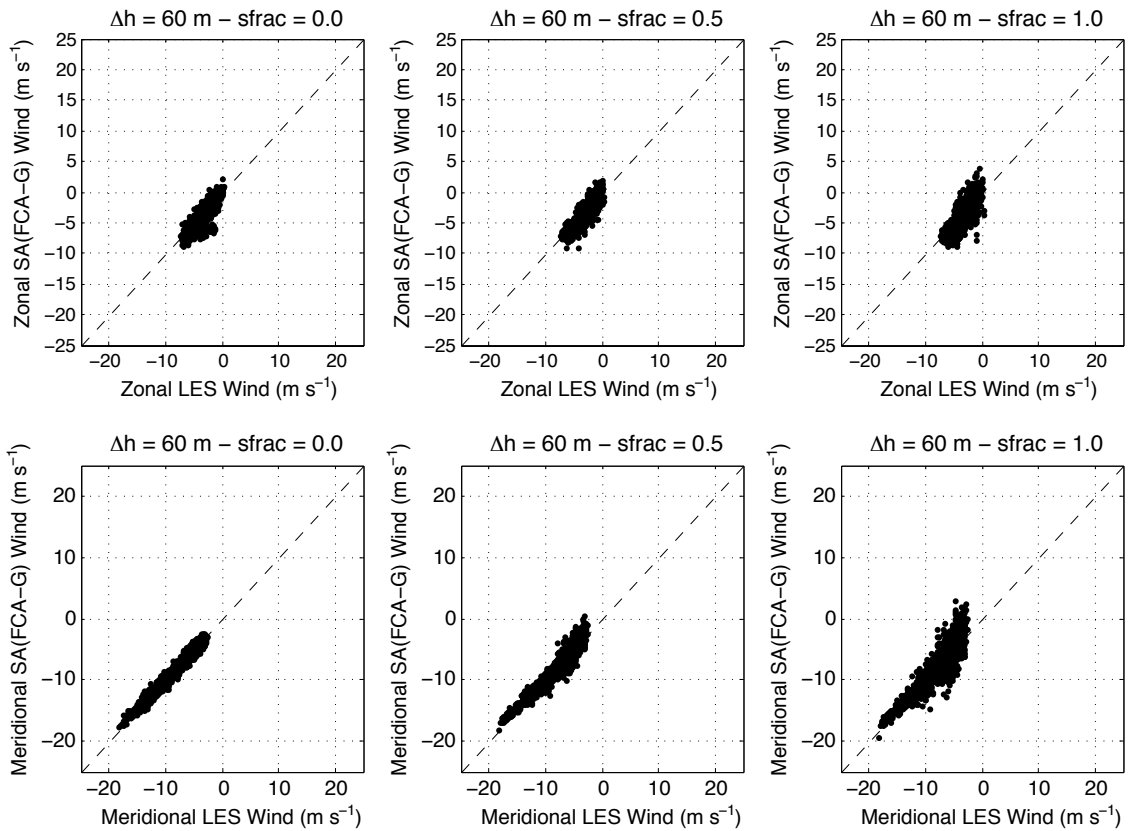


Figure 5.13: Comparison between the SA estimates vs. LES fields. Top: zonal wind for different *sfrac* values. Bottom: meridional wind for the same *sfrac* values. Left: *sfrac* = 0.00. Middle: *sfrac* = 0.50. Right : *sfrac* = 1.00.

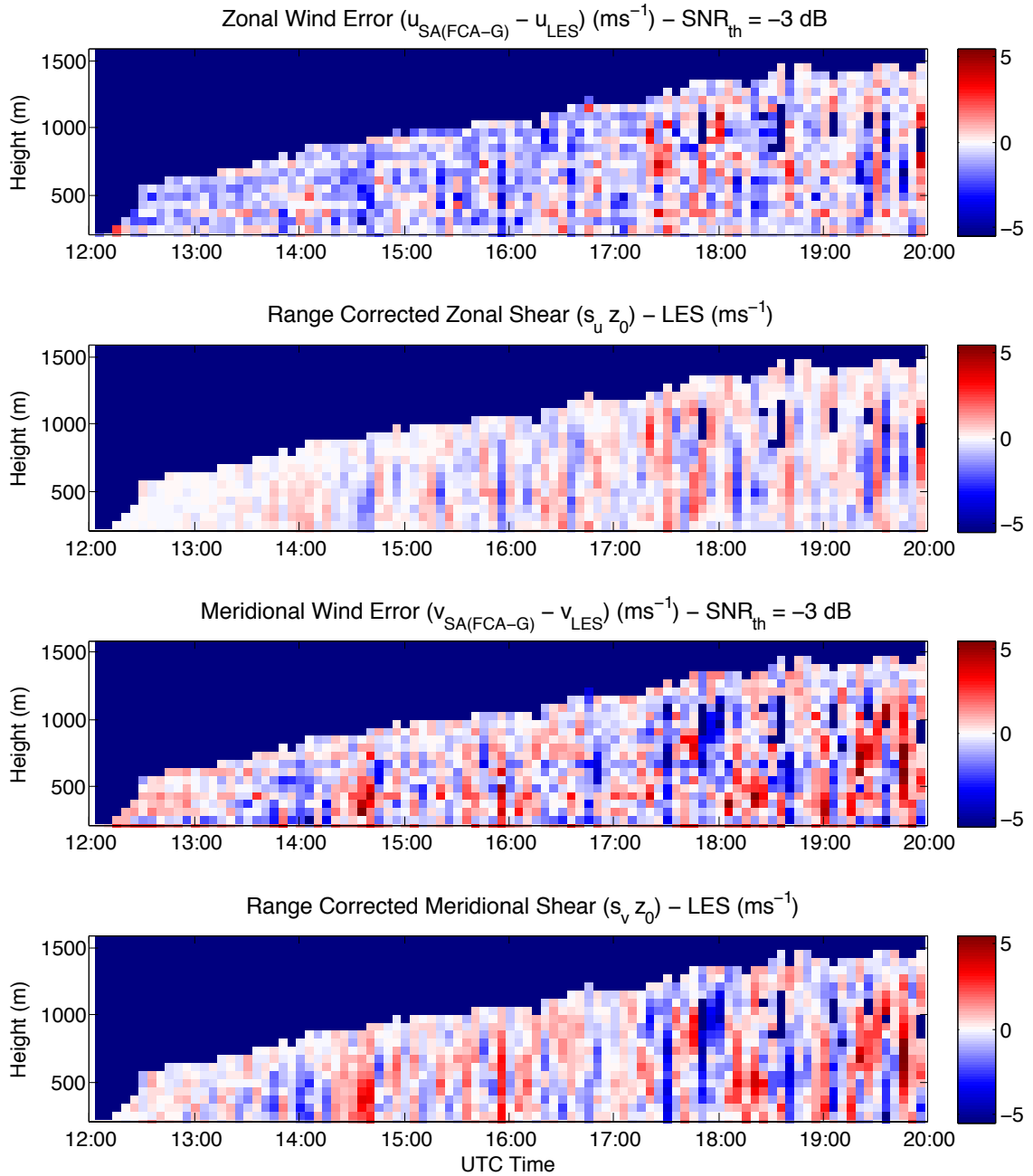


Figure 5.14: Error analysis as a function of time for  $sfrac = 1$ . Top: zonal wind error from SA estimates. Middle-top: range corrected zonal shear from LES. Middle-bottom: meridional wind error from DBS estimates. Bottom: range corrected meridional shear from LES.

The ideal bias error and the measured range corrected shear are presented as a scatter plot for  $sfrac = 1$  in Figure 5.15. There is good correlation between both quantities. However, in contrast to what was presented for DBS (see Figure 5.11), the correlation for both horizontal wind components has improved. That is, the correlation for zonal and meridional winds are 0.66 and 0.79, respectively. Probably, because the scan volume for SA is smaller than for DBS.

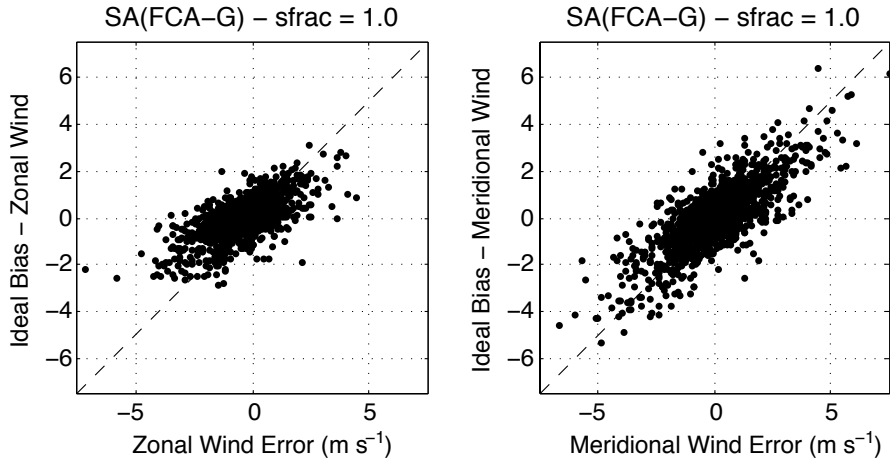


Figure 5.15: Error from the SA estimates vs. range corrected shear from LES for  $sfrac = 1.00$ . Left: zonal wind. Right: meridional wind.

Finally, the cumulative measured bias error as function of  $sfrac$  is presented in Figure 5.16. As observed for DBS (see Figure 5.12), there is a bias different than zero for  $sfrac = 0$ , which indicates the presence of other factors contributing to the measured bias. Also, their increase as a function of  $sfrac$  is also observed. However, they are not as well aligned as in the case of DBS.

In realistic radar setups, the horizontal shear caused by vertical velocity cannot be separated from the horizontal wind estimates, and depending on the level of activity of the CBL, it can considerably bias their estimates (Flowers et al. 1994; Zhang and Doviak 2007). From the results shown for both techniques when  $sfrac = 0$ , it can be inferred that this is not the only cause that generated bias in the wind estimates. Other might include estimation errors, and/or horizontal wind shear, etc.

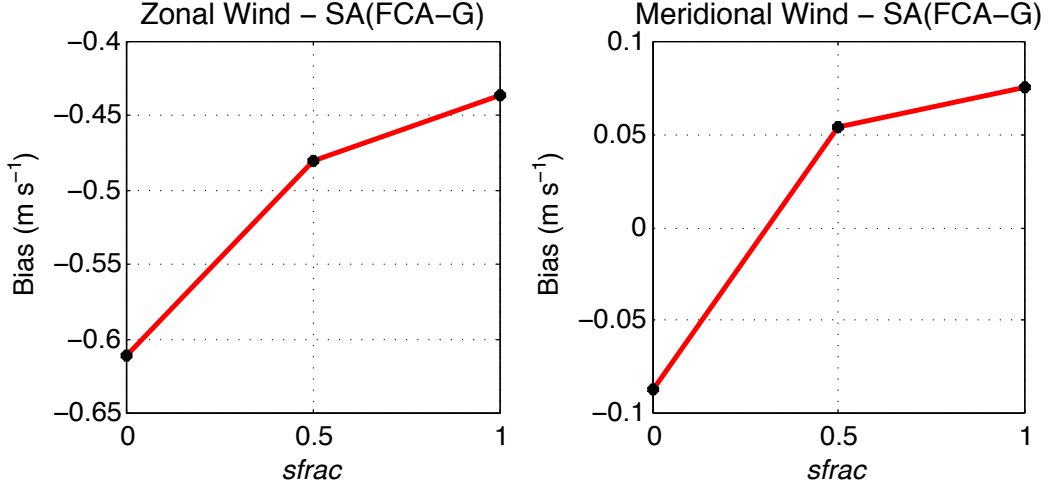


Figure 5.16: Wind bias for SA. Left: zonal wind. Right: meridional wind.

## 5.2 Turbulence Kinetic Energy Based on Radar Wind Estimates

### 5.2.1 Theoretical Formulation

Turbulence kinetic energy (TKE) estimates have been calculated from both LES and virtual BLR data using a variety of averaging approaches. The reference TKE values have been obtained from LES data by horizontal plane averages over the entire sub-domain as:

$$\sigma_u^2(LES) = \overline{u'u'} + \frac{2}{3}\overline{E}, \quad (5.9)$$

$$\sigma_v^2(LES) = \overline{v'v'} + \frac{2}{3}\overline{E}, \quad (5.10)$$

$$\sigma_w^2(LES) = \overline{w'w'} + \frac{2}{3}\overline{E} \quad (5.11)$$

$$TKE_{LES} = \frac{1}{2} (\sigma_u^2 + \sigma_v^2 + \sigma_w^2), \quad (5.12)$$

where  $u'$ ,  $v'$ , and  $w'$ , respectively, are the zonal-, meridional-, and vertical- velocity fluctuations against the corresponding plane means,  $E$  is sub-grid TKE, and the over-bars represent the horizontal plane averaging. To enable comparisons with the BLR statistics, the TKE estimates from LES are additionally averaged in time over a one-hour period.

Another TKE estimate is obtained from the LES velocity fields first averaged in space over a cross-section that encloses five DBS beams for each LES time step. The

resulting time series of velocity is then used to estimate TKE by temporal averaging over a period of one hour. The employed expressions for statistics in this case are analogous to Equations (5.9) to (5.12), where the over-bars would now specify temporal averaging and primes which denote a deviation from temporal means. The optimal averaging period is investigated empirically.

Estimates of TKE obtained from the virtual BLR in the DBS mode are calculated from velocity fluctuations as functions of time within the DBS volume sampled over the same period of time (one hour):

$$\sigma_u^2(Radar) = \overline{u'u'}, \quad (5.13)$$

$$\sigma_v^2(Radar) = \overline{v'v'}, \quad (5.14)$$

$$\sigma_w^2(Radar) = \overline{w'w'}, \quad (5.15)$$

$$TKE_{Radars} = \frac{1}{2} (\sigma_u^2 + \sigma_v^2 + \sigma_w^2), \quad (5.16)$$

where the over-bars represent temporal averaging in this case.

## 5.2.2 Results

Estimates of TKE from the virtual BLR with two DBS settings are considered. In the ideal setting (DBS ideal), the velocity readings from individual beams are assumed to be available at the same time. In the realistic setting (DBS real), data from individual beams are available sequentially every 30 s so that the wind estimates are calculated after the *scan time* period (150 s) is completed.

All considered methods of the TKE evaluation have been analyzed accordingly. The horizontal wind variances from LES and BLR which are obtained from different averaging techniques are presented in Figure 5.17. The estimates over the DBS domain represent a smaller velocity field sample as compared to the hour-long sample of the velocity field from the LES within the whole BLR sub-domain. Only the statistics obtained by plane averaging show that they are variable in time. The spread of plane statistics over one-hour time period is demonstrated by gray lines in Figure 5.17. Both the estimates from the ideal and realistic DBS settings overestimate the horizontal velocity variance. DBS estimates from the ideal configuration are consistently smaller than the estimates from realistic settings.

After careful analysis, the overestimation of the TKE for horizontal components by the DBS technique are attributed to the horizontal shear of vertical velocity effect (see Section 5.1), which generates a bias in the horizontal wind estimates. The shear

effect in these estimates can be easily removed by setting the vertical velocity to zero ( $sfrac = 0$ ). Once it has been removed, the BLR estimates of TKE are in better agreement with the LES horizontal velocity variance data.

A longer averaging time for the DBS signal (1200 s instead of 150 s) reduces the effect of the vertical velocity variability on the retrieved horizontal wind variances. The corresponding variance estimates are presented in Figure 5.18. However, the number of points used in the calculations of the horizontal variance has been reduced from 24 (for 150 s) to 3 (for 1200 s). This reduction in the number of points, although they provide better agreement with the LES estimates, is not appropriate for variance calculations.

Estimates of the vertical velocity variances are presented in the left panel of Figure 5.19 for the same cases that have been analyzed with respect to the horizontal velocity variances. The discrepancies among the estimates are due to the differences in the spatial and temporal dimensions of the vertical velocity samples. Same effect was observed in Section 4.4, where the sampling time of the vertical velocities was set to  $\sim 6$  min to replicate the radar *revisit time*. The velocity variances calculated from the LES across the DBS volume scan over a one-hour time period agree reasonably well with estimates from the DBS in ideal and realistic settings.

Finally, the estimated values of all three flow components (zonal, meridional, and vertical) variances are brought together to obtain TKE estimates. The horizontal velocity variances from the DBS are computed with 1200 s averaging applied. The vertical component variances are evaluated with the maximum sampling time. The results are presented in right panel of Figure 5.19. Remarkably, the DBS estimates from the realistic setting are rather close to the LES estimates calculated over the DBS volume with one-hour averaging.

## 5.3 Turbulence-Eddy Dissipation Rate Based on Radar Spectrum Width

### 5.3.1 Theoretical Formulation

The TKE (eddy) dissipation rate  $\epsilon$  is commonly estimated from the Doppler spectrum width  $\sigma_v$  of the radar signal when the outer scale in the inertial subrange is at least three times greater than the scale of the radar's resolution volume (Istok and Doviak 1986; Doviak and Zrnić 1993). As indicated in White (1997); Jacoby-Koaly

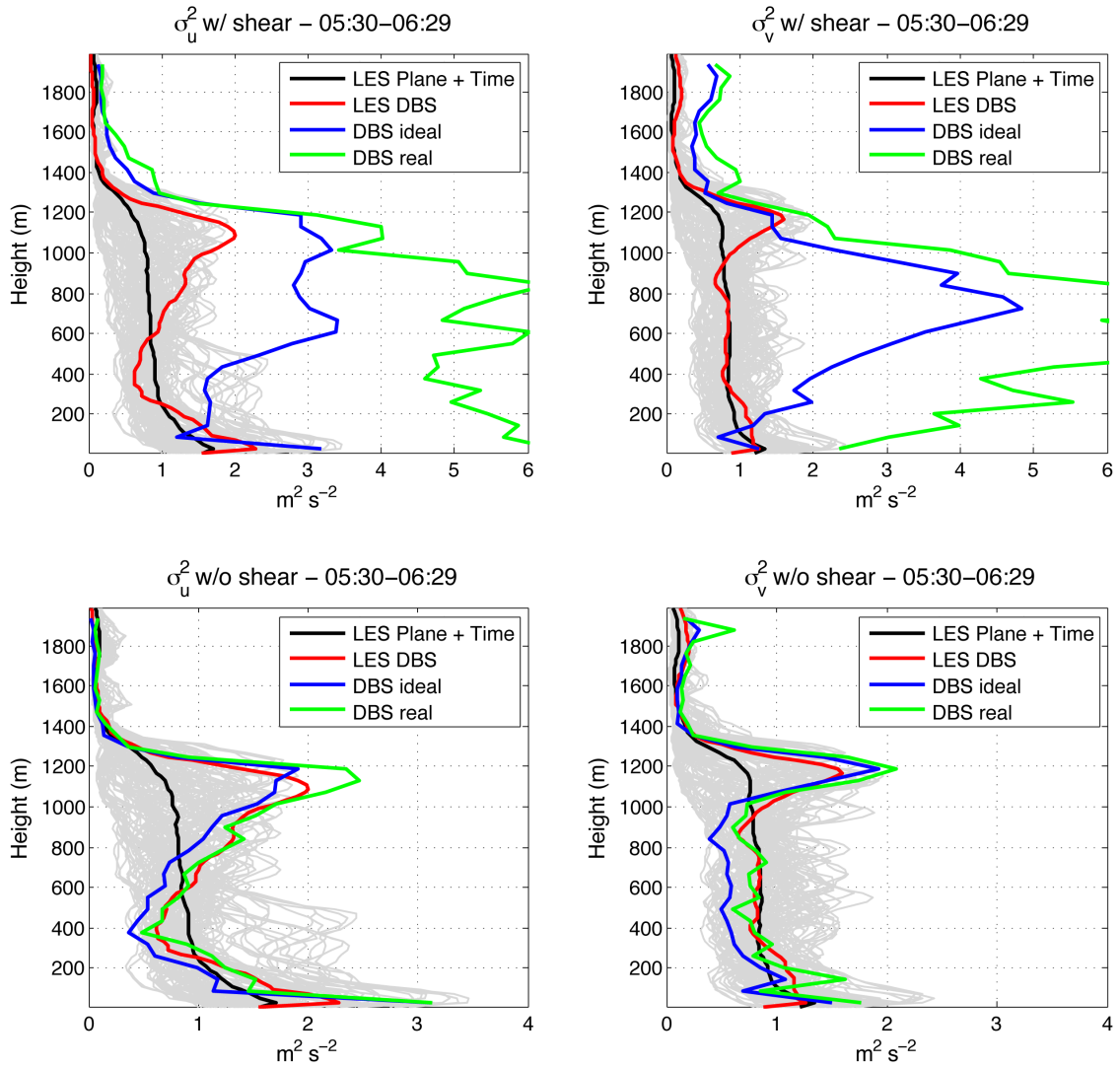


Figure 5.17: Horizontal velocity variances. Gray lines: time spread of plane statistic estimates from the LES over a one-hour period. Black: statistics obtained from LES data over the entire BLR domain by plane averaging and additional time averaging over one hour. Red: velocity variances calculated by time averaging from LES data over the DBS volume scan. Blue: velocity variance estimated from an ideal DBS setting (all beams available at dwell time of 30 s). Green: velocity variance estimated from a realistic DBS setting (all beams available after the scan time of 150 s). Statistics in the two upper plots are evaluated with original vertical velocities ( $sfrac = 1$ ). Statistics in the two lower plots are obtained with zero vertical velocity ( $sfrac = 0$ ).

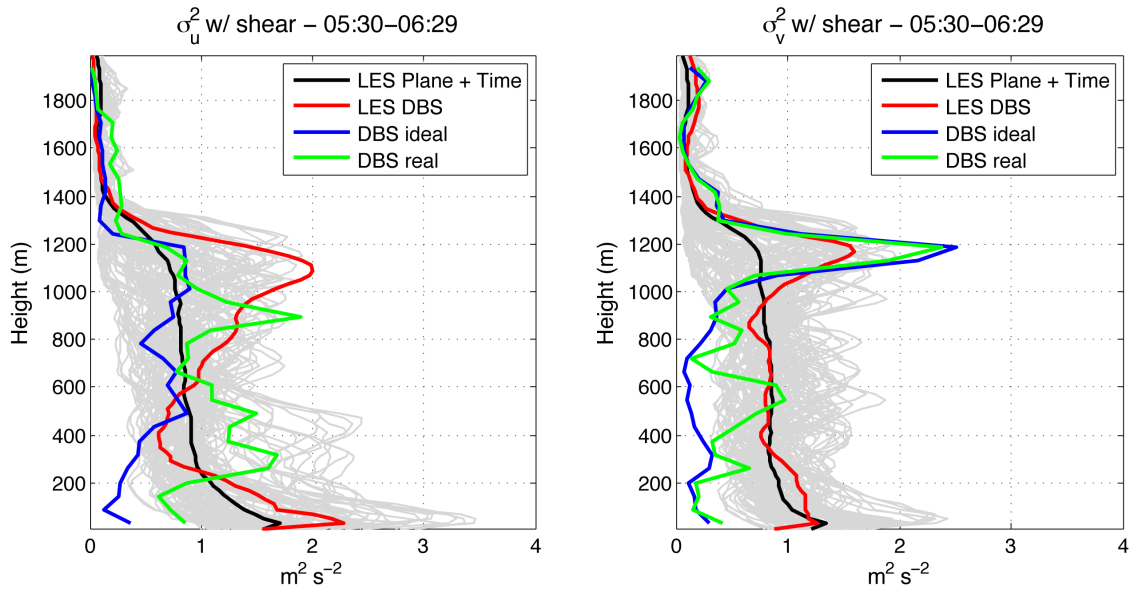


Figure 5.18: Horizontal velocity variances. For notation see Figure 5.17. The averaging time for the DBS estimates is 1200 s instead of 150 s.

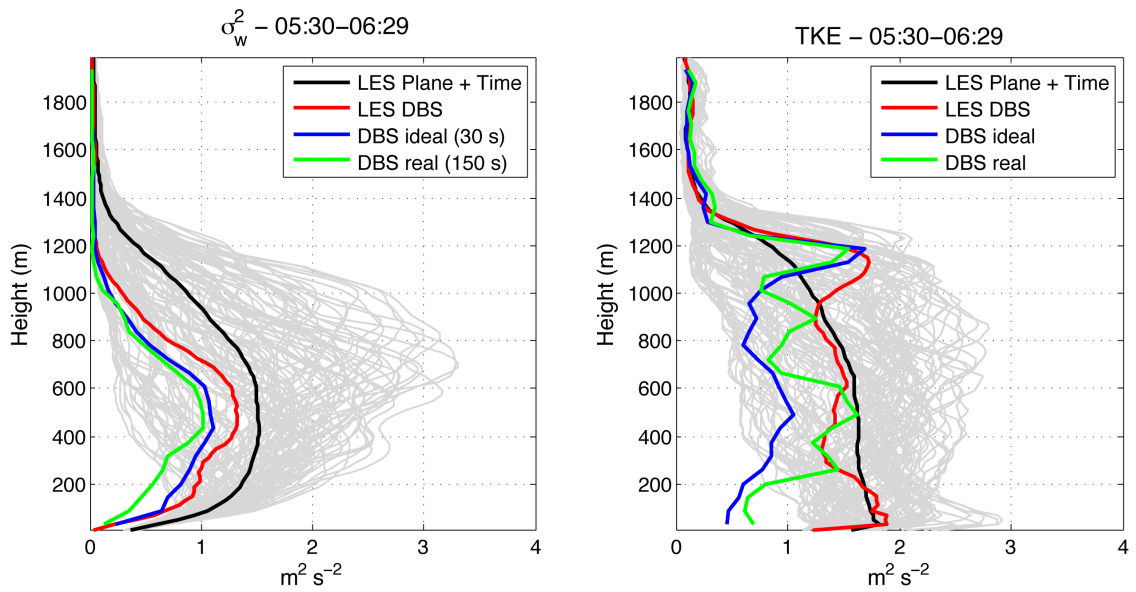


Figure 5.19: Left: vertical velocity variance. Right: turbulence kinetic energy. For notation see Figure 5.17.

et al. (2002); Scipi3n et al. (2009), the spectral broadening is caused by spatial and temporal variations of radial velocity within the resolution volume. As mentioned in Section 2.3.1.2, the square of the spectrum width can be expressed as the sum of at least three different contributions (Doviak and Zrni3c 1984; Doviak and Zrni3c 1993):

$$\sigma_v^2 = \sigma_{11}^2 + \sigma_s^2 + \sigma_x^2, \quad (5.17)$$

where  $\sigma_{11}$  represents broadening due to turbulence,  $\sigma_s$  represents the shear broadening due to large-scale (larger than the radar resolution volume) variations of the wind field, and  $\sigma_x$  represents other contributions that can be attributed to signal processing inaccuracies.

As discussed in White (1997), Jacoby-Koaly et al. (2002), and Scipi3n et al. (2009), the shear broadening effect for a vertical pointing beam is primarily determined by beam broadening. It may be represented as:

$$\sigma_s^2 = \sigma_a^2 \times V_H^2, \quad (5.18)$$

$$\sigma_a = \frac{\theta_1}{4\sqrt{\ln 2}}, \quad (5.19)$$

where  $V_H$  is the horizontal wind magnitude.

For a case corresponding to oblique beams, and under the assumptions of narrow beams, constant wind shear, and separable beam illumination, Doviak and Zrni3c (1984) and Jacoby-Koaly et al. (2002) recommend expressing the shear broadening effect as:

$$\sigma_s^2 = (a_1 k_\theta)^2 + (a_2 k_\phi)^2 + (b k_r)^2, \quad (5.20)$$

where  $k_\theta$ ,  $k_\phi$ , and  $k_r$  represent the components of the wind shear in the spherical coordinates. Under the additional assumption of a circularly symmetric Gaussian beam pattern,  $a_1$  and  $a_2$  have the same value  $a = \sigma_a r$ , which is a function of range and beamwidth. Finally,

$$a k_\phi = \sigma_a \left[ \left( \frac{\partial u}{\partial z} \sin \theta + \frac{\partial v}{\partial z} \cos \theta \right) r_0 \cos^2 \phi - u \sin \theta \sin \phi - v \cos \theta \sin \phi + \frac{\partial w}{\partial z} r_0 \cos \phi \sin \phi + w \cos \phi \right], \quad (5.21)$$

$$a k_\theta = \sigma_a (u \cos \theta - v \sin \theta), \quad (5.22)$$

$$b k_r = b \left[ \left( \frac{\partial u}{\partial z} \sin \theta + \frac{\partial v}{\partial z} \cos \theta \right) \cos \phi \sin \phi + \frac{\partial w}{\partial z} \sin^2 \phi \right], \quad (5.23)$$

where  $b$  is related to the pulse width as  $b = 0.3\Delta r$ .

Following Scipi3n et al. (2009), the windowing effect is considered the only signal processing effect that broadens the estimated spectrum. This contribution is generally constant and is easily calculated from the Fourier transform of the window used in the processing (3-dB spectrum width).

After removing all the external effects, the value of  $\sigma_{11}$  can be employed to estimate the turbulence eddy dissipation rate  $\epsilon$ . Under the assumptions of homogeneity and isotropy, and Gaussianity of the beam and range weighting functions, the turbulence broadening contribution  $\sigma_{11}^2$  may be related to the dissipation rate  $\epsilon$  by Equation (5.32) from White (1997). After converting to spherical coordinates and approximating  $\text{sinc}^2(x)$  with  $\exp(-x^2/3)$  (the approximation has a margin of error of 2%), White et al. (1999) obtains a more manageable expression for  $\epsilon$ , namely:

$$\epsilon_{Rad} = \sigma_{11}^3 (4\pi/A_e)^{3/2} J^{-3/2}, \quad (5.24)$$

$$J = 12\Gamma(2/3) \int_0^{\pi/2} \int_0^{\pi/2} (\sin^3 \varphi)(b^2 \cos^2 \varphi + a^2 \sin^2 \varphi) \quad (5.25)$$

$$+ (L^2/12) \sin^2 \varphi \cos^2 \phi)^{1/3} d\varphi d\phi,$$

$$L = V_T t_D, \quad (5.26)$$

where  $\Gamma$  is the Gamma function,  $V_T$  is the wind speed transversal to the radar beam, and  $t_D$  is the radar dwell-time (White 1997). The parameter  $A_e = 1.6$  is related to the empirical constant in the inertial subrange of the velocity spectrum. Note that  $\epsilon$  is proportional to the cube of  $\sigma_{11}$ . This implies that the TKE dissipation rate in the considered formulation is quite sensitive to variations of  $\sigma_{11}$ .

The best way to obtain  $\epsilon$  from LES data is to use the parameterized expression that enters the LES prognostic equation for the sub-grid kinetic energy (Deardorff 1980) as presented in Equations (2.9) to (2.11).

### 5.3.2 Results

The energy spectrum of turbulence  $E(\kappa)$  was estimated from the LES velocity fields at approximately 700 m following the procedure described in Kaiser and Fedorovich (1998). The average longitudinal and transverse spectra obtained between 18:00 - 19:00 UTC are presented in Figure 5.20. However, due to the limited number of points of the LES sub-domain used in the radar simulator, it is impossible to determine the outer scale of the inertial subrange  $\Lambda$  from the estimated spectrum. Nevertheless, its

scale is greater than 1400 m, which corresponds to the maximum scale resolvable by the spectrum.

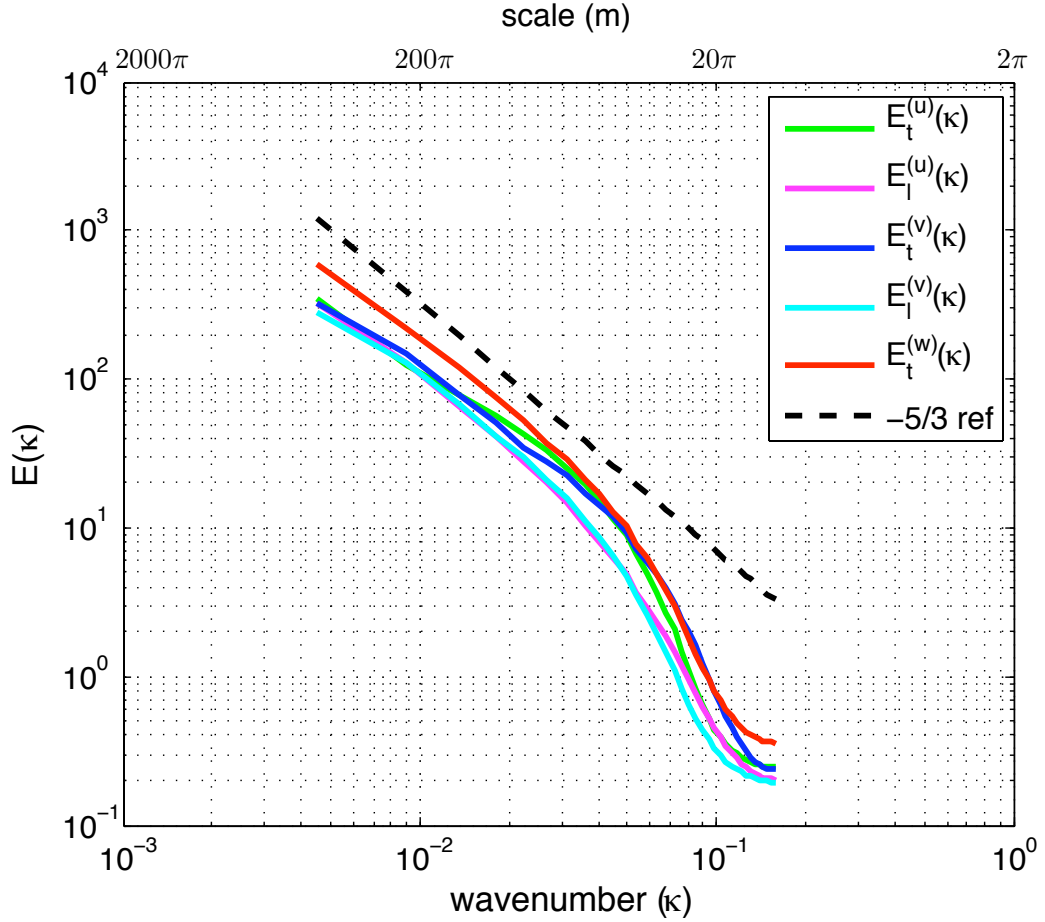


Figure 5.20: Kolmogorov turbulence spectra obtained from the velocity fields. The subscript represents the longitudinal  $l$  or the transverse  $t$  component, and the superscript represents the velocity component. All five components are presented as a time average obtained between 18:00-19:00 UTC at approximately 700 m. The black dashed line represents the  $-5/3$  law expected from isotropic turbulence (see Section 2.2.3.2). All spectra behave similarly, which confirms the isotropy in the LES fields. Also, the transverse spectrum is larger than the longitudinal spectrum, which is consistent with the structure parameter in the inertial subrange. The beginning of the dissipation range can be identified as  $\approx 157$  m, which is caused by dumping in the sub-grid closure of the LES model.

The scale of the resolution volume is defined as (Istok and Doviak 1986):

$$\Lambda_6 = r_{max}\theta_1, \quad (5.27)$$

where  $r_{max} = 2$  km is the maximum vertical range available from the LES. Therefore, for the virtual BLR with  $\theta_1 = 9^\circ$ , the resulting  $\Lambda_6 \approx 220$  m is less than one third of the outer scale of the inertial subrange. In the BLR simulation, the eddy dissipation rate has been obtained for all five DBS beams (4 oblique and 1 vertical) without censoring and for the whole run of the simulation (approximately 11.5 hrs). The obtained estimates are compared with the  $\epsilon$  estimates from LES. The estimates are presented in Figure 5.21. Qualitatively, all estimates look similar; however, a more in-depth analysis is needed to quantify the observed differences.

Hourly averaged profiles of  $\epsilon$  from the BLR are presented in Figures 5.22 through 5.25 for four time periods: 16:00-17:00, 17:00-18:00, 18:00-19:00, and 19:00-20:00. In the left-hand plots, the radar estimates for different beams are presented in different colors. Different between the estimates for different beams are  $\leq 4 \times 10^{-2} \text{ m}^2 \text{ s}^{-3}$ . This agreement confirms the previous findings of Jacoby-Koaly et al. (2002) and complements their results since their estimates of  $\epsilon$  from the vertical beam were rather poor due to ground-clutter contamination. In the right-hand plots of Figures 5.22 to 5.25, averages from the five beams are compared with the LES estimates of  $\epsilon$ . In general, the radar and LES estimates of dissipation rate agree well, with discrepancies in the mixed layer  $\leq 2 \times 10^{-2} \text{ m}^2 \text{ s}^{-3}$ . The observed discrepancies correspond to heights below  $\sim 100$  m where the radar simulator does not reproduce the spectrum width accurately. Another region of discrepancies is above the CBL top (*free atmosphere*) where the estimates are not reliable because the turbulence levels there are extremely low.

In this chapter, the horizontal shear of vertical velocity effect has been studied in depth. First, the theoretical approach using LES-like fields as an input for the virtual radar simulator proves that it affects both DBS and SA techniques for wind estimations. The theoretical measured bias for the simulated case is in excellent agreement for both techniques. The second approach uses realistic LES fields for 8 hours of simulation. Here, the measured biases are also in good agreement with the theoretical biases estimated at each time and height. However, from scatter plot comparison between the two quantities, the horizontal shear of vertical velocity is not the only factor that contributes to discrepancies observed in the horizontal wind estimates. Other factors might include errors in the wind estimates inherent to each technique, horizontal wind shear, etc. Nevertheless, these factors are not subject of the study in this work.

Also, estimates of TKE have been contrasted and compared for different averaging times. LES and radar horizontal estimates are in excellent agreement when the

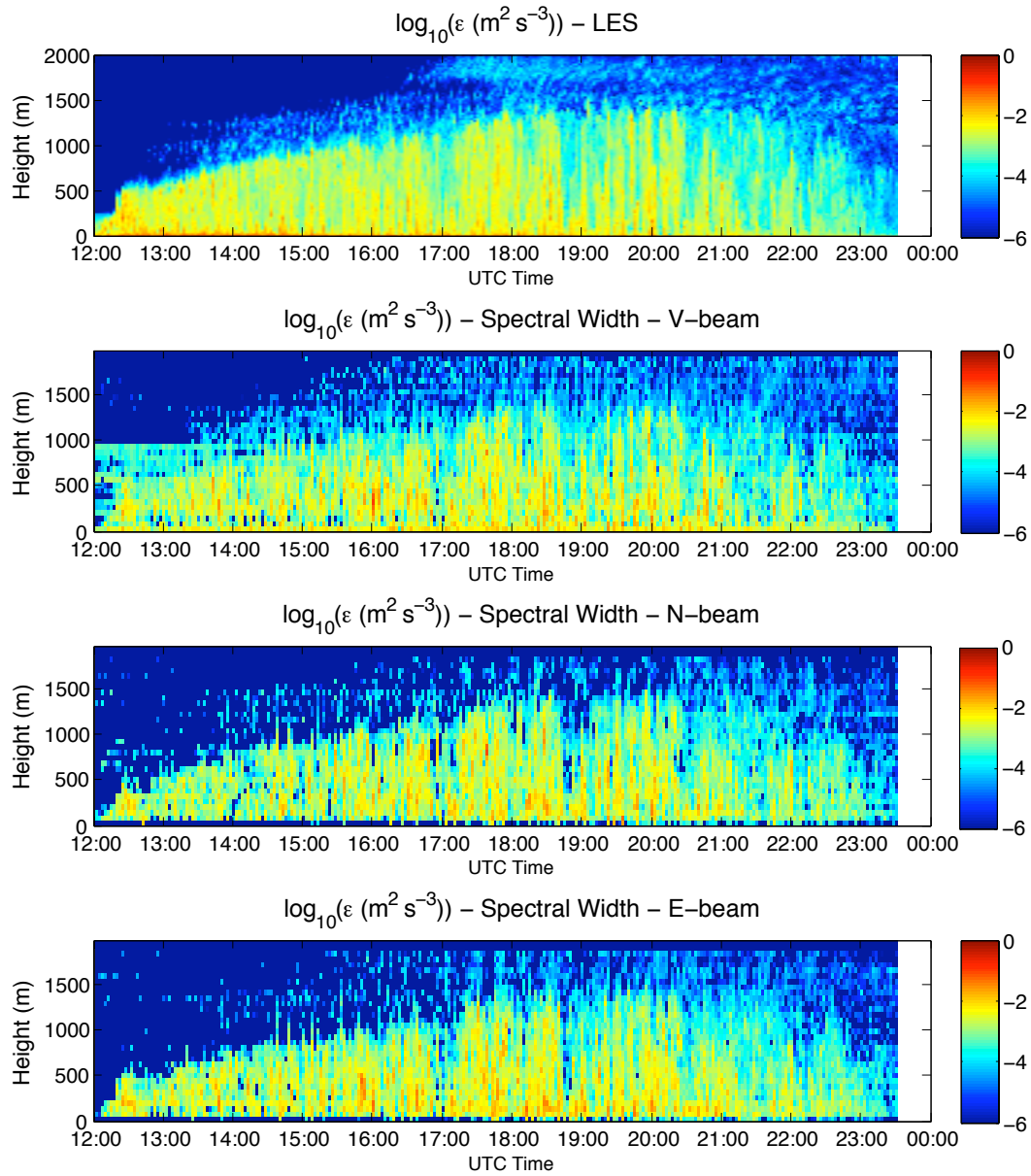


Figure 5.21: Turbulence eddy dissipation rate as a function of time and height. Top: estimates from LES. Middle-top: estimates from the Doppler spectrum width of the signal from the vertical beam. Middle-bottom: estimates from the Doppler spectrum width of the signal from the oblique beam pointing to the north. Bottom: estimates from the Doppler spectrum width of the signal from the oblique beam pointing to the east.

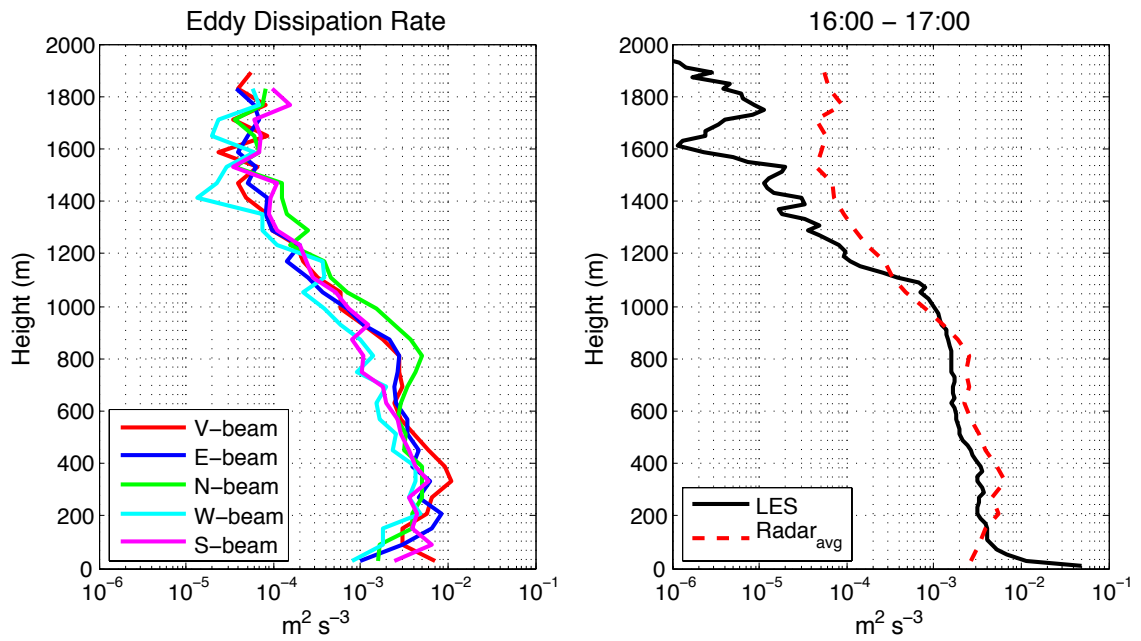


Figure 5.22: Hourly averages of turbulence eddy dissipation rate profiles from 16:00 - 17:00. Left: estimates from the virtual BLR with different directed beams (red: vertical beam; blue: east beam; green: north beam; cyan: west beam; magenta: south beam). Right:  $\epsilon$  profile from the LES (black) compared to the profile from BLR averages among different beam directions (red).

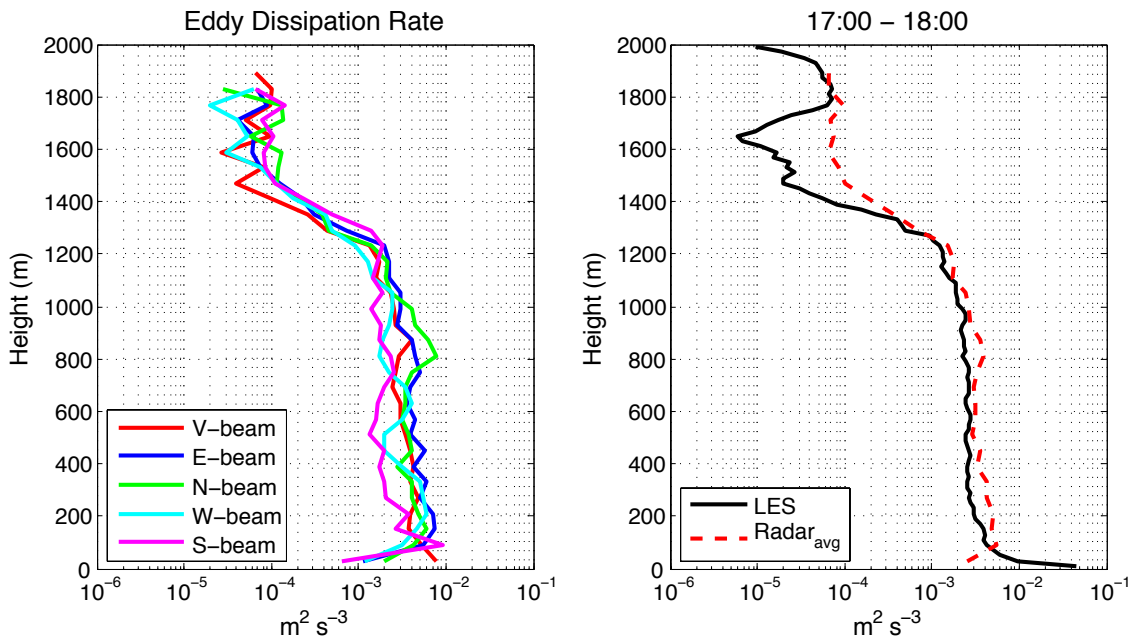


Figure 5.23: Same as Figure 5.22, except with time averaging over period 17:00 - 18:00 UTC.

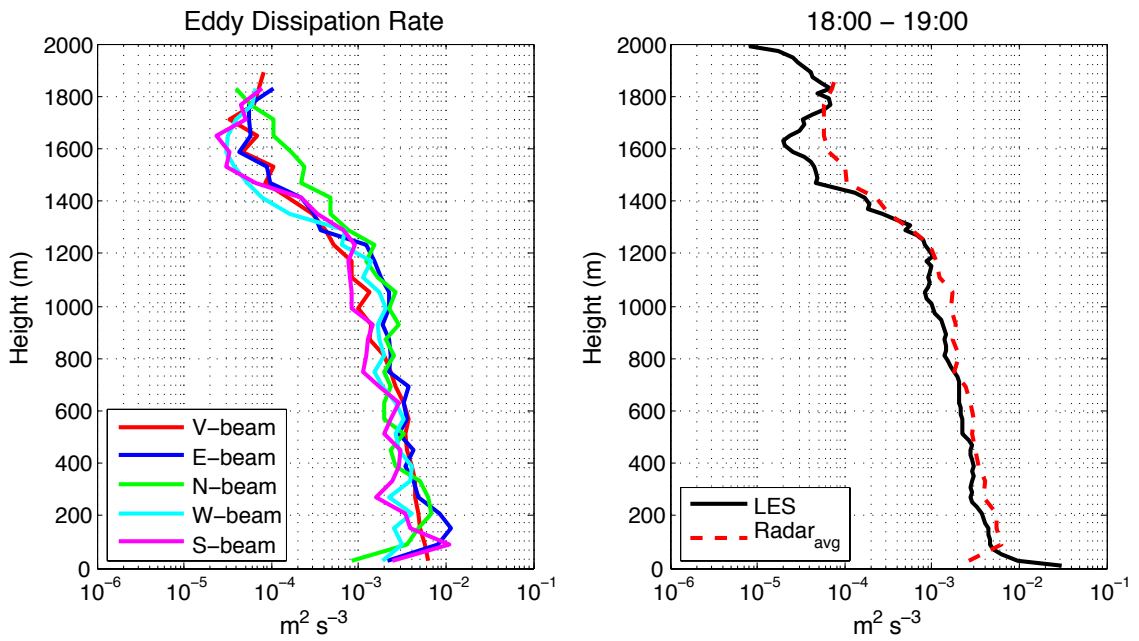


Figure 5.24: Same as Figure 5.22, except with time averaging over period 18:00 - 19:00 UTC.

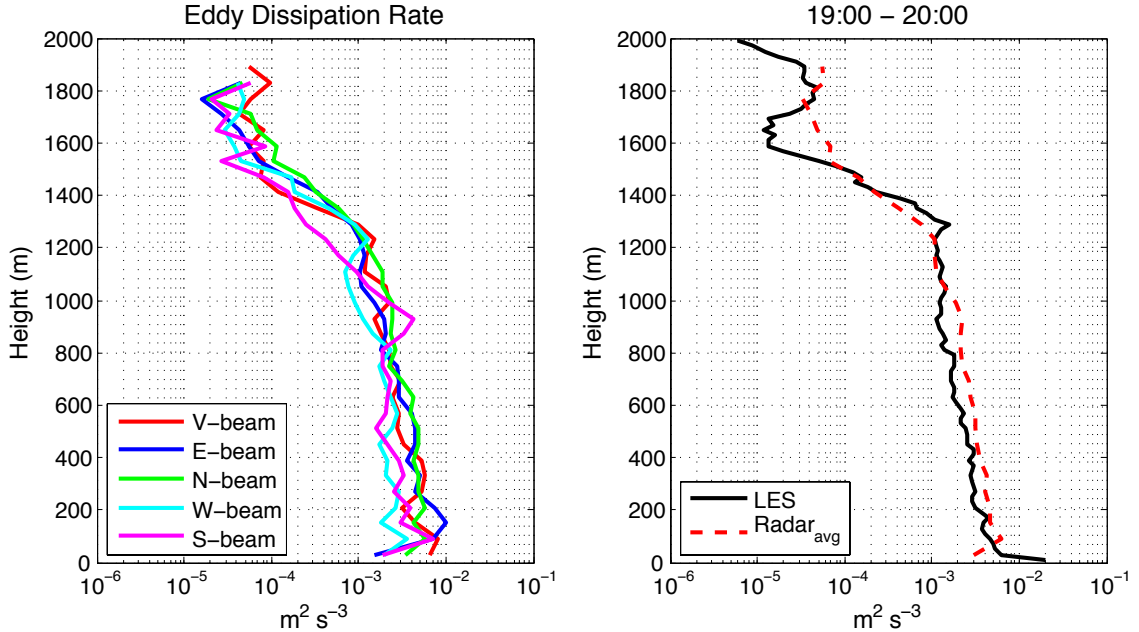


Figure 5.25: Same as Figure 5.22, except with time averaging over period 19:00 - 20:00 UTC.

horizontal shear of vertical velocity effect is not present. When the effect is present, using a long time-average can reduce its effect. Vertical variances have to be calculated using the best time resolution available to avoid filtering the estimates (see Chapter 4).

Finally, TKE (eddy) dissipation rate estimates have been obtained from the radar Doppler spectrum width for all DBS beams. These estimates are in excellent agreement among each other and have been compared with the LES estimates obtained using the Deardorff (1980) closure scheme. Both estimates show similar results, the discrepancies observed at lower heights ( $<100$  m) are due the lack of points in the LES. Discrepancies above the BL top are caused by weak turbulence. It is important to notice, that these estimates are not affected by the horizontal shear of vertical velocity since they are not obtained from radial velocities but from spectrum width.

## Chapter 6

### Conclusions and Future Work

#### 6.1 Conclusions

In this work, the combination of LES and an LES-based wind profiler was used to study and characterize the lower atmosphere. The LES had succeeded in adequately reproducing different ideal and realistic CBL cases. Meanwhile, the virtual BLR had replicated complex voltage radar signals within the LES sub-domain used in this study.

A LES-based radar simulator that uses an Eulerian framework approach was presented for studies of the CBL in Section 3.1. The virtual radar was based on the work of Muschinski et al. (1999). However, it was refined to allow a wide range of virtual radar experiments. The simulator was capable of producing realistic complex time-series data for the case of a cloud-free CBL. For example, one could select the beam direction, beam width, pulse width, and simultaneously deploy a large number of virtual radars. The radar simulator was also designed to accommodate multiple-frequency applications, as well as monostatic, bi-static, and SA configurations. The primary differences between the virtual BLR presented here and the one developed by Muschinski et al. (1999) can be summarized as follows:

- The virtual BLR, in its present form, could accommodate multiple beams (vertical and off-vertical), which was made possible through the calculation of oblique  $C_n^2$  at each LES grid point considering the radial from the transmitter to the point.
- $C_n^2$  and velocity values were interpolated for each time step of the virtual BLR.
- Noise was generated and injected into the time-series data.

- Location of each grid point with respect to the transmitter and receiver were included as part of the equation.
- Radial velocities at each LES point were calculated as a resultant of the transmitter and receiver components.
- Radar beamwidth was also calculated independently for the transmitter and receiver.

The LES was initialized with the CBL case observed in the U.S. Southern Great Plains Atmospheric Radiation Measurement Climate Research Facility in Lamont, Oklahoma on June 8, 2007. As indicated in Botnick and Fedorovich (2008), this particular case was one for which LES predictions compare rather favorably with sounding data (see Figure 4.6). The LES output was also compared with actual radar data from the same location and date.

Range-corrected power estimates were used to retrieve profiles of  $C_n^2$  at every height for the entire simulation time using an empirical calibration method (see Section 4.2). There was good agreement between the estimates obtained from the LES, the virtual (RadSim) and real (Radar<sub>ARM</sub>). Discrepancies were observed in the RadSim at regions with low SNR when the noise power was amplified through the range correction algorithm. Also, the LES code was apparently unable to reproduce the evolution of external atmospheric forcing, which caused a discrepancy in the heights at which the  $C_n^2$  from LES and Radar<sub>ARM</sub> attain maxima values. Comparisons of horizontal winds were presented, in addition to the  $C_n^2$  in Section 4.3. The results showed a reasonable agreement in the three wind fields estimates between the RadSim and the LES, which reflects the ability of the employed LES code to reproduce basic properties of the CBL mean flow for the studied case. Estimates of the mean wind by virtual (RadSim) and real (Radar<sub>ARM</sub>) radars were also in good agreement, which indicates that the virtual BLR is capable of reliable characterization of atmospheric flow in a similar way as the real radar.

The wind fields estimates obtained from the LES and the radar simulator were in good agreement. The discrepancies observed especially on the mixed layer were  $\leq 5 \text{ m s}^{-1}$  for the horizontal wind fields and were attributed by the AWGN contamination, associate error measurements, and the horizontal shear of vertical velocity. Discrepancies observed between the LES and the real (Radar<sub>ARM</sub>) radar, in particular at high elevations were  $\leq 10 \text{ m s}^{-1}$  and were due to the apparent inability of the LES to account for the evolution of large-scale forcing.

It was shown that the LES was able to reproduce the evolution of a cloud free CBL case. The virtual BLR replicated realistic radar signals under the same conditions. The combination of both allows the characterization of different CBL parameters.

Additional comparisons between the three initial quantities were made to confirm the agreement observed. Estimates of the vertical velocity variance (see Section 4.4) from LES and RadSim were generally in good agreement. The small discrepancies between these estimates were  $\leq 1.4 \text{ m}^2 \text{ s}^{-2}$  and apparently to the differences in the spatial and temporal extent of the vertical velocity samples. The differences between the LES and Radar<sub>ARM</sub> variances might be attributed to the inability of LES to sufficiently reproduce the actual evolution of the CBL depth, particularly during the morning stages. The sharp decrease in the vertical velocity variance in the upper portion of the CBL can be used as a rough indicator of the top of the capping inversion layer and of the overall CBL top. This decrease was clearly observed in the variance data retrieved from LES and virtual radar for subsequent stages of CBL growth (see Figure 4.7).

The skewness of the vertical velocity, presented in Section 4.5, was analyzed as a function of height. In the well-mixed portion of the CBL, skewnessVertical velocity!skewness estimates are essentially positive and their magnitude increases with height in agreement with Moeng and Rotunno (1990). The estimates from the three sources agree well with an error of  $\leq 1$ , especially within the well-mixed portion of the CBL. The estimates of CBL depth from skewness profiles demonstrate fair agreement with those retrieved from vertical velocity variance distributions.

The LES and LES-based radar simulator were also used to investigate other atmospheric parameters, phenomena, or effects in the CBL. The effect of horizontal shear of vertical velocity on horizontal wind estimates was studied for DBS and SA in Section 5.1. The virtual BLR was setup during the theoretical studies to only change its phase due to variations in the three wind fields. Its magnitude was kept constant for simplicity. A known shear was introduced in the vertical velocity, and its magnitude was controlled by an external parameter *sfrac*, which allowed the amount of vertical shear within the simulator. The presence of the shear biased the zonal wind estimates. The theoretical and the measured bias were in excellent agreement, and the MSE between both quantities is  $1.55 \times 10^{-4} \text{ m}^2 \text{ s}^{-2}$  for DBS and  $1.83 \times 10^{-2} \text{ m}^2 \text{ s}^{-2}$  for SA. Under realistic conditions, the biases showed the same behavior as in the theoretical studies; when the *sfrac* increased, the bias also increased. It is important to mention that the theoretical bias was calculated at each time and height from the LES fields.

The correlation between the theoretical bias from the LES and the measured bias from the virtual BLR indicated the presence of other factors that could contribute to the measured bias. Other factors might include estimation errors, and/or horizontal wind shear. Also, the effect of the horizontal shear of the vertical velocity is observed mostly in the mixed layer, where the strong updrafts and mild downdrafts were present.

The radar was employed to retrieve variances of the wind velocity components from the simulated radar signals with different DBS settings in Section 5.2. The vertical profiles of TKE obtained with BLR were evaluated against the reference TKE profiles directly computed from the LES data. Different averaging approaches for evaluating velocity statistics were studied, and the effect of the horizontal shear of vertical velocity on the accuracy of the evaluation of the horizontal wind component variances was investigated. It was noticed that the horizontal variances were influenced by the horizontal shear in the vertical velocity, and in some cases, the bias in the variance was more than 600%. A proposed method to reduce the horizontal biases was to average the wind estimates before the calculation of the variances. However, this procedure might reduce the number of points used in the calculations making the results unrealistic. On the other hand, calculations of the vertical variance required high time resolution. Also, it is important to mention the lack of agreement observed in the horizontal variances between the time- and the space/time- average from the radar simulator and LES when the shear of vertical velocity was artificially removed.

A method of estimating turbulence intensity is through remotely sensed velocity variations (e.g., Brewster and Zrnic 1986). The Doppler spectrum is an approximation of a power-weighted distribution of radial velocities within the resolution volume of the radar. The standard deviation of the Doppler spectrum is termed the spectrum width  $\sigma_v$ , and it can be related to the turbulence energy dissipation rate  $\epsilon$  (Hocking 1985). The measurement of the width of the Doppler spectrum can be problematic in that there are several phenomena that tend to bias it to larger values, such as wind shear and finite beam-width effects (Nastrom 1997; White 1997; White et al. 1999). However, given a known beam pattern of the radar and standard DBS measurements, it is possible to minimize these effects and estimate the velocity variation due to turbulence (Cohn 1995; White 1997; White et al. 1999). The broadening of the Doppler spectrum resulting from turbulence within the radar resolution volume was estimated using the procedure outlined in White (1997); Jacoby-Koaly et al. (2002)

in Section 5.3. The TKE (eddy) dissipation rates have been estimated for alternatively (vertically and obliquely) directed radar beams. The estimates of  $\epsilon$  for the differently directed beams agreed extremely well. In LES, the dissipation rate values were estimated using a parameterized expression from Deardorff (1980). Radar and LES estimates of  $\epsilon$  in the mixed layer were found to be in good agreement with discrepancies  $\leq 2 \times 10^{-2} \text{ m}^2 \text{ s}^{-3}$ . Major discrepancies have been found at low heights where the radar simulator does not reproduce the spectrum width with accuracy due to the limited number of points within the resolution volume, and above the CBL top (*free atmosphere*) where the turbulence was low and/or the presence of residual noise was not removed.

## 6.2 Future Work

At the conclusion of this work, it is important to assess areas of potentially important future research. Subsequent work in studies of the atmosphere with LES and radar simulators should include the simulation of more LES cases to complement the realistic case presented in this dissertation. An alternative to oblique calculations of  $C_n^2$  at each LES grid cell presented in Section 3.1 can be made considering an average over the twelve edges of the LES cube surrounding the desired grid cell (see Appendix C for details).

Some of these cases will include the simulation of new realistic setups to help study the following:

- Study and compare the evolution of CBL between LES and realistic radar data from LMN. This study will include accurate measurements of the CBL depth and quantification of the discrepancies.
- Quantify the discrepancies observed between the LES and LES-based virtual radar estimates of the horizontal wind fields.
- Implement stable boundary layer (SBL) cases which are often observed at night. These cases will complement the daytime CBL presented in this study and will give a complete idea of the evolution of the BL.

Additional cases will incorporate the simulation of several idealized cases. Some will include cases with non-horizontal shear, and/or constant wind velocity. These cases will clarify the following:

- Identify and isolate cases where discrepancies that cannot be attributed to the horizontal shear of the vertical velocity are observed in the horizontal winds.
- Quantify the contribution of each of the factors identified before.

These new cases will also help to improve the estimates of TKE, in particular the discrepancies observed between the time and the space/time average in the horizontal variances. Additionally, it is important to fully calculate the second-order statistics, which will complement the calculations of vertical velocity variance and TKE, in particular the calculations of the kinematic momentum fluxes ( $\overline{u'w'}$  and  $\overline{v'w'}$ ). A first attempt to calculate these fluxes was made by Scipi3n et al. (2007), but the results were inconclusive. This new set of cases will allow the study of these fluxes to be more detailed and to incorporate different conditions. Complementary to the calculation of the kinematic momentum fluxes, profiles of kinematic heat flux ( $\overline{\Theta'w'}$ ) can also be obtained from the same data set. Profiles of virtual potential temperature can be obtained if the simulation of a RASS system is included within the radar simulator.

The mixed layer height in the SBL reaches its maximum at approximately 200 m (e.g., Asimakopoulos et al. 2004) at night. Usually, radars have a range resolution of 100 m, which might be too coarse for SBL studies. A more appropriate instrument for remote sensing of the SBL is a SODAR (SOund Detection And Ranging), which has a range resolution as small as 5 m. In the literature, estimations of the SBL mixed layer height are widely spread (e.g., Beyrich and Weill 1993; Beyrich 1995; Crescenti 1997; Asimakopoulos et al. 2004), as well as studies of the atmospheric fluxes based on wind profiles retrieved from a Doppler sodar (e.g., Giannini et al. 1997). For studies of the SBL, the LES will have a finer resolution (at least 2 m) than the LES used in CBL studies (10 m and 20 m). A LES-based sodar can be simulated from the fine LES fields to study the SBL. As in the case of CBL, true sodar retrievals can aid in the validation of LES and virtual sodar.

Finally, the LES with fine resolution, especially designed for SBL studies, can be extended to improve the previous daytime CBL studies. These new high-resolution cases will give a better population in the radar resolution volume, especially at lower elevations. It can also help with the determination of small layers using FDI or RIM. Additionally, other techniques can be implemented and tested to study the CBL, like the turbulent eddy profiler (TEP) (Cheong et al. 2004b, 2008).

## Bibliography

- Ahrens, C. D., 1991: *Meteorology Today: An introduction to weather, climate, and the environment*. 4th ed., West Publishing Company.
- Angevine, W. M., 1999: Entrainment results with advection and case studies from Flatland boundary layer experiments. *J. Geophys. Res.*, **104**, 30 947–30 963.
- Angevine, W. M., R. J. Doviak, and Z. Sorbjan, 1994a: Remote sensing of vertical variance and surface heat flux in a convective boundary layer. *J. Appl. Meteorol.*, **33**, 977–983.
- Angevine, W. M., A. B. White, and S. K. Avery, 1994b: Boundary-layer depth and entrainment zone characterization with a boundary-layer profiler. *Boundary-Layer Meteorol.*, **68**, 375–385.
- Asimakopoulos, D. N., C. G. Helmig, and J. Michopoulos, 2004: Evaluation of sodar methods in the determination of the atmospheric boundary layer mixing height. *Meteor. Atmos. Phys.*, **85**, 85 – 92, DOI 10.1007/s00 703–003–0036–9.
- Atlas, D., (Ed.) , 1990: *Radar in Meteorology: Battan Memorial and 40th Anniversary*. Amer. Meteor. Soc.
- Atlas, D. and K. R. Hardy, 1966: Radar analysis of the clear atmosphere: Angels. *Progress in Radio Science 1963-1966: Proc. XVth General Assembly of the Int. Scientific Radio Union*, 401–469.
- Baldwin, M. W., 1948: Radar reflections from the lower atmosphere. *Proc. IRE*, **36**, 363.
- Balsley, B. B., 1981: The MST technique - A brief review. *J. Atmos. Terr. Phys.*, **43 (5/6)**, 495–509.
- Balsley, B. B. and K. Gage, 1982: On the use of radars for operational wind profiling. *Bull. Amer. Meteor. Soc.*, **63 (9)**, 1009–1018.
- Bean, B. R. and E. J. Dutton, 1966: *Radio Meteorology*, Natl. Bur. Stand. Monogr., Vol. 92. Supt. Doc. U.S. Govt. Printing Office, Washington D.C., 435 pp.
- Benjamin, S. G., et al., 2004: An hourly assimilation-forecast cycle: The RUC. *Mon. Wea. Rev.*, **132 (2)**, 495–518. DOI: 10.1175/1520–0493(2004)132.

- Beyrich, F., 1995: Mixing-height estimation in the convective boundary layer using sodar data. *Boundary-Layer Meteor.*, **74**, 1–18.
- Beyrich, F. and A. Weill, 1993: Some aspects of determining the stable boundary layer depth from sodar data. *Boundary-Layer Meteor.*, **63**, 97 – 116.
- Boodoo, S., D. Hudak, M. Leduc, and N. Donaldson, 2008: Observations of the melting layer in southern Canada with a C-band dual polarized radar. *ERAD 2008 - The Fifth European Conference on Radar Meteorology and Hydrology, Helsinki, Finland*, [Available online at <http://erad2008.fmi.fi/proceedings/extended/erad2008-0205-extended.pdf>].
- Botnick, A. M. and E. Fedorovich, 2008: Large eddy simulation of atmospheric convective boundary layer with realistic environmental forcings. *Quality and Reliability of Large-Eddy Simulations, J. Meyers et. al., Eds., Springer*, 193 – 204.
- Brewster, K. A. and D. S. Zrnic, 1986: Comparison of eddy dissipation rates from spatial spectra of Doppler velocities and Doppler spectrum widths. *J. Atmos. Oceanic Technol.*, **3**, 440–452.
- Briggs, B., 1984: *The analysis of spaced sensor records by correlation techniques.*, MAP Handbook, Vol. 13, chap. 13, 166 – 186. SCOSTEP Sec., Univ. of Ill., Urbana, IL.
- Briggs, B., G. J. Phillips, and D. H. Shinn, 1950: The analysis of observation on spaced receivers of the fading radio signals. *Proc. Phys. Soc. London Sect. B.*, **63**, 106 – 121.
- Cheong, B. L., M. W. Hoffman, and R. D. Palmer, 2004a: Efficient atmospheric simulation for high-resolution radar imaging application. *J. Atmos. Oceanic Technol.*, **21**, 374 – 378.
- Cheong, B. L., M. W. Hoffman, R. D. Palmer, S. J. Frasier, and F. J. Lopez-Dekker, 2004b: Pulse pair beamforming and the effects of reflectivity field variations on imaging radars. *Radio Sci.*, **39**, RS3014, doi:10.1029/2002RS002843.
- Cheong, B. L., T.-Y. Yu, R. D. Palmer, K.-F. Yang, M. W. Hoffman, S. J. Frasier, and F. J. Lopez-Dekker, 2008: Effects of wind fields inhomogeneities of Doppler beam swinging revealed by an imaging radar. *J. Atmos. Oceanic Technol.*, **25**, 1414–1422. DOI: 10.1175/2007JTECHA969.1.
- Chilson, P. B., 2004: The retrieval and validation of Doppler velocity estimates from range imaging. *J. Atmos. Oceanic Technol.*, **21** (7), 1033–1043.
- Chilson, P. B., T.-Y. Yu, R. G. Strauch, A. P. Muschinski, and R. D. Palmer, 2003: Implementation and validation of range imaging on a UHF radar wind profiler. *J. Atmos. Oceanic Technol.*, **20**, 987–996.
- Cohn, S. A., 1995: Radar measurements of turbulent eddy dissipation rate in the troposphere: A comparison of techniques. *J. Atmos. Oceanic Technol.*, **12**, 85–95.

- Cohn, S. A. and W. M. Angevine, 2000: Boundary level height and entrainment zone thickness measured by lidars and wind-profiling radars. *J. Appl. Meteorol.*, **39**, 1233–1247.
- Conzemius, R. J. and E. Fedorovich, 2006: Dynamics of sheared convective boundary layer entrainment. Part I: Meteorological background and large-eddy simulations. *J. Atmos. Sci.*, **63**, 1151–1178.
- Crescenti, G. H., 1997: A look back on two decades of Doppler sodar comparison studies. *Bull. Amer. Meteor. Soc.*, **78** (4), 651–673.
- Crum, T. D. and R. L. Alberty, 1993: The WSR-88D and the WSR-88D operational support facility. *Bull. Amer. Meteor. Soc.*, **74**, 1669–1687.
- Crum, T. D., R. E. Saffle, and J. W. Wilson, 1998: An update to the NEXRAD program and future WSR-88D support to operations. *Weather Forecast.*, **13** (2), 253–262.
- Dabberdt, W. F., G. L. Frederick, R. M. Hardesty, W. C. Lee, and K. Underwood, 2004: Advances in meteorological instrumentation for air quality and emergency response. *Meteor. Atm. Phys.*, **87**, 57–88.
- Dazhang, T., S. G. Geotis, R. E. Passarelli Jr., A. L. Hansen, and C. L. Frush, 1984: Analysis and correction of dual PRF velocity data. *22<sup>nd</sup> Conf. on Radar Meteorology, Zurich, Switzerland*, Amer. Meteor. Soc., Vol. Preprints, 523–527.
- Deardorff, J. W., 1970: Preliminary results from numerical integration of the unstable boundary layer. *J. Atmos. Sci.*, **27**, 1209 – 1211.
- Deardorff, J. W., 1972: Numerical investigation of neutral and unstable planetary boundary layers. *J. Atmos. Sci.*, **29**, 91–115.
- Deardorff, J. W., 1980: Stratocumulus-capped mixed layers derived from a three-dimensional model. *Boundary-Layer Meteorol.*, **18**, 495 – 527.
- Doviak, R. and D. S. Zrnić, 1984: Reflection and scatter formula for anisotropically turbulent air. *Radio Sci.*, **19**, 325–336.
- Doviak, R. J. and M. J. Berger, 1980: Turbulence and waves in the optical clear planetary boundary layer resolved by dual Doppler radars. *Radio Sci.*, **15**, 297 – 317.
- Doviak, R. J., R. J. Latatits, and C. L. Holloway, 1996: Cross correlations and cross spectra for spaced antenna wind profilers. 1. Theoretical analysis. *Radio Sci.*, **31** (1), 157 – 180.
- Doviak, R. J., G. Zhang, S. A. Cohn, and W. O. J. Brown, 2004: Comparison of spaced-antenna baseline wind estimators: Theoretical and simulated results. *Radio Sci.*, **39** (RS1006), DOI: 10.1029/2003RS002931.

- Doviak, R. J. and D. S. Zrnić, 1993: *Doppler Radar and Weather Observations*. 2d ed., Academic Press, San Diego, CA.
- Dunlap Jr., O. E., 1946: *Radar: What Radar is and How It Works*. 2d ed., Harper and Brothers, New York, NY.
- Eaton, F. D., S. A. McLaughlin, and J. R. Hines, 1995: A new frequency-modulated continuous wave radar for studying planetary boundary layer morphology. *Radio Sci.*, **30** (1), 75–88.
- Ecklund, W. L., K. S. Gage, and C. R. Williams, 1995: Tropical precipitation studies using a 915-MHz wind profiler. *Radio Sci.*, **30**, 1055–1064.
- Fedorovich, E. and R. Conzemius, 2008: Effects of wind shear on the atmospheric convective boundary layer structure and evolution. *Acta Geophysica*, **56**, 114 – 141.
- Fedorovich, E., R. Conzemius, and D. Mironov, 2004a: Convective entrainment into a shear-free linearly stratified atmosphere: Bulk models re-evaluated through large-eddy simulations. *J. Atmos. Sci.*, **61**, 281–295.
- Fedorovich, E., R. Kaiser, M. Rau, and E. Plate, 1996: Wind tunnel study of turbulent flow structure in the convective boundary layer capped by temperature inversion. *J. Atmos. Sci.*, **53** (9), 1273–1289.
- Fedorovich, E., F. T. M. Nieuwstadt, and R. Kaiser, 2001: Numerical and laboratory study of horizontally evolving convective boundary layer. Part I: Transition regimes and development of the mixed layer. *J. Atmos. Sci.*, **58**, 70–86.
- Fedorovich, E., et al., 2004b: Entrainment into sheared convective boundary layers as predicted by different large eddy simulation codes. *Preprints, 16th Symp. on Boundary Layers and Turbulence, Amer. Meteor. Soc., 9-13 August, Portland, Maine, USA*, CD-ROM, P4.7.
- Flowers, W. L., L. Parker, G. Hoidale, E. Sanantonio, and J. Hines, 1994: Evaluation of a 924 MHz wind profiling radar. Tech. rep., Army Research Laboratory Final Rep. ARL-CR 101, CD-ROM.
- Forsyth, D. E., et al., 2002: The National Weather Radar Testbed (Phased-Array). *18th International Conference on Interactive Information and Processing Systems (IIPS), Orlando FL.*, Amer. Meteor. Soc., Vol. Preprints, 140–141.
- Forsyth, D. E., et al., 2005: The National Weather Radar Testbed (Phased-Array). *21st International Conf. on Interactive Information Processing Systems for Meteor., Oceanography, and Hydrologist, San Diego, CA*, Amer. Meteor. Soc., Vol. Preprints.
- Friend, A. W., 1949: Theory and practice of tropospheric sounding by radar. *Proc. IEEE*, **37** (116–138).

- Gage, K. S. and B. B. Balsley, 1978: Doppler radar probing of the clear atmosphere. *Bull. Amer. Meteor. Soc.*, **59** (9), 1074–1093.
- Gage, K. S., C. R. Williams, and W. L. Ecklund, 1994: UHF wind profilers: A new tool for diagnosing and classifying tropical cloud systems. *Bull. Amer. Meteor. Soc.*, **75**, 2289–2294.
- Giangrande, S. E., J. Krause, and A. Ryzhkov, 2008: Automatic designation of the melting layer with a polarimetric prototype of the WSR-88D radar. *J. Appl. Meteorol. Climatol.*, **47** (5), 1357–1364. DOI: 10.1175/2007JAMC1634.1.
- Giangrande, S. E. and A. Ryzhkov, 2008: Estimation of rainfall based on the results of polarimetric echo classification. *J. Appl. Meteorol. Climatol.*, **47** (9), 2445–2462. DOI: 10.1175/2008JAMC1753.1.
- Giannini, L., S. Argentini, G. Mastrantonio, and L. Rossino, 1997: Estimation of flux parameters from sodar wind profiles. *Atmos. Environ.*, **31** (9), 1307–1313.
- Gossard, E. E. and J. H. Richter, 1970: The shape of internal waves of finite amplitude from high resolution radar sounding of the lower atmosphere. *J. Atmos. Sci.*, **27**, 971–973.
- Gossard, E. E. and R. G. Strauch, 1983: *Radar Observations of Clear Air and Clouds*. Elsevier, 280 pp.
- Grimsdell, A. W. and W. M. Angevine, 2002: Observation of the afternoon transition of the convective boundary layer. *J. Appl. Meteorol.*, **41**, 3–11.
- Hardy, K. R., D. Atlas, and K. M. Glover, 1966: Multiwavelength backscatter from clear atmosphere. *J. Geophys. Res.*, **71**, 1537–1552.
- Hardy, K. R. and H. Ottersten, 1969: Radar investigations of convective patterns in the clear atmosphere. *J. Atmos. Sci.*, **26**, 666–672.
- Harrold, T. W. and K. A. Browning, 1971: Identification of preferred areas of shower development by means of high power radar. *Quart. J. Roy. Meteor. Soc.*, **97**, 330–339.
- Heinselman, P. L., D. L. Priegnitz, K. L. Manross, T. M. Smith, and R. W. Adams, 2008: Rapid sampling of severe storms by the National Weather Radar Testbed Phased Array Radar. *Weather Forecast.*, **23** (5), 808–824. DOI: 10.1175/2008WAF2007071.1.
- Hildebrand, P. H. and R. S. Sekhon, 1974: Objective determination of the noise level in Doppler spectra. *J. Appl. Meteorol.*, **13**, 808–811.
- Hocking, W. K., 1983: On the extraction of atmospheric turbulence parameters from radar backscatter Doppler spectra, Part I; Theory. *J. Atmos. Terr. Phys.*, **45**, 89–102.

- Hocking, W. K., 1985: Measurement of turbulent eddy dissipation rates in the middle atmosphere by radar techniques: A review. *Radio Sci.*, **20** (6), 1403–1422.
- Hocking, W. K., 1988: Two years of continuous measurements of turbulence parameters in the upper mesosphere and lower thermosphere made with a 2-MHz radar. *J. Geophys. Res.*, **93**, 2475–2491.
- Hocking, W. K., 1992: On the relationship between the strength of atmospheric radar backscatter and the intensity of atmospheric turbulence. *Adv. Space Res.*, **12** (10), 207–213.
- Hocking, W. K., 1996: An assessment of the capabilities and limitations of radars in measurements of upper atmospheric turbulence. *Adv. Space Res.*, **17** (11), 37–47.
- Hocking, W. K. and P. K. L. Mu, 1997: Upper and middle tropospheric kinetic energy dissipation rates from measurements of  $C_n^2$  – review of theories, *in-situ* investigations, and experimental studies using the Buckland Park atmospheric radar in Australia. *J. Atmos. Sol.-Terr. Phys.*, **59** (14), 1779–1803.
- Holdsworth, D. A. and I. M. Reid, 1995: A simple model of atmospheric radar backscatter: Description and application to the full correlation analysis of spaced antenna data. *Radio Sci.*, **30**, 1263–1280.
- Holloway, C. L., R. J. Doviak, S. A. Cohn, R. J. Latatits, and J. S. V. Baelen, 1997: Cross correlations and cross spectra for spaced antenna wind profilers. 2. Algorithms to estimate wind and turbulence. *Radio Sci.*, **32** (3), 967–982.
- Holton, J. R., 2004: *An Introduction to Dynamic Meteorology*, International Geophysics Series, Vol. 88. 4th ed., Elsevier Academic Press.
- Holtslag, A. A. M. and P. G. Duynkerke, 1998: Clear and cloudy boundary layers. *Royal Netherlands Academy of Arts and Sciences, Amsterdam*, 372.
- Istok, M. J. and R. J. Doviak, 1986: Analysis of the relation between Doppler spectral width and thunderstorm turbulence. *J. Atmos. Sci.*, **43** (20), 2199 – 2214.
- Istok, M. J., et al., 2009: WSR-88D dual polarization initial operational capabilities. *25<sup>th</sup> International Conference on Interactive Information and Processing Systems (IIPS), Phoenix, AZ, USA*, Amer. Meteor. Soc., Vol. Preprints.
- Jacoby-Koaly, S., B. Campistron, S. Bernard, B. Bénech, F. Arduin-Girard, J. Dessens, E. Dupont, and B. Carissimo, 2002: Turbulent dissipation rate in the boundary layer via UHF wind profiler Doppler spectral width measurements. *Boundary-Layer Meteor.*, **103**, 361–389.
- Kaiser, R. and E. Fedorovich, 1998: Turbulence Spectra and Dissipation Rates in a Wind Tunnel Model of the Atmospheric Convective Boundary Layer. *J. Atmos. Sci.*, **55**, 580 –594.

- Khanna, S. and J. G. Brasseur, 1998: Three-dimensional buoyancy- and shear-induced local structure of the atmospheric boundary layer. *J. Atmos. Sci.*, **55**, 710–743.
- Konrad, T. G., 1970: The dynamics of the convective process in clear air as seen by radar. *J. Atmos. Sci.*, **27**, 1138–1147.
- Kudeki, E. and G. R. Stitt, 1987: Frequency domain interferometry: A high resolution radar technique for studies of atmospheric turbulence. *Geophys. Res. Lett.*, **14**, 198.
- Lei, L., G. Zhang, R. J. Doviak, R. D. Palmer, B. L. Cheong, M. Xue, Q. Cao, and Y. Li, 2011: Multi-lag correlation estimator for polarimetric radar measurements in the presence of noise. *J. Atmos. Oceanic Technol.*, Submitted.
- Luce, H., M. Yamamoto, S. Fukao, D. Helal, and M. Crochet, 2001: A frequency domain radar interferometric imaging (FII) technique based on high resolution methods. *J. Atmos. Sol.-Terr. Phys.*, **63**, 221–234.
- Mason, P. J., 1989: Large-eddy simulation of the convective atmospheric boundary layer. *J. Atmos. Sci.*, **46**, 1492–1516.
- Meischner, P., (Ed.) , 2004: *Weather Radar: Principles and Advanced Applications*. 1st ed., Springer Berlin Heidelberg New York.
- Moeng, C.-H., 1984: A large-eddy-simulation model for the study of planetary boundary layer turbulence. *J. Atmos. Sci.*, **41**, 2052–2062.
- Moeng, C.-H. and R. Rotunno, 1990: Vertical-velocity skewness in the buoyancy-driven boundary layer. *J. Atmos. Sci.*, **19 (9)**, 1149–1162.
- Moeng, C.-H. and P. P. Sullivan, 1994: A comparison of shear- and buoyancy-driven planetary boundary layer flows. *J. Atmos. Sci.*, **51**, 999–1022.
- Muschinski, A. P., P. P. Sullivan, R. J. Hill, S. A. Cohn, D. H. Lenschow, and R. J. Doviak, 1999: First synthesis of wind-profiler signal on the basis of large-eddy simulation data. *Radio Sci.*, **34 (6)**, 1437–1459.
- Nastrom, G. D., 1997: Doppler radar spectral width broadening due to beamwidth and wind shear. *Ann. Geophys.*, **15**, 786–796.
- Nieuwstadt, F. T. M., 1990: Direct and large-eddy simulation of free convection. *Proc. 9th Internat. Heat Transfer Conference*, 37–47.
- Ottersten, H., 1969: Mean vertical gradient of potential refractive index in turbulent mixing and radar detection of CAT. *Radio Sci.*, **4 (12)**, 1247–1249.
- Palmer, R. D., R. F. Woodman, S. Fukao, M. F. Larsen, M. Yamamoto, T. Tsuda, and S. Kato, 1990: Frequency domain interferometry observations of tropo/stratospheric scattering layers using the MU radar: Description and first results. *Geophys. Res. Lett.*, **17**, 2189–2192.

- Palmer, R. D., T.-Y. Yu, and P. B. Chilson, 1999: Range imaging using frequency diversity. *Radio Sci.*, **34** (6), 1485–1496.
- Park, H. S., A. V. Ryzhkov, D. S. Zrnić, and K.-E. Kim, 2009: The hydrometeor classification algorithm for the polarimetric WSR-88D: Description and application to an MCS. *Weather Forecast.*, **24** (3), 730–748.
- Pope, S. B., 2000: *Turbulent Flows*. Cambridge University Press.
- Reinoso-Rondinel, R., T.-Y. Yu, and S. Torres, 2010: Multifunction Phased-Array Radar: Time balance scheduler for adaptive weather sensing. *J. Atmos. Oceanic Technol.*, **27** (11), 1854–1867. DOI: 10.1175/2010JTECHA1420.1.
- Richter, J. H., 1969: High resolution tropospheric radar sounding. *Radio Sci.*, **4**, 1261–1268.
- Rinehart, R. E., 2004: *RADAR for Meteorologists*. 4th ed., Rinehart Publications, P.O. Box 30800, Columbia, MO 65203-3800, USA - <http://radarwx.com>.
- Rogers, R. R., W. L. Ecklund, D. A. Carter, K. S. Gage, and S. A. Ethier, 1993: Research applications of a boundary-layer wind profiler. *Bull. Amer. Meteor. Soc.*, **74**(4), 567–580.
- Ryzhkov, A., S. E. Giangrande, and T. J. Shuur, 2005a: Rainfall estimation with a polarimetric prototype of WSR-88D. *J. Appl. Meteorol.*, **44** (4), 502–515.
- Ryzhkov, A., T. J. Shuur, D. W. Burgess, P. L. Heinselman, S. E. Giangrande, and D. S. Zrnić, 2005b: The Joint POLARization Experiment: Polarimetric rainfall measurements and hydrometeor classification. *Bull. Amer. Meteor. Soc.*, **86** (6), 809–824.
- Sachidananda, M. and D. S. Zrnić, 1986: Recovery of spectral moments from overlaid echoes in a Doppler weather radar. *IEEE Trans. Geosci. Remote Sens.*, **24**, 751–764.
- Schmidt, H. and U. Schumann, 1989: Coherent structure of the convective boundary layer derived from large eddy simulations. *J. Fluid Mech.*, **200**, 511–562.
- Scipi3n, D. E., P. B. Chilson, E. Fedorovich, and R. D. Palmer, 2008: Evaluation of an LES-based wind profiler simulator for observations of a daytime atmospheric convective boundary layer. *J. Atmos. Oceanic Technol.*, **25**, 1423–1436. DOI: 10.1175/2007JTECHA970.1.
- Scipi3n, D. E., R. D. Palmer, P. B. Chilson, E. Fedorovich, and A. M. Botnick, 2009: Retrieval of convective boundary layer wind fields statistics from radar profiler measurements in conjunction with large eddy simulations. *Meteorol. Z.*, **18** (2), 175–187.

- Scipi3n, D. E., R. D. Palmer, E. Fedorovich, P. B. Chilson, and A. M. Botnick, 2007: Structure of a daytime convective boundary layer revealed by a virtual radar based on large eddy simulation. *33<sup>rd</sup> Conference on Radar Meteorology, Cairns, Australia*, American Metr. Soc.
- Shanmugan, K. S. and A. M. Breipohl, 1988: *Random Signals: Detection, Estimation, and Data Analysis*. John Wiley & Sons, Inc.
- Sheppard, E. L. and M. F. Larsen, 1992: Analysis of model simulations of spaced antenna/radar interferometer measurements. *Radio Sci.*, **27** (5), 759–768.
- Siggia, A. D. and R. E. Passarelli Jr., 2004: Gaussian model adaptive processing (GMAP) for improved ground clutter cancellation and moment calculation. *ERAD 2004*, Copernicus GmbH, 67–73.
- Sirmans, D., D. S. Zrni3c, and B. Bungarner, 1976: Extension of maximum unambiguous Doppler velocity by use of two sampling rates. *17<sup>th</sup> Conf. on Radar Meteorology, Seattle, WA*, Amer. Meteor. Soc., Vol. Preprints, 23–28.
- Skolnik, M. I., (Ed.) , 1990: *Radar Handbook*. 2d ed., McGraw-Hill, New York.
- Skolnik, M. I., 2001: *Introduction to Radar systems*. 3d ed., McGraw-Hill, New York.
- Sorbjan, Z., 1996: Effects caused by varying the strength of the capping inversion based on a large eddy simulation model of the shear-free convective boundary layer. *J. Atmos. Sci.*, **53**, 2015–2024.
- Sorbjan, Z., 2004: Large-eddy simulation of the baroclinic mixed layer. *Boundary-Layer Meteor.*, **112**, 57–80.
- Stevens, B. and D. H. Lenschow, 2001: Observations, experiments, and large eddy simulation. *Bull. Amer. Meteor. Soc.*, **82**, 283–294.
- Strauch, R. G., 1976: Theory and application of the FM-CW Doppler radar. Ph.D. thesis, Graduate School of the University of Colorado, Department of Electrical Engineering.
- Stull, R., 2000: *Meteorology for Scientists and Engineers*. 2d ed., Brooks/Cole Thomson Learning.
- Stull, R. B., 1988: *An Introduction to Boundary Layer Meteorology*. Kluwer.
- Sullivan, P., C.-H. Moeng, B. Stevens, D. H. Lenschow, and S. D. Mayor, 1998: Structure of the entrainment zone capping the convective atmospheric boundary layer. *J. Atmos. Sci.*, **55**, 3042–3064.
- Tatarskii, V. I., 1961: *Wave Propagation in a Turbulent Medium*. McGraw-Hill, New York.
- Tatarskii, V. I., 1971: *The effects of turbulent atmosphere on wave propagation*. NOAA U.S. Department of Commerce and NSF.

- Taylor, G. I., 1938: The spectrum turbulence. *Proc. Roy. Soc.*, **164**, 476–490.
- Torres, S. M., Y. F. Dubel, and D. S. Zrnić, 2004: Design, implementation, and demonstration of a staggered PRT algorithm for the WSR-88D. *J. Atmos. Oceanic Technol.*, **21**, 1389–1399.
- Van Zandt, T. E., 2000: A brief history of the development of wind-profiling on MST radars. *Ann. Geophys.*, **18**, 740–749.
- Van Zanten, M. C., P. G. Duynkerke, and J. W. M. Cuijpers, 1999: Entrainment parameterization in convective boundary layers derived from large eddy simulations. *J. Atmos. Sci.*, **56**, 813–828.
- Wallace, J. M. and P. V. Hobbs, 2006: *Atmospheric science: An introductory survey*. 2d ed., Elsevier Academic Press.
- Weadon, M., P. L. Heinselman, D. E. Forsyth, W. E. Benner, G. S. Torok, and J. Kimpel, 2009: Multifunction Phased Array Radar. *Bull. Amer. Meteor. Soc.*, **90** (3), 385–389.
- White, A. B., 1997: Radar remote sensing of scalar and velocity microturbulence in the convective boundary layer. NOAA Technical Memorandum ERL ETL-276, Environmental Research Laboratories.
- White, A. B., R. J. A. Lataitis, and R. S. Lawrence, 1999: Space and time filtering of remotely sensed velocities turbulence. *J. Atmos. Oceanic Technol.*, **16**, 1967–1972.
- Wilczak, J. M., E. E. Gossard, W. D. Neff, and W. L. Eberhard, 1996: Ground-based remote sensing of the atmospheric boundary layer: 25 years of progress. *Boundary-Layer Meteorol.*, **78**, 321–349.
- Woodman, R. F. and A. Guillen, 1974: Radar observations of winds and turbulence in the stratosphere and mesosphere. *J. Atmos. Sci.*, **31**, 493–505.
- Wyngaard, J. C., 1998: Experiment, numerical modeling, numerical simulation, and their roles in the study of convection. Buoyant convection in geophysical flows. *E. J. Plate et al., Eds., Kluwer*, 239–252.
- Yu, T.-Y., 2000: Radar studies of the atmosphere using spatial and frequency diversity. Ph.D. thesis, University of Nebraska, Lincoln, Nebraska.
- Yu, T.-Y. and W. O. J. Brown, 2004: High-resolution atmospheric profiling using combined spaced antenna and range imaging techniques. *Radio Sci.*, **39** (RS1011), DOI: 10.1029/2003RS002907.
- Yu, T.-Y., M. B. Orescanin, C. D. Curtis, D. S. Zrnić, and D. E. Forsyth, 2007: Beam multiplexing using the Phased-Array Weather Radar. *J. Atmos. Oceanic Technol.*, **24** (4), 616–626. DOI: 10.1175/JTECH2052.1.
- Yu, T.-Y. and R. D. Palmer, 2001: Atmospheric radar imaging using multiple-receiver and multiple-frequency techniques. *Radio Sci.*, **36** (6), 1493–1503.

- Yu, T.-Y., R. Reinoso-Rondinel, and R. D. Palmer, 2009: Investigation of Non-Gaussian Doppler spectra observed by weather radar in tornadic supercell. *J. Atmos. Oceanic Technol.*, **26**, 444–461. DOI: 10.1175/2008JTECHA1124.1.
- Zhang, G. and R. J. Doviak, 2007: Spaced-antenna interferometry to measure cross-beam wind, shear, and turbulence: Theory and formulation. *J. Atmos. Oceanic Technol.*, **64**, 791 – 805. DOI: 10.1175/JTECH2004.1.
- Zhang, G., R. J. Doviak, J. Vivekanandan, W. O. J. Brown, and S. A. Cohn, 2003: Cross-correlation radio method to estimate cross-beam wind and comparison with full correlation analysis. *Radio Sci.*, **38 (3)**, DOI: 10.1029/2002RS002682.
- Zilitinkevich, S. S., 1991: Turbulent penetrative convection. *Avebury Technical, Aldershot*, 179.
- Zrnić, D. S., et al., 2007: Agile-beam Phased Array Radar for weather observations. *Bull. Amer. Meteor. Soc.*, **88 (11)**, 1753–1766.

## Appendix A - List Of Symbols

$A$	Complex amplitude
$A_e$	Empirical constant in the inertial subrange of velocity spectrum
$A^{(p)}$	Amplitude at the $p^{th}$ LES grid cell
$\mathbf{A}$	Matrix for the solution of DBS
$c$	Speed of Light
cm	Centimeter, $10^{-2}$ meters
$C$	Radar calibration constant
$C_n^2$	Structure function parameter of refractive index
$C_n^{2(p)}$	Structure function parameter of refractive index at the $p^{th}$ LES grid cell
$c_p$	Specific heat for air
$c_{11}$	Autocorrelation function
$\widehat{c}_{11}$	Estimate of autocorrelation function
$c_{12}$	Cross-correlation function
$\widehat{c}_{12}$	Estimate of cross-correlation function
$c_0$	Amplitude offset of the auto- or cross-correlation function
$D$	Diameter of a spherical drop
DC	Direct Current
$e$	Partial pressure of water vapor
$\widehat{\mathbf{e}}_{tx}^{(p)}$	Unit vector from the transmitting antenna to the $p^{th}$ LES grid cell
$\widehat{\mathbf{e}}_{rx}^{(p)}$	Unit vector from the receiving antenna to the $p^{th}$ LES grid cell
$E$	Sub-grid TKE viscous dissipation rate
$E(\kappa)$	Energy spectrum of turbulence

$E_t^{(u)}(\kappa)$	Transverse energy spectrum of turbulence obtained from LES zonal wind
$E_l^{(u)}(\kappa)$	Longitudinal energy spectrum of turbulence obtained from LES zonal wind
$E_t^{(v)}(\kappa)$	Transverse energy spectrum of turbulence obtained from LES meridional wind
$E_l^{(v)}(\kappa)$	Longitudinal energy spectrum of turbulence obtained from LES meridional wind
$E_t^{(w)}(\kappa)$	Transverse energy spectrum of turbulence obtained from LES vertical wind
$f$	Frequency
$f_d$	Doppler frequency
$f_N$	Nyquist frequency
$f_s$	Pulse repetition frequency
$f^2(\theta, \phi)$	(One-way) normalized power density pattern
$g$	Gravitational acceleration
$G$	Gain of the transmitting or receiving antennas
$G_{tx}$	Gain of the transmitting antenna
$G_{rx}$	Gain of the receiving antenna
GHz	Gigahertz, $10^9$ Hz
$H$	Sensible heat flux
hPa	Hectopascal, $10^2$ Pascals
Hz	Hertz, unit increment of frequency
$I(t, r_0)$	In-phase component of the complex voltage signal
J	Joules
$k$	Wavenumber
$k_B$	Bragg wavenumber
kg	Kilogram
$k_m$	Estimate of the peak of the Doppler spectrum
$k_0$	Radar wavenumber
K	Kelvin, unit increment of temperature
$K_h$	Sun-grid eddy diffusivity
$K_m$	Sub-grid eddy viscosity
$K_m$	Complex dielectric factor
$K_w$	Complex dielectric factor for liquid water

$K_i$	Complex dielectric factor for ice
km	Kilometer, $10^3$ meters
kW	Kilowatts, $10^3$ Watts
$l$	Sub-grid mixing length
$l$	Losses
$LH$	Latent heat flux
$L_v$	Latent heat of vaporization
m	Meter, unit increment of length
$m$	Complex refractive index for water
$M$	Number of signal samples
$M$	Number of LES grid points within the resolution volume
mb	Millibar, $10^{-3}$ bar
mm	Millimeter, $10^{-3}$ meters
MHz	Megahertz, $10^6$ Hz
$n$	Refractive index
$n$	Refractive index at level $z$
$n_1$	Refractive index at level $z + \Delta z$
$n_2$	Refractive index at level $z - \Delta z$
$n_{xy}$	Refractive index at point $(x,y)$
$n_{x_i,y_i}$	Refractive index at the fixed grid cells $(x_i,y_i)$
$N$	Refractivity
$N$	Noise power
$\hat{N}$	Estimated noise power
$N(D)$	Particle size distribution
$p$	Surface pressure from RUC
$\tilde{p}$	Resolved pressure
$\hat{P}$	Estimated total power
Pa	Pascal
$P_r$	Received power
$P_t$	Transmitted power
$P$	Atmospheric pressure
$P_0$	Pressure at $z=0$ m
$p_0$	Hydrostatic atmospheric pressure
$q$	Specific humidity

$Q(t, r_0)$	Quadrature component of the complex voltage signal
$r$	Range
$\mathbf{r}$	Position vector
$r_a$	Range Aliasing
$r_{tx0}$	Range from the transmitting antenna to the center of the resolution volume
$r_{rx0}$	Range from the receiving antenna to the center of the resolution volume
$r_{max}$	Maximum range available at the LES sub-domain
$r_0$	Range from the antenna to the center of the resolution volume
$R$	Gas constant for dry air
RxA	Location of receiver A in the spaced antenna configuration
RxB	Location of receiver B in the spaced antenna configuration
RxC	Location of receiver C in the spaced antenna configuration
RxD	Location of receiver D in the spaced antenna configuration
$R(\tau)$	Autocorrelation function
$\widehat{R}(k)$	Estimated autocorrelation function
$sfrac$	Vertical velocity fraction
s	Second
$s_u$	Shear in the zonal direction
$s_{uz0}$	Range corrected shear in the zonal direction
$s_v$	Shear in the meridional direction
$s_{vz0}$	Range corrected shear in the meridional direction
$s_w$	Shear in the vertical direction
$S$	Signal power
$\widehat{S}$	Estimated signal power
$\widetilde{s_{ij}}$	Deformation tensor for filtered velocity
$S(f)$	Doppler spectrum in frequency

$\widehat{S}(f)$	Estimated Doppler spectrum
$S(v)$	Doppler spectrum in velocity
$\widehat{S}_n(k)$	Normalized Doppler spectrum
SNR	Signal-to-Noise Ratio
$t$	Time
$t_0$	Initial time for variable interpolation from LES
$t_1$	Final time for variable interpolation from LES
$t_D$	Radar dwell time
$T$	Absolute temperature
$T_r$	Range time
$T_s$	Pulse repetition time
Tx	Location of transmitter in the spaced antenna configuration
$u$	Zonal wind field
$u'$	Fluctuating component of the zonal velocity
$\widetilde{u}$	Measured zonal wind field biased by the horizontal shear of vertical velocity
$\mathbf{u}$	Three dimensional velocity vector
$u_0$	Uniform zonal wind field
$\widetilde{u}_i$	Resolved velocity components - Einstein summation convention
$u_g$	Zonal geostrophic wind
$U(t)$	Transmitted pulse shape
$v$	Meridional wind field
$v'$	Fluctuating component of the meridional velocity
$\widetilde{v}$	Measured meridional wind field biased by the horizontal shear of vertical velocity
$v_0$	Uniform meridional wind field
$v_g$	Meridional geostrophic wind
$V(t, r_0)$	Received complex echo voltage
$V(t_0 + \Delta t)$	Received complex echo voltage at $t_0 + \Delta t$
$V(mT_s)$	Baseband time series signal
$v_a$	Aliasing velocity
$v_H$	Horizontal velocity
$V_H$	Horizontal wind magnitude

$V_T$	Wind speed transverse to the radar beam
$v_r$	Radial velocity
$\hat{v}_r$	Estimate of the mean radial velocity
$\mathbf{v}_r$	Radial velocity vector
$\mathbf{v}^{(p)}$	Instantaneous radial velocity at the $p^{th}$ LES grid cell
$w$	Vertical wind field
$w'$	Fluctuating component of the vertical velocity
$w_0$	Uniform vertical wind field
$W_r$	Range weighting function
$W_b$	Two-way beam weighting function
$W_{b_{tx}}$	One-way transmitter beam pattern weighting function
$W_{b_{rx}}$	One-way receiver beam pattern weighting function
$x_i$	Right cartesian coordinates - Einstein summation convention
$z$	Level of the grid cell
$z_0$	Vertical range of the radial velocity
$Z$	Reflectivity factor
$Z(f)$	Discrete time Fourier transform
$Z_e$	Equivalent reflectivity factor
$z_w$	Distance from the ground
$\beta_h$	Length of diffraction pattern
$\delta$	Separation scale
$\delta$	Bragg scale ( $\delta = \lambda/2$ )
$\delta_m$	Kroneker delta function
$\Delta$	Effective grid-cell size
$\Delta$	Oblique distance between layers in calculations of $\Delta n$
$\Delta n$	Refractive index gradient at the grid scale
$\Delta n'$	Refractive index gradient at the Bragg scale
$\Delta r$	Range resolution
$\Delta t$	Increment in time, usually a function of PRT
$\Delta x$	Grid cell size in the x-direction

$\Delta y$	Grid cell size in the y-direction
$\Delta z$	Grid cell size in the z-direction
$\Delta z_w$	Vertical dimension of the lower grid cell
$\epsilon$	Turbulence (eddy) dissipation rate
$\eta$	Radar reflectivity - average cross-section per unit volume
$\hat{\eta}$	Decorrelation parameter of $\hat{c}_{12}$
$\kappa$	Attenuation index
$\kappa$	Wavenumber
$\lambda$	Radar wavelength
$\Lambda$	Outer scale of the inertial subrange
$\Lambda_6$	Scale of the resolution volume
$\nu$	Kinematic viscosity
$\Omega$	Earth's angular velocity
$\phi$	Zenith angle
$\psi_e$	Echo phase of the received signal
$\psi_e^{(p)}$	Echo phase at the $p^{th}$ LES grid cell
$\psi_t$	Transmitted phase
$\psi_s$	Scattering phase shift
$\psi_0^{(p)}$	Random initial phase at the $p^{th}$ LES grid cell
$\rho_0$	Constant reference density
$\rho$	Cross-correlation factor at $t_0$ and $t_1$
$\sigma_{11}$	Doppler spectrum broadening due turbulence
$\sigma_b$	Backscattered radar cross-section
$\sigma_r$	Second central moment of the range weighting function
$\sigma_s$	Doppler spectrum broadening due shear
$\sigma_x$	Doppler spectrum broadening due signal processing
$\sigma_t$	rms wind variability for isotropic turbulence
$\sigma_v$	Doppler spectrum width
$\hat{\sigma}_v$	Estimate of the Doppler spectrum width
$\sigma_w^2$	Vertical velocity variance
$\tilde{\pi}$	Normalized pressure
$\theta$	Azimuth angle

$\bar{\theta}_{xtx}$	Transmitting antenna beam pointing in x-direction
$\bar{\theta}_{ytx}$	Transmitting antenna beam pointing in y-direction
$\bar{\theta}_{xrx}$	Receiving antenna beam pointing in x-direction
$\bar{\theta}_{yrx}$	Receiving antenna beam pointing in y-direction
$\Theta$	Potential temperature
$\Theta_{v0}$	Constant reference potential temperature
$\theta_1$	3-dB width of the one-way pattern (radians)
$\hat{\tau}_c$	Square root of the second moment of $\hat{c}_{12}$
$\hat{\tau}_p$	Peak time delay of $\hat{c}_{12}$
$\hat{\tau}_x$	Lag when $ \hat{c}_{11}(\tau_x)  =  \hat{c}_{12}(0) $
$\tau_w$	Transmitting pulse width

## Appendix B - List Of Acronyms and Abbreviations

ABL	Atmospheric Boundary Layer
ACF	Autocorrelation Function
ACRF	Atmospheric radiation measurement Climate Research Facility
ARM	Atmospheric Radiation Measurement
AWGN	Additive White Gaussian Noise
BMX	Beam MultiPlexing
BLR	Boundary Layer Radar
CBL	Convective Boundary Layer
CCF	Cross-Correlation Function
COHO	Coherent Oscillator
CW	Continuous Wave
DBS	Doppler Beam Swinging
DC	Direct Current
DOC	Department of Commerce
DOD	Department of Defense
DOT	Department of Transportation
DTFT	Discrete Time Fourier Transform
FAA	Federal Aviation Administration
FCA	Full Correlation Analysis
FCA-G	Full Correlation Analysis - Gaussian
FM-CW	Frequency Modulated - Continuous Wave
GMAP	Gaussian Model Adaptive Processing
HCA	Hydrometeor Classification Algorithm
IF	Intermediate Frequency
IPP	Inter-Pulse Period
JDOP	Joint Doppler Operational Project
JPOLE	Joint Polarization Experiment

LES	Large-Eddy Simulations
LMN	Lamont, OK
MLDA	Melting Layer Detection Algorithm
MPAR	Multifunction Phased Array Radar
MRC	Multiple Radar Configuration
MSE	Mean Square Error
MST	Mesosphere-Stratosphere-Troposphere
MU	Middle and Upper
NASA	National Aeronautics and Space Administration
NCAR	National Center for Atmospheric Research
NEXRAD	Next-Generation Radar
NOAA	National Oceanic and Atmospheric Administration
NSSL	National Severe Storms Laboratory
NPTS	Number of Points
NWRT	National Weather Radar Testbed
NWS	National Weather Service
OPERA	Operational Program for the Exchange of weather RAdar information
ORDA	Open Systems Radar Data Acquisition
OK	Oklahoma
PAR	Phased Array Radar
PPI	Plan Position Indicator
PRT	Pulse Repetition Time
PRF	Pulse Repetition Frequency
PSD	Power Spectral Density
QPE	Quantitative Precipitation Estimation
RADAR	Radio-Detection-And-Ranging
RASS	Radio Acoustic Sounding System
RF	Radio Frequency
RHI	Range Height Intensity
RMS	Root Mean Square Error
ROC	Radar Operations Center
RTI	Range Time Intensity
RUC	Rapid Update Cycle

RWP	Radar Wind Profiler
SA	Spaced Antenna
SBL	Stable Boundary Layer
SGP	Southern Great Plains
SNR	Signal-to-Noise Ratio
SODAR	SOunding Detection And Ranging
SOUSY	SOunding SYstem
SPRT	Staggered PRT
ST	Stratosphere-Troposphere
STALO	Stable Local Oscillator
TB	Time Balance
TEP	Turbulent Eddy Profiler
TKE	Turbulence Kinetic Energy
UHF	Ultra High Frequency
VCP	Volume Coverage Pattern
VHF	Very High Frequency
WSR-88D	Weather Surveillance Radar - 1988 Doppler
WSS	Wide Sense Stationary

## Appendix C

### Calculations of Structure Function Parameter of Refractive Index

Calculations of  $C_n^2$  due to isotropy at each LES grid cell can be alternatively estimated by computing the structure function as an average over the twelve edges of the cell (see Figure C.1). The square of the difference in the refractive index is estimated at each edge of the grid cell and divided by the the LES grid spacing  $\Delta$  as:

$$C_n^2 = \frac{1}{12} \sum_{k=1}^{12} (\Delta n_k)^2. \quad (\text{C.1})$$

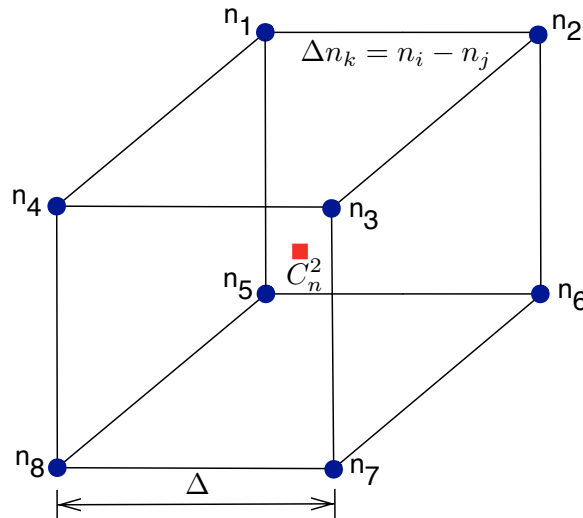


Figure C.1: Scheme that describes the calculations of  $C_n^2$  at each LES cell. The difference in refractive index  $\Delta n_k$  is calculated at edge of the cube considering the refractive index at each vertex. The length of each of the twelve edges of the cube corresponds by the LES grid spacing  $\Delta$ .

# Index

- Additive White Gaussian Noise, 56, 86, 110
- Autocorrelation function, 38–42, 46–48, 62, 80
- bias
  - ideal, 83, 85, 88, 93, 96
  - measured, 85, 88, 93, 96, 104, 112
- Boundary Layer
  - Atmospheric, 5, 16, 17, 35
  - Convective, 5, 6, 16–20, 22, 25, 26, 48, 113
  - depth, 5, 6, 16, 18, 22, 23
  - top, 53, 66, 73–75, 77, 86, 104, 108, 111, 113
  - Stable, 113, 114
- Bragg
  - scale, 15, 16, 35, 50, 51
  - scatter, 13
- Central Limit Theorem, 37
- COHO, 28, 29
- Cross-correlation function, 46–48, 62, 79, 80
- dissipation range, 35, 36
- Doppler Beam Swinging, 16, 18, 19, 43, 45, 48, 59, 61, 68, 77–81, 83, 85, 86, 88, 93, 96–100, 104, 108, 111, 112
- Doppler spectrum, 30, 31, 38–40, 112
  - width, 43, 77, 99, 102–105, 108, 113
- dwelt time, 40, 59, 61, 64, 65, 68, 74, 86, 100
- Einstein summation, 20
- energy-containing range, 35, 36
- entrainment zone, 5, 16–18, 26, 74, 77, 111
- ergodic, 37
- Eulerian framework approach, 50, 54
- free atmosphere, 5, 73, 104, 113
- Full Correlation Analysis, 46, 47
  - Gaussian, 47, 85, 88
- homogeneity, 43, 45, 59, 61, 103
- homogeneous, 49
- Horizontal shear of vertical velocity, 18, 19, 77, 78, 85, 88, 93, 98, 104, 108, 111, 112, 114
- in-phase, 28, 29, 37
- inertial subrange, 15, 35, 36, 49, 103
- inversion layer, *see* entrainment zone
- isotropy, 73, 103
- Lagrangian framework approach, 50
- Large-eddy simulations, 17–20, 22, 24, 48, 50–56, 58, 59, 61, 62, 64, 66, 68, 69, 73–75, 77, 78, 80, 86, 88, 93, 97–99, 103, 104, 108–112
  - sub-domain, 50, 56, 58, 61, 86
- mean square error, 83, 85
- mixed layer, 5, 69, 73, 75, 104, 112
- Power
  - Noise, 39–42
  - Signal, 39, 40, 42
  - Total, 39, 40, 42
- quadrature, 28, 29, 37
- radar, 6, 7
  - bi-static, 27, 55, 109
  - Boundary Layer, 16, 17, 24, 25, 48, 66, 68, 69, 86, 97–99, 104
  - clear-air, 7, 35, 39
  - Doppler, 7–9, 13, 19
  - heterodyne, 28, 29

- homodyne, 28, 29
- monostatic, 27, 33, 55, 58–61, 109
- PAR, 11, 12
- pseudo-monostatic, 62
- reflectivity, 9, 33–35, 49, 65
  - factor, 34
- simulator, 18, 19, 50, 55, 56, 62–64, 66, 67, 80, 81, 104, 109, 111, 114
- weather, 7, 32–34, 39
- Wind Profilers, 13, 19, 64–66, 68, 74, 77–79
- WSR-88D, 8–12
- radial velocity, 9, 30, 32, 37, 39–44, 48, 55, 59, 79, 102
- Radio Acoustic Sounding System, 64, 65
- range corrected shear, *see* bias
- RASS, *see* Radio Acoustic Sounding System
- Rayleigh
  - scatter, 7, 34
- refractive index, 13, 16, 34, 35, 49, 51
  - structure function parameter of, 19, 35, 36, 49, 50, 52–55, 64–66, 73, 75, 77, 78, 86, 109, 110
- refractivity, 49, 53
- revisit time, 68, 74, 75, 77, 99
- scan time, 59, 61, 64, 68, 86, 88, 98, 100
- sfrac, 81–83, 85, 86, 88, 89, 91–96, 99, 100, 111
- sodar, 114
- Spaced Antenna, 18, 19, 45, 46, 48, 80, 83, 85, 86, 88, 93, 96, 104, 109, 111
- STALO, 28, 29
- stationarity, 43, 45, 59, 61
- surface layer, 5
- Taylor frozen-turbulence hypothesis, 18
- turbulence, 4–6, 13, 17–20, 22, 25, 36, 39, 46, 49, 53, 66, 68, 80, 86, 108
  - energy spectrum, 35
  - isotropic, 35, 46, 49, 51
  - Spectrum width due, 43, 102, 103
- Turbulence kinetic energy, 18, 19, 97–99, 104, 112, 114
  - (eddy)dissipation rate, 18, 19, 77, 78, 99, 103, 104, 108, 113
- Vertical velocity
  - skewness, 19, 26, 64, 75, 77, 111
  - variance, 19, 64, 73, 74, 77, 111, 114
- vertical velocity fraction, *see* sfrac
- weighting function
  - beam, 55, 58, 59
  - range, 55
- Wide Sense Stationary, 37, 38